

NUMERICAL SIMULATIONS OF SLUG FLOW IN A MICRO CHANNEL

Andreas Carlson

Energy and Environmental Engineering

August 28, 2007

Master in Science Thesis

Division of Nuclear Power Safety

The Royal Institute of Technology

Department of Energy and Process Engineering

The Norwegian University of

Science and Technology

Professor: **Truc-Nam Dinh**

Professor: **Lars Sætran**

Abstract

Multiphase dynamics and characteristics of slug flow in micro channels are investigated computationally by means of advanced numerical simulation methods. Although, due to its importance in many engineering and biomedical applications, the topic has been studied previously, methods for robust and accurate simulation of slug flow remain elusive. Evaluation of current state-of-the-art Computational Multi Fluid Dynamics (CMFD) technology depicts deficiency with advanced computational methods (Volume of Fluid (VOF), Level Set, Adaptive Mesh Refinement (AMR)), which fail to deliver physically sound results. The separation of temporal and spatial length scales in the thin liquid film, formed between the channel surface and the gas bubbles, verifies the foreseen multiscale nature in the slug flow. This indicates that perturbations from the micro-scale can effectively propagate up scale, rendering the macro-scale description (CMFD) inadequate. A Sub-Grid Scale model was developed for the treatment of micro-scale thin liquid film dynamics based on the Long Wave Theory. A novel multiscale-coupling between a Sub-Grid Scale (SGS) thin film model and a CMFD code is proposed to preserve the micro-scale perturbations on the macro-scale and to enable high-fidelity simulations without a dramatic sacrifice of computational time. First-of-a-kind "multiscale-simulations" for the treatment of the microscopic lubricating thin film show unique physical results.

Abstract

Dynamikken i flerfase og dens typiske karakteristikk av slug strømning i mikrokanaler, er utforsket med avanserte simuleringsmetoder for numeriske beregninger. Til tross for dens viktige betydning for ingeniør og biomedicinsk anvendelse, samt emnet har vært studert tidligere, er robuste metoder og nøyaktig beregning for slug strømning unnvikende. Evalueringen av dagens teknologi, the state-of-the-art, Computational Multi Fluid Dynamics (CMFD), viser mangler i avanserte beregningsmetoder (Volume of Fluid (VOF), Level Set, Adaptive Mesh Refinement (AMR)), og svikter i å levere fysiske resultater. Separasjon av lengde og tids skalaer i den tynne væskefilmen, formet mellom kanalveggen og bobleoverflaten, bekrefter den forutsette multiskala-naturen i slug strømning. Dette indikerer at perturbasjoner fra micro-skalaen effektivt kan spre seg opp-skala, og gjør macro-skala (CMFD) beskrivelsen utilstrekkelig. En Sub-Grid Skala (SGS) modell var utviklet for beskrivelse av den tynne væskefilmens dynamikk, basert på Long Wave Theory (LWT). En ny multiskala-kobling mellom en Sub-Grid Skala (SGS), en tynn film-modell og en makroskopisk CMFD kode er foreslått for å bevare mikro-skala perturbasjoner på makro-skalaen, og for å kunne gjennomføre nøyaktige simuleringer uten en dramatisk økning i dens beregningstid. First-of-a-kind resultater fra multiskala simuleringer med behandling av en mikroskopisk lubrikerende film, viser unike fysiske resultater.

Contents

1	Introduction	1
2	Literature review	4
2.1	Experimental and numerical studies on slug flow in micro channels	6
2.1.1	Experimental studies	6
2.1.2	Numerical studies	10
2.2	Thin film dynamics and antagonistic governing forces	11
2.3	Recent theory and results on Multiscale coupling	15
2.4	Remarks on the literature review	17
3	Theoretical basis and numerical methods	19
3.1	Theoretical basis	20
3.1.1	Intermolecular and surface forces	20
3.1.1.1	Van der Waals forces and repulsive intermolecular forces	20
3.1.1.2	Surface forces	23
3.1.1.3	Surface and adhesion energies	25
3.1.2	Theory of multiphase flow	26
3.1.2.1	Governing equations single phase flow	27
3.1.2.2	Definitions and modeling of two-phase flow	29
3.1.2.3	Micro-channel effects	30
3.1.3	Long Wave Theory	31
3.1.4	Summary	33
3.2	Numerical methods	34
3.2.1	Finite Volume Method	34
3.2.1.1	Discretization schemes and time integration methods	35
3.2.1.2	Velocity-pressure coupling	37
3.2.2	Approaches on Computational Multi Fluid Dynamics	40
3.2.2.1	Volume of Fluid method	41
3.2.2.2	Level Set method	43

3.2.2.3	Continuum Surface Force model	45
3.2.2.4	Remarks on the CMFD methods	47
4	Evaluation of existing computational technology	48
4.1	Technical approach used for simulations of slug flow in a micro channel . .	48
4.1.1	Comparison of simulation results with FLUENT and TransAT . . .	49
4.2	Adaptive Mesh Refinement in FLUENT	52
4.2.1	AMR simulation with disturbed liquid inlet flow	54
4.2.2	Adaptation method in FLUENT	56
4.3	Critical comments on Diffuse Interface Tracking Methods	56
4.3.1	Comparison of FLUENT (VOF) and TransAT (Level Set)	57
4.3.2	Critical comment to the Continuum Surface Force model	61
4.4	Numerical experiments on slug flow in TransAT	62
4.4.1	Parameter domain	62
4.4.2	Numerical results and discussion	64
4.4.3	Remarks about the fidelity of TransAT	68
4.4.4	Multiscale phenomena in slug flow	71
5	Development and evaluation of a mechanistic micro-scale model for thin film dynamics	72
5.1	Development of a computational platform for the thin film equation	73
5.2	Evaluation of the computational platform for the non-dimensional thin film equation with intermolecular forces	73
5.3	Evaluation of computational platform for the dimensional thin film equation with intermolecular forces	75
5.4	Findings	79
6	Development of a novel technology and multiscale platform for coupling of a Sub-Grid Scale thin film model to a CMFD code	80
6.1	Hierarchy of descriptions for thin film Sub-Grid Scale model coupled to a macro solver	81
6.2	Methodology and algorithm for a Sub-Grid Scale model coupled to a CMFD platform	82
6.3	Multiscale simulations with a Sub-Grid Scale thin film model	87
6.3.1	Summary	90
7	Conclusion and future work	92

A	Rising bubble (spherical cap) benchmark case	102
A.1	Phase contour of rising bubble	104
A.2	AMR of rising bubble	107
A.3	Reduced time evolution of speed of bubble displacement	108
B	Parametric study of slug flow in TransAT	109
B.1	Parameter domain	109
B.2	Numerical results and discussion	111
C	Long wave theory	118
C.1	Critical note on publication: Long-scale evolution of thin liquid films [30] .	118
C.2	Effective length of Van der Waals forces	119

List of Figures

1.1	Picture from DEFOR experiment, showing high porosity and different internal cooling channels in the debris bed, printed with permission from T. N. Dinh.	2
2.1	Map of the topics reviewed in literature.	5
2.2	Sketched streamlines in bubble reference frame, upper figure $m > 0.5$, lower figure $m < 0.5$, from [45].	6
2.3	Section of bubble in horizontal tube, from [8].	7
2.4	Transition region, from [8]	7
2.5	Taylor's law eq.(2.3) (-) compared against eq.(2.1) (\cdot) and experimental data, from [3].	8
2.6	Transition zones for near circular channel with $D_h < 1mm$, from [2].	9
2.7	Schematic of multiscale method for Marangoni flow taken from [34].	17
2.8	Synthesis between the different fields of study.	18
3.1	Non retarded Van der Waals forces for different geometries with pair wise additive. Hamaker constant A calculated from eq.(3.5), taken from [22].	24
3.2	Static contact line from [22].	26
3.3	Multiphase flow pattern in a circular vertical pipe, experiments from Prasser et al. FZR.	27
3.4	Basic forces and macroscopic theory are merged into LWT.	33
3.5	Stencil for QUICK scheme on an equidistant mesh.	36
3.6	Sketch of CFL-number definition on a three point scheme, defining numerical and physical advection characteristics.	38
3.7	Equidistant cell centered and cell vertex meshes, (\bullet) indicates where the variables are defined.	38
3.8	Staggered equidistant mesh, (\rightarrow) indicates velocity in x-direction, velocity (\uparrow) y-direction and (\bullet) indicates where the pressure are defined.	39
3.9	Volume of fluid methodology, by coloring of the domain by the volume fraction.	42

3.10	Interface reconstruction method, Piecewise Linear Interface Calculation (PLIC).	42
3.11	Schematic drawing of the transition region for the CSF model taken from [7].	45
3.12	Positive and negative features with the VOF and Level Set method.	47
4.1	Initial condition of the simulations.	48
4.2	$\alpha = 0.25$ FLUENT calculations, Case 1.	50
4.3	$\alpha = 0.25$ TransAT calculations, Case 1.	50
4.4	$\alpha = 0.36$ FLUENT calculations, Case 2.	51
4.5	$\alpha = 0.36$ TransAT calculations, Case 2.	51
4.6	$\alpha = 0.49$ FLUENT calculations, Case 3.	52
4.7	$\alpha = 0.49$ TransAT calculations, Case 3.	52
4.8	FLUENT AMR results for $\alpha = 0.25$, Case 1.	53
4.9	FLUENT AMR results for $\alpha = 0.36$, Case 2.	53
4.10	Localized effects of spurious currents localized with $\leftarrow \downarrow$ in the refined interfacial area, pressure contours.	54
4.11	FLUENT AMR results for $\alpha = 0.25$, $\beta = 0.1$, Case 1.	55
4.12	FLUENT AMR results for $\alpha = 0.25$, $\beta = 0.2$, Case 1.	55
4.13	FLUENT AMR results $\alpha = 0.25$, $\beta = 0.5$, Case 1.	55
4.14	Close up on the adaptation in FLUENT on curved surface.	56
4.15	Effect on interfacial smearing of properties.	59
4.16	Contours of the densities with streamlines and isoline for $\phi = 0$, Case 1.	64
4.17	Contours of the pressure with velocity vectors and isoline for $\phi = 0$, Case 1.	64
4.18	Contours of the densities with streamlines and isoline for $\phi = 0$, Case 2.	65
4.19	Contours of the pressure with velocity vectors and isoline for $\phi = 0$, Case 2.	65
4.20	Contours of the densities with streamlines and isoline for $\phi = 0$, Case 3.	66
4.21	Contours of the pressure with velocity vectors and isoline for $\phi = 0$, Case 3.	66
4.22	Contours of the densities with streamlines and isoline for $\phi = 0$, Case 4.	67
4.23	Contours of the pressure with velocity vectors and isoline for $\phi = 0$, Case 4.	67
4.24	Pressure drop in long pipe ($\sim 24D$) for Case 1 – 4.	68
4.25	Contours of the densities with streamlines and isoline for $\phi = 0$, Case 5.	70
4.26	Contours of the densities with streamlines and isoline for $\phi = 0$, Case 5.	70
4.27	Multiscale problem in slug flow.	71
5.1	Multiscale coupling between two developed computational platforms.	72
5.2	Solution of the non-dimensional scaled film equation eq.(5.4) with Van der Waals potential $\Phi = AH^{-3}$.	75

5.3	Solution of the non-dimensional scaled film equation eq.(5.4) with Lennard-Jones potential $\Phi = A_3H^{-3} - A_9H^{-9}$	76
5.4	Solution of the dimensional film equation eq.(3.25) with Van der Waals potential $\phi = \frac{A'}{6\pi}h^{-3}$, with different Hamaker constants A' and $h_{mean} = 10nm$	77
5.5	Solution of the dimensional film equation eq.(??), $\phi = a_3h^{-3} - a_4h^{-4}$, $h_{mean} = 4.9nm$	78
6.1	Results from FLUENT and TransAT shows numerical dry-out.	80
6.2	Hierarchy of micro thin film descriptions coupled to a macroscopic solver.	81
6.3	Schematic drawing of near wall cell and adjacent wall normal cell containing the interface.	84
6.4	Domain for the microscopic thin film model for imposing boundary condition on the macro solver.	86
6.5	Multiscale simulation with $h_{min} = 0.1\mu m$ contours of the densities with streamlines and isoline for $\phi = 0$, Case 5.	88
6.6	Multiscale simulation with $h_{min} = 0.1\mu m$ contours of the densities with streamlines and isoline for $\phi = 0$, Case 5.	88
6.7	Multiscale simulation with $h_{min} = 0.05\mu m$ contours of the densities with streamlines and isoline for $\phi = 0$, Case 5.	89
6.8	Multiscale simulation with $h_{min} = 0.05\mu m$ contours of the densities with streamlines and isoline for $\phi = 0$, Case 5.	89
6.9	(a) Lodging state, (b) Lodging state, (c) Bubble lodged in on of the branches from [10].	91
A.1	Non dimensional time, $\tau = 0.01$	104
A.2	Non dimensional time, $\tau = 2.23$	105
A.3	Non dimensional time, $\tau = 3.69$	106
A.4	AMR results for rising bubble in stagnant liquid, $\tau = 5.53$	107
A.5	Space end time convergence, three different meshes with reduced time steps.	108
B.1	Contours of the densities with streamlines and isoline for $\phi = 0$, Case 6.	111
B.2	Contours of the pressure with velocity vectors and isoline for $\phi = 0$, Case 6.	111
B.3	Contours of the densities with streamlines and isoline for $\phi = 0$, Case 7.	112
B.4	Contours of the pressure with velocity vectors and isoline for $\phi = 0$, Case 7.	112
B.5	Contours of the densities with streamlines and isoline for $\phi = 0$, Case 8.	113
B.6	Contours of the pressure with velocity vectors and isoline for $\phi = 0$, Case 8.	113
B.7	Contours of the densities with streamlines and isoline for $\phi = 0$, Case 9.	114
B.8	Contours of the pressure with velocity vectors and isoline for $\phi = 0$, Case 9.	114
B.9	Contours of the densities with streamlines and isoline for $\phi = 0$, Case 10.	115

B.10	Contours of the pressure with velocity vectors and isoline for $\phi = 0$, Case 10.	115
B.11	Contours of the densities with streamlines and isoline for $\phi = 0$, Case 11.	116
B.12	Contours of the densities with streamlines and isoline for $\phi = 0$, Case 11.	116
B.13	Pressure drop in short pipe ($10D$) for Case 6, 7, 10.	117
C.1	Effective length of the Van der Waals forces shown by changing initial mean film height, parameters from [9].	119

List of Tables

4.1	Applied numerical schemes and methods.	49
4.2	Applied numerical schemes and treatment of color function (C-F), number of cells and max CFL number.	49
4.3	Material properties, Case 1 – 3.	49
4.4	Numerical schemes and treatment of color function (C-F), number of cells and max CFL number for AMR simulations.	53
4.5	Numerical schemes and methods for AMR simulations.	53
4.6	Material properties, Case 1 – 4.	63
4.7	Bubble velocity, slip ratio and Capillary number, Case 1 – 4.	63
4.8	Weber number, Case 1 – 4.	63
4.9	Ohnesoge number, Case 1 – 4.	63
4.10	Material properties, Case 5.	68
4.11	Bubble velocity, slip ratio and Capillary number, Case 5.	69
4.12	Weber number, Case 5.	69
4.13	Ohnesoge number, Case 5.	69
5.1	Analytical and computed minimum film height with LJ-potential, $\Phi = A_3H^{-3} - A_9H^{-9}$	76
5.2	Properties for media used for film study.	77
A.1	Material properties rising bubble.	103
B.1	Material properties, Case 6 – 11.	109
B.2	Bubble velocity, slip ratio and Capillary number, Case 6 – 11.	110
B.3	Weber number, Case 6 – 11.	110
B.4	Ohnesoge number, Case 6 – 11.	110

Nomenclature

Roman Symbols

$()_G$	gas notation
$()_L$	liquid notation
A	Hamaker constant
c	volume fraction
h	local film height
P	pressure
S_{ij}	rate of deformation tensor
u_i	instantaneous velocity in direction i
\underline{u}	velocity vector
U_{GS}	superficial gas velocity
T	time
$w(r)$	intermolecular potential
$W(r)$	intermolecular body potential
$\underline{\underline{I}}$	unit tensor

Greek Symbols

α	void fraction
γ	surface energy
ρ	density
μ	dynamic viscosity
ν	kinematic viscosity
σ	surface tension coefficient
ϕ	dimensional intermolecular forces
Φ	non-dimensional intermolecular forces
τ	viscous shear stress

Non-dimensional numbers

Bo	Bond number
Ca	Capillary number
Oh	Ohnesoge number
Re	Reynolds number
We	Weber number

Abbreviations

AMR	Adaptive Mesh Refinement
CFD	Computational Fluid dynamics
CFL	Courant-Friedrich-Leavy
CMFD	Computational Multi Fluid Dynamics
CPU	Central Processing Units
CSF	Continuum Surface Force
DNS	Direct Numerical Simulation
FEM	Finite Element Method
FVM	Finite Volume Method
HLPA	Hybrid Linear / Parabolic Approximation
LST	Linear Stability Theory
LWT	Long Wave Theory
MDS	Molecular Dynamics Simulation
MUSCL	Monotone Upstream-Centered Scheme for Conservation Laws
NS	Navier-Stokes
PISO	Pressure-Implicit Split Operator
PLIC	Piecewise Planar Interface Reconstruction
PRESTO	PRESsure Staggered Option
QUICK	Quadratic Upwind Interpolation for Convective Kinetics
SGS	Sub-Grid Scale
SIMPLE	Semi Implicit Method for Pressure-Linked Equations
SIMPLEC	Semi Implicit Method for Pressure-Linked Equations Consistent
VOF	Volume of Fluid
WENO	Weighted Essential Non-Oscillatory

Chapter 1

Introduction

Multiphase flow dynamics and characteristics of slug flow in a micro channel are investigated by means of advanced numerical simulation methods. Micro channels inherit features that make them feasible for numerical simulations compared with larger channels. Flow patterns are more stable, as an effect of the capillary force, with modest separation of length scales and the computational domain is substantially reduced with the same mesh resolution.

Micro channels play an important part in many natural processes and industrial applications. They are especially suitable for heat transfer processes due to their large area to volume ratio. The flow patterns in these channels often consist of two or three phases, a multiphase flow. In many processes it can be crucial to determine the nature of the flow pattern.

Elongated bubbles or slug flow is subject of study in this thesis. Slug flow is often encountered or used in engineering applications: micro-components, biomedical and oil and gas industry. It inherits a nature that makes it appropriate for heat and mass transport. The bounding liquid film, formed between the pipe surface of the pipe and the bubble interface, is the determining parameter for heat transfer. The importance of qualitative knowledge about the flow phenomenon can be illustrated by the case of a cooling debris bed. In a hypothetical severe reactor accident, hot liquid melt is released into a pool of cooling liquid. This forms a debris bed in the lower reactor plenum. To ensure that we determine the risk of, and develop mitigative measures to deal with a severe reactor accident (core melt-down), it is crucial to determine its coolability. The debris bed is a porous media, consisting of cooling channels of arbitrary shape. Many of these channels are micro channels with a multiphase slug flow pattern.



Figure 1.1: Picture from DEFOR experiment, showing high porosity and different internal cooling channels in the debris bed, printed with permission from T. N. Dinh.

The determining parameter for heat removal in slug flow is the thin film formed between the pipe surface and the bubble interface. The thin film can rupture for cases of high heat flux, generating a *burnout*. It implies that the gaseous phase is in direct contact with the solid surface, making the debris bed un-coolable. Burnout is an important aspect also for other engineering applications. It is a critical safety aspect for cooling application as well as the limiting factor in performance enhancement.

Different topics have been studied in the open literature in accordance with the focus of this work: experimental and numerical study on slug flow in micro channels, thin film dynamics and intermolecular forces, multiscale coupling. There exist a vast amount of literature, and key papers are sought within each topic with the aim to notice previous hinders as well as model and method limitations.

Volume of Fluid (VOF) and Level Set are two of the most widely applied interface tracking methods and current state-of-the-art for multiphase flow simulations. For the investigation of the slug flow phenomenon two Computational Multi Fluid Dynamics (CMFD) codes have been applied, FLUENT (VOF) and TransAT (Level Set). Our first goal is to evaluate the capabilities and performance of the two methods and codes to adequately describe the slug flow phenomenon. By comparing their performance we want to depict numerical artifacts and suggest mitigative strategies.

We know that a thin film will be formed between the pipe wall and bubble interface, for a certain parameter domain. This occurs when the surface tension forces are domi-

nating, low Capillary (Ca) number;

$$Ca = \frac{\mu U}{\sigma}. \quad (1.1)$$

We suspect that the thin film slug flow phenomenon inherits a multiscale nature.

Our second goal is to verify this hypothesis from simulation results, and develop a novel technology for the multiscale coupling between a Sub-Grid Scale (SGS) thin film model and a CMFD code.

With this basis the thesis is structured into five major parts:

1. Literature review.
2. Theoretical basis and numerical methods.
3. Evaluation of existing computational technology.
4. Evaluation of a mechanistic micro-scale model for thin film dynamics.
5. Development of a platform for a novel multiscale coupling of a Sub- Grid Scale thin film model to a CMFD code.

Chapter 2

Literature review

In such a complex phenomenon as slug flow many different topics can be studied in depth. In this literature review emphasis is directed on:

1. Experimental and numerical study on slug flow in micro channels.
2. Thin film dynamics and intermolecular forces.
3. Multiscale coupling.

The different topics are selected in accordance with the focus of this work, the coupling between slug flow and thin film dynamics. As mentioned earlier there is a discrepancy between studies of slug flow and thin film: even though they are closely related to each other, they are usually studied separately. Experimentalist holds on to the already developed correlations for film height or they intend to modify them. It is not possible to quantify features in the film (down to nm) from experiments, as a consequence of material refraction index and optical limitations. Numerical simulations for very thin films in slug flow are non-existing and this author was unable to identify any report in the open literature about slug flow simulation with treatment of microscopic thin film. For very thin film high mesh resolution comes with the cost at a high computational time, and the thin film is often not resolved. Different avenues for the investigation of thin films have been sought. Usually these films are initially stagnant and planar on a semi-infinite plate. Effects of the intermolecular forces on the film are modeled in different attempts. Also a separation of the different effects is used to define what are the forces that govern the film topology. Coupling these two separate phenomena is also a question of coupling two different scales in both time and space. This is where the multiscale coupling enters. Recent progress and methods are reviewed and the most promising ones for the slug flow simulation are described. The review of multiscale coupling is not developed in depth: the multiscale methodology is in this thesis a promising tool for the elaborated coupling

of separated scales, but the focus here is not on developing or extending this methodology.

There is a vast amount of literature on slug flow, numerical simulations of slug flow in micro channels and thin film dynamics. Figure 2.1 depicts a topical structure, by which published papers and reports were sought and analyzed.

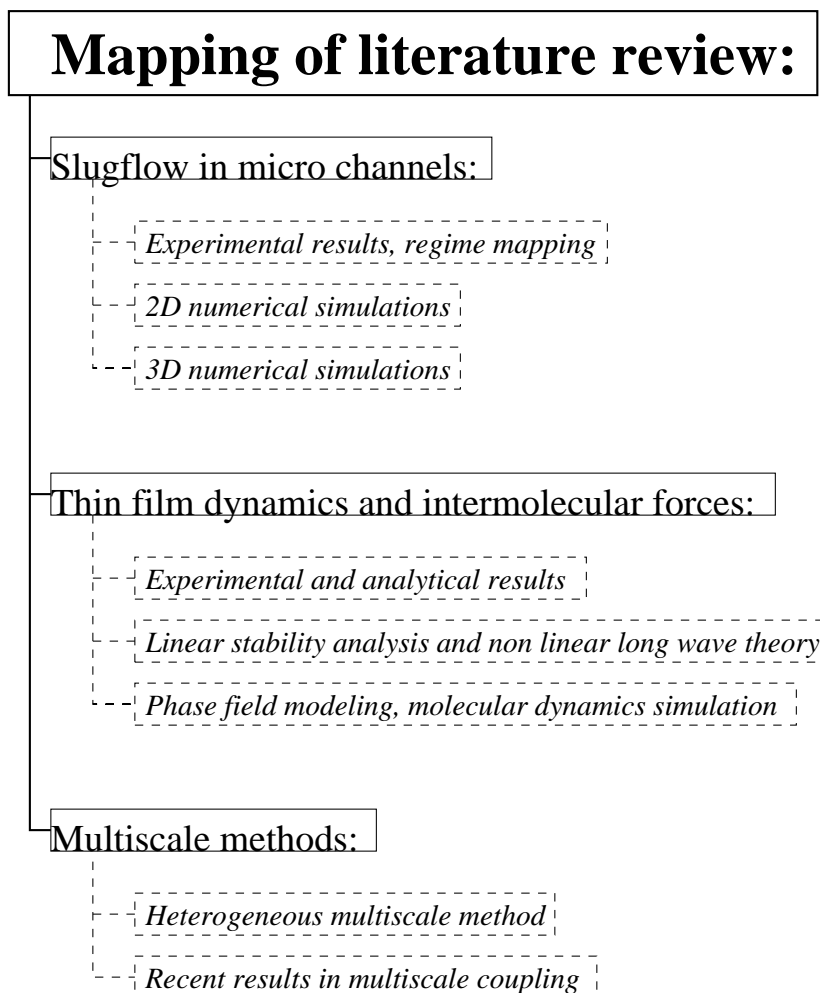


Figure 2.1: Map of the topics reviewed in literature.

2.1 Experimental and numerical studies on slug flow in micro channels

2.1.1 Experimental studies

In 1960 two papers were published [45], [8] which still stand today as a fundament for research on long bubbles in tubes, slug flow. Both these papers followed a publication by Fairbrother and Stubbs [17]. They proposed a relationship between the non-dimensional ratio of the difference in bubble velocity and the mean velocity ahead of the bubble, $m = \frac{U-U_m}{U_m}$, with the capillary number eq.(1.1), $m = Ca^{\frac{1}{2}}$. Taylor [45] performed experiments on different fluids and criticized the validity of the correlation for m . His experiments were valid for a valid for a broad range of capillary number, $10^{-4} < Ca < 1.9$, and the results did not match Fairbrother and Stubbs correlation. Taylor also sketched different streamline patterns for slug flow for different values of m .

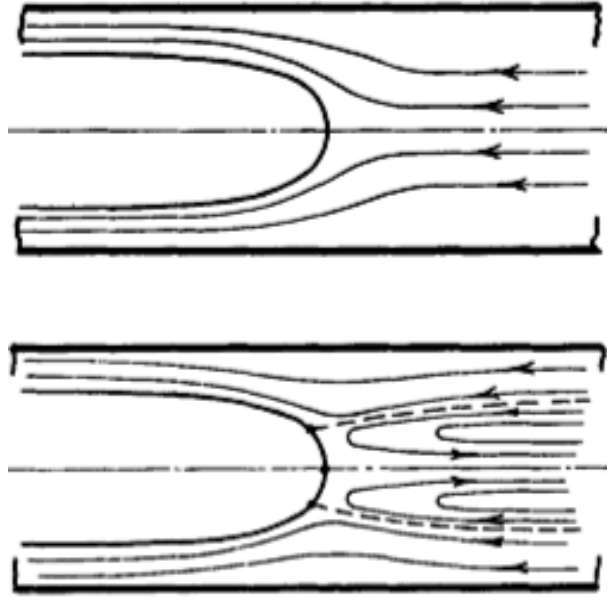


Figure 2.2: Sketched streamlines in bubble reference frame, upper figure $m > 0.5$, lower figure $m < 0.5$, from [45].

Bretherton [8] studied two cases of elongated bubbles in tubes, first case where bubbles travel in a small horizontal tube and second bubbles in a vertical tube. He approached the problem analytically and proposed a correlation for the height of the deposited liquid film on the wall. Some simplifications were made in his analysis, $Bo \ll 1$, $Re \ll 1$, $We \ll 1$. He also divided the bubble area into different regions, visualized in Figure 2.3 and assumed that the film section is planar in the transition region. With these assumptions he used lubrication theory, a simplification of Navier-Stokes equations, to

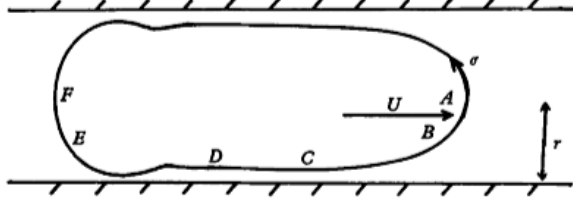


Figure 2.3: Section of bubble in horizontal tube, from [8].

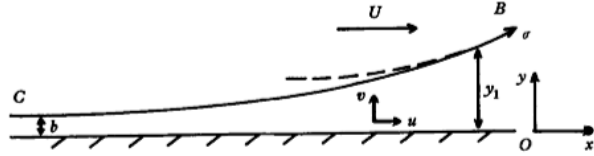


Figure 2.4: Transition region, from [8]

obtain the following thin film correlation:

$$\frac{\delta}{r} = 1.337 \left(\frac{\mu U}{\sigma} \right)^{\frac{2}{3}} = 1.337 Ca^{\frac{2}{3}} \quad (2.1)$$

where δ is the film height. He validated his correlation by experiments, but he already in 1960 pointed out a discrepancy for very thin films and pointed on disjoining pressure as a possible new governing force in the film. The validity of Bretherton's correlation was studied experimentally in [3] and numerically in [25]. Remarkably, validity of Bretherton's correlation was found to be limited to the range of Ca number between $10^{-4} < Ca < 10^{-2}$. It is assumed that with increasing Ca the assumption of negligible inertia forces no longer hold. A quite recent publication on the topic of deposition of liquid film on a wall was published by Quèrè and Aussillous [3]. They used the results from Taylor's experiments and by scaling law extended the correlation from Bretherton to be valid for a larger limit of Ca numbers ($10^{-4} < Ca < 10^0$). The film forms in the dynamic meniscus of a thickness δ and length λ . The flow takes place due to the difference in curvature in the meniscus and static film, defined by the Laplace pressure difference, $\Delta p = \sigma/r$. This yields then for the balance of the viscous forces and the pressure gradient, $\frac{\mu U}{\delta^2} \sim \frac{1}{\lambda} \frac{\sigma}{r}$. By using the fact that the Laplace pressure is constant at the interface, or that the spherical part matches the curvature at the transition region,

$$-\frac{\sigma}{r} - \frac{\sigma \delta}{\lambda^2} \sim -\frac{2}{\lambda} \frac{\sigma}{r}. \quad (2.2)$$

The unknown in these equations is the length of the transition region, and with the classical scaling law $\lambda = \sqrt{\sigma r}$ we obtain \sim eq.(2.1). As Ca increases Quèrè, claims that r must be replaced with $r - \delta$ for the deposition scaling law. Both eq.(2.1) and scaling law fit well with Taylor's results, a fit of the data with the new scaling of the film thickness

in the visco-capillary regime gives Taylor's law:

$$\frac{\delta}{r} = \frac{1.337Ca^{\frac{2}{3}}}{\left(1 + 2.5 \cdot 1.337Ca^{\frac{2}{3}}\right)} \quad (2.3)$$

which is valid for higher Ca than eq.(2.1).

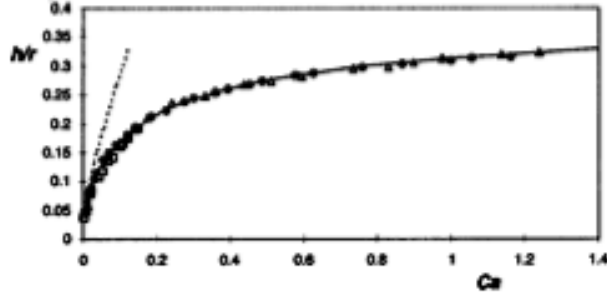


Figure 2.5: Taylor's law eq.(2.3) (-) compared against eq.(2.1) (· ·) and experimental data, from [3].

Quèrè divides the slug flow into three different regimes: visco-capillary deposition, visco-inertia and viscous boundary, to point out discrepancies with the Taylor law. The visco-capillary regime is already discussed above. In the visco-inertia regime (relative high velocity) it was found that the effect of inertia thickens the film, and Taylor's law under predicts the film height. A threshold of $U = 1\text{m/s}$ was found for the validity of eq.(2.3). In the viscous boundary layer regime the deposited film can be limited by a viscous boundary layer, which develops in the liquid drop (between the slugs) as it moves. The thickness can be then derived from the balance between inertia and viscosity, which yields the classical Prandtl law:

$$\delta \sim \left(\frac{\mu L}{\rho U}\right)^{\frac{1}{2}} \quad (2.4)$$

where L is liquid drop length.

Bico and Quèrè [5] experimentally looked at different liquid trains in tubes to examine the effects of different hydrophobic and hydrophilic liquids. Different effects and promising results were shown: deposition of multiple film layers for coating and determining mass transport of slugs.

The flow regimes observed in micro channels differ in some extent from the ones observed in larger channels. Ghiaasian et al. [2] used previously published experimental results to categorize the flow regimes in micro channels. Previously the micro channel regimes have been divided into three different ones, surface tension dominated, inertia dominated and transition. An additional flow regime was proposed, inertia dominated

(zone 1 and zone 2). The four different zones are mapped by the non-dimensional *Weber* number with the superficial gas and liquid velocity.

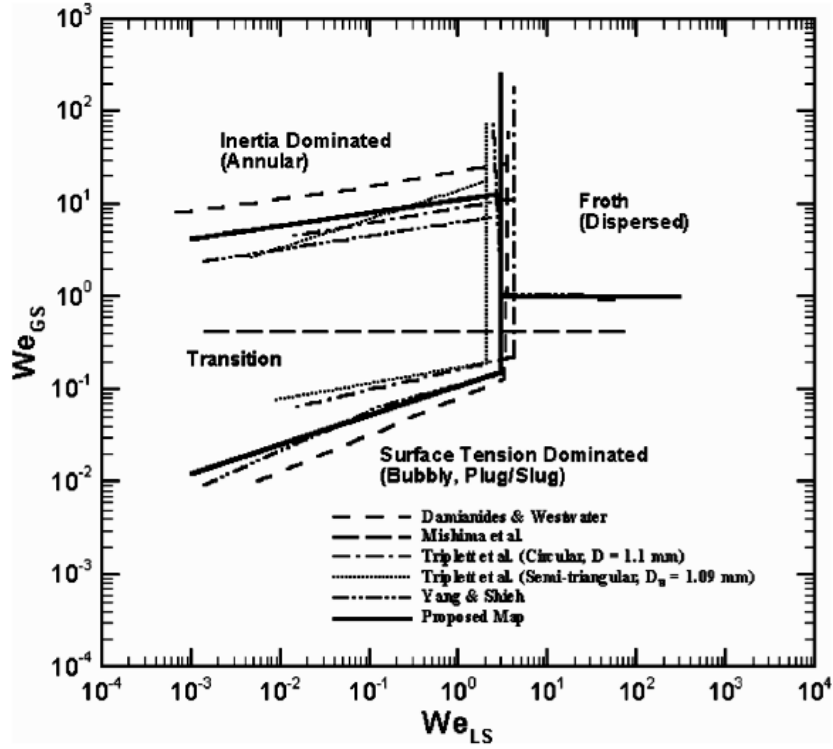


Figure 2.6: Transition zones for near circular channel with $D_h < 1\text{mm}$, from [2].

Pan et al. [12] experimentally investigated the flow regimes in micro channels, and mapped the regimes with use of superficial gas and liquid velocity. Also a peculiar flow pattern called bubble-train slug flow was reported. This flow pattern is characterized by the presence of several bubble-trains formed by several bubbles connected together by a liquid membrane between neighboring bubbles.

This review shows signs of the multiscale nature of deposition of thin liquid film in slug flow. Bretherton's [8] correlation for film thickness in slug flow has recently been extended by Quèrè [3] for a larger parameter domain. Although this correlation is current state-of-the-art, it is not valid for the parameter domain where very thin films are formed (Ca number $< 10^{-4}$). This comes as a consequence, since it is not feasible to correlate very thin films solely by hydrodynamics, as new intermolecular forces are effective.

2.1.2 Numerical studies

The strength of numerical simulations is the possibility to investigate small details that are impossible to observe in experiments. Some of the previous mentioned results have been used to validate results from CFD simulations. [19], [16] performed $2D$ simulations on the Bretherton problem, a gas inflow displacing a viscous fluid, both with in-house developed codes. Heil [19] investigated the effect of inertia on the flow field in front of the propagating bubble, pressure distribution and height of the liquid film. A strong effect on the recirculation pattern was reported with increase of Re as well as a thickening of film height. It was also reported that a generation of closed vortexes at the tip of the finger significantly increases pressure rise in the region. Shyy et al. [16] used state of the art computational techniques with an immersed boundary method on an adaptively refined Cartesian grid. Marker based method was applied to capture the interface representation with a continuous interface method. Trailing film thickness for different Re and Ca number were reported and validated against other publicized results, as well as results of the pressure distribution and variation of film thickness in time. Ghiaasiaan and Akbar [1] investigated Taylor flow or Taylor bubbles with the use of the commercial CFD code FLUENT with a Volume of Fluid (VOF) method, $2D$ simulations. The initial bubble geometry was defined at the start of the simulations. Two different simulations were performed with either initial bubble radii calculated from experimental results ("type 1") or initial film thickness from eq.(2.3) ("type 2"). The obtained results were compared against experimental result for bubble length and bubble velocity, comparison against the drift flux model, and previously proposed correlations for bubble length and pressure drop. A new correlation for the frictional pressure drop was proposed. Also a quite fair match against results for film thickness was obtained for "type 2" calculations. Lakehal et. al. [26] investigated slug flow for a diabatic case with means of the Level Set method. Several different flow patterns were observed and validated against experimental results from [12]. Physical insight was sought on the micro-channel slug flow, and a new correlation was proposed for the bubble velocity based on break-up frequency. Heat transfer distribution was investigated and compared with single phase flow. The overall heat-removal in two phase flow is higher than single phase flow. Slug flow shows to dissipate more heat in the bulk, and bubbly flow has a higher wall heat flux due blockage effects.

Some simulations have also been performed for $3D$ geometries, to investigate $3D$ effects. $2D$ calculations for slug flow are not a trivial task, and extending to $3D$ case means increasing complexity and CPU time. Taha and Cui [44],[43] simulated $3D$ slug flow with the commercial code FLUENT with a VOF method to study geometrical effect of a square vertical capillary and a round vertical tube. In both cases, recirculation patterns were reported, though it should be noted that viscosity effects are neglected. Bonometti et al.

[35] both experimentally and numerically looked at liquid droplets moving in a circular micro channel. The recirculation velocity pattern was obtained in both experiments and simulations. Dye was used to show mixing within each droplet.

For a more comprehensive review on the fluid mechanical aspects in slug flow, experimental and numerical results, I would recommend readers to a paper by Kreutzer et al. [25].

VOF is the classical interface tracking method for multiphase flow simulations. It is the most widely applied method, and is implemented in the commercial CMFD codes. Recent advancement of the Level Set method shows promising results. The performance of both VOF and Level Set methods are closely investigated and compared in Chapter 4.

2.2 Thin film dynamics and antagonistic governing forces

For thin films, less than 100nm, new forces appear which are not described by macroscopic continuum theory in this case the Navier-Stokes equations. Different avenues of describing film dynamics with some of the obtained results are also discussed here. The main body in this part of the review is concerned with the lubrication theory, also called Long Wave Theory (LWT). This is a simplification of the Navier-Stokes equations, also discussed more in detail in 3.1.3, for thin film dynamics. Also other approaches are mentioned along with experimental results.

Jain and Ruckstein [23] deduced a theoretical framework with the use of Navier-Stokes equation to study thin film dynamics. By extending the Navier-Stokes equations with an additional body force term for the Van der Waals forces, they investigated isothermal thin film on a semi-infinite horizontal plate bounded between a solid and a gas. The equations were reduced by a simplification in terms of lubrication theory. Applying a small perturbation on the interface, film ruptures occur when the perturbations grow in time and linear stability analysis was used to determine rupture and rupture time. Also different cases were investigated to show effects of pure film, surface active agents and viscous film. It was shown that an initial periodic disturbance along the bounding plane has a critical wavelength much larger than the mean height of the film. Film rupture occur for perturbations with wavelengths larger than the critical wavelength.

Sharma and Ruckstein [39] followed the path of Jain and Ruckstein [23] to study the instability and rupture time for films with an finite disturbance. Linear stability analysis

predicts the effect of infinitesimal disturbances growing or decaying in the film. A finite disturbance is accounted for in the base state of the film, the zeroth order solution (and brings it closer to the initial perturbation). It was shown that for large initial perturbation with surfactant concentration, nonlinear effect for both the Marangoni-flow (surface elasticity) and surface viscosity prolong the film rupture several times more than what linear theory predicts. Also the rupture of a tear film in the external eye was studied, and showed large qualitative discrepancy between non-linear and linear theory for large amplitude perturbation.

Burelbach et al. [9] extended the non-linear theory developed by William and Davis [47] for a case including evaporation, thermo-capillary, non-equilibrium effects, in addition to disjoining pressure induced by Van der Waals forces. The numerical solution of the film equation from long wave theory was shown for the isothermal case with Van der Waals forces with extended discussion of the behavior near the rupture point. Also film cases for quasi equilibrium and non-equilibrium with evaporation and condensation, taking into account mass loss/gain, thermo capillarity and vapor recoil, were investigated. Vapor recoil is a destabilizing force for evaporation or condensation of films, and can cause hydrodynamic instability. Since a fluid particle conserves its mass flux upon phase change, a liquid particle at the interface accelerates greatly when it vaporizes. The vapor particle has a much lower density than the liquid density. This back reaction at the interface is called vapor recoil. Van der Waals forces, evaporation and condensation were all destabilizing phenomena and caused film rupture.

Long-range apolar and polar forces in thin films have been described by Sharma with co-workers, who have contributed to a number of milestones in thin film research by the use of long wave theory, [36], [37], [38]. Additional polar forces as electrostatic forces have been modeled and different effects due to these new forces have been shown. The different topologies of the films have also been investigated and mapped as effects of change in the free energy. They argue that the linear stability theory for long wave theory is inadequate in terms of rupture time. The rupture time from non-linear theory shows rupture time that differ of several orders of magnitude comparing with linear stability theory, this shows that the nonlinear effects are important near film rupture. In [38] the formation of different $2D$ morphological patterns are shown with initial topography of "hills" and "valleys" for air-water interface with Van der Waals and polar forces. The evolution of the film show different types of patterns formed depending on the initial mean film height. For relative thick films ($> 8\text{nm}$) holes are formed and films ($< 8\text{nm}$) tend into isolated stable droplets (pseudo wetting). These results are claimed not predictable by either linear or nonlinear $1D$ analysis. It is though stated that with $1D$ analysis it is possible to

predict their length scales.

Stable structures have been observed in $1D$ film studies by Mitlin and Petviashvili [27] who investigated a typical Lennard-Jones ($3 - 9$) potential for the intermolecular forces in the frame work of long-wave theory. Kinetically stable structures were observed as attractive and repulsive forces level each other. The structures and topography resemble a pseudo-wetting scenario. Also Deissler and Oron [13] observed stable film structures but by the $2D$ film equation, describing the $3D$ spatiotemporal evolution of air-liquid interface of a thin film on a cooled horizontal plate, has a Lianpunov function that is strictly non increasing in time. This is used to show existence of stable axi-symmetric structures. Oron [29] further studied the $3D$ film evolution, but for the case of evaporating film with the one sided model derived by Burelbach et at. [9] without accounting for vapor recoil and gravity. The intermolecular forces were modeled by a Lennard-Jones potential, with a repulsive and attractive term. Stable structures of a non-evaporating film was found in agreement with $1D$ results from Mitlin and Petviashvili [27]. Temporal evolution of the film patterns shows peak formations going into broad circular troughs, which broaden into expansion of "holes" that coalesce into a pattern of "droplet" on a thin film. These patterns are assumed to decrease due to wetting of the solid due to capillary forces not because of evaporation. The patterns decrease until a flat stable film is formed, which rapidly dries out almost uniformly in space.

Majumdar and Mezic discussed the influence of the Hamaker constant for both Van der Waals, hydration, electrostatic forces and elastic strain interaction. Stability maps for Van der Waals, DVLO (Van der Waals and electrostatic potential) based on Hamaker constant and critical wave length were proposed. It is shown that surface tension tends to stabilize the film, since film instabilities increase the surface area and as an effect also surface energy. Suman and Kumar [42] also investigated the effect of Hamaker constant (by a time periodic wettable surface). Mean Hamaker constant was reported to determine rupture or stable patterning regardless of amplitude and frequency. Oscillations could delay rupture of films with spatial wettability gradients are present, but not prevent rupture.

In [40] a macroscopic mechanism of film rupture is described without inclusion of intermolecular force terms in Navier-Stokes. A similar asymptotic reduction of the equations as in long wave theory was performed. The rupture was described by tangential stress from the inclusion of surface tension gradient (Marangoni flow).

For a more comprehensive review on Long Wave Theory we refer to the work of Oron et

al. [30].

From the literature on film dynamics and slug flow, one point emerges. Numerical simulations on slug flow have been triggered by experimental results, the opposite is the case for thin films. More and good experimental results are needed to validate and compare against numerical results and theory. Some of the obtained experimental results for thin films and intermolecular forces are here discussed.

Sharma et al.[33] experimentally investigated a thin Polydimethylsiloxane (PDMS) film on a silicon wafer coated with a PDMS brushes, bimodal (dimethylsiloxane) (PDMS) brush. The main advantage of using these polymers in both coating and film media is that they allow to modify short range interaction at the film interface without having to introduce a chemical potential between the substrate and film. Initially the PDMS film (41nm,60nm and 80nm) is stable with air as a bounding medium. Antagonistic polar intermolecular interaction by the long range forces was studied by placing a millimeter water film on the PDMS film. As a consequence the effective Hamaker constant changes from the initial configuration. This introduces a dramatic change in the morphology of the PDMS film. The initial stable film undergoes a generic transition from "hills" and "valleys", coalesce and develop stable drop patterns. By removing the water the PDMS re-spread. Again introducing bounding water film the PDMS goes into pseudo-wetting, so the procedure is re-healing. $2D$ simulations in [38] show similar film morphology. The results were obtained by optical micrographs and show the crucial effect produced by the change of the Hamaker constant. A similar experiment was performed in [32], with a PDMS film with a thin layer of a polystyrene (PS) film. This structure is initially stable, as water is introduced on top of the PS film the PDMS-PS bilayer start to destabilize the system. By removal of the water the PDMS-PS bilayer re-spreads. It is shown that long range forces between PDMS and water influence over the PS bilayer. However the magnitude of the forces are unexpectedly high.

Blossey et al. [4] performed experiment of a PS film on an Si wafer with a SiO coating layer. Experimental results for PS film morphology were compared against numerical simulations of $2D$ thin film equation from lubrication theory. Similarities of the experimental and simulated results were strikingly good in both time and space. Both dewetting morphology and satellite holes were reported.

Sharma et al. [33] argue that it might not be correct to assume that long range forces can be neglected for film distances above 100nm. Israelachvili et al. [11] reported experimental findings of coalescing interfaces of both liquid-liquid and liquid-gas. These results show long range intermolecular Van der Waals forces active for distances over $100nm$.

The distance between the media was determined by an adjacent fingers of chromatic order (FECO) in a spectrogram. Coalescence of the interfaces showed compelling results as well as the effect of Van der Waals forces for interfacial spacing of 200nm.

It should however be noted that other simulation methods for thin film dynamics have also been applied that the one mentioned above. Two of these avenues are molecular dynamics and Cahn-Hilliard Navier-Stokes phase field modeling. They have received increasing attention as the computational power grows. Hwang et al. [21] did simulate film rupture for a Lennard-Jones fluid with molecular dynamics simulation. [48] simulated a stressed film by phase field modeling and reported interesting stable structures within the thin film.

The literature review on thin films shows that several avenues have been tracked to describe the thin film dynamics. The Long Wave theory (LWT), developed in the late seventies is the most studied and applied, enable simulations and analysis of thin film dynamics. Development of accurate numerical algorithms for the film equations shows that the theory has matured, and in [4] numerical results from the LWT match well with experimental results. This is recognized and the LWT is exploited in present work; first Section 3.1.3 gives a thorough description of the theory, second Chapter 5 shows results from a developed computational platform for the film equation.

2.3 Recent theory and results on Multiscale coupling

There have been several attempts to deal with multiscale phenomena, where spatial and temporal time scales are separated. A methodology for such multiscale coupling has been proposed in the framework called Heterogeneous Multiscale Methods (HMM) by Engquist and co-workers. Two key papers will in this section be discussed in HMM . For readers with interest in details I would refer to the two papers, [15], [34].

Engquist et. al. [15] give a review of the frame work of HMM, current progress of the different scientific fronts of multiscale coupling and a coherent summary of the status of HMM. The name "heterogeneous" is used to emphasize the different nature in the phenomena. For many phenomena a macro scale solver may not produce accurate results or the error in the effective models exceed the solution error. Such systems may need special treatment, or new effective models for the microscopic scales. Treating the whole domain with a microscopic model would be inefficient in terms of computational time. The HMM rest on a macroscopic solver for the "whole" domain. The microscopic model is used in a complementary way to provide information missing on the macro-scale. Typically, one is

not interested on the details of the micro-scale solution. Definition taken from [15].

1. "We have to ask for less about the solutions of the micro-scale solver, e.g. we have to be satisfied with getting only the gross behavior of the solution, not the details everywhere.
2. We must explore possible special features of the micro-scale problem, such as scale separation, self similarity. Therefore these methods are less general than traditional micro-scale solvers.

One of the main challenges is to recognize such special features in a problem and make use of it." The use of multiscale solver is only justified if:

$$\frac{\text{cost of multiscale method}}{\text{cost of the micro-scale solver on the full domain}} \ll 1. \quad (2.5)$$

Multiscale problems are separated into four different types:

Type A: These are problems that contain isolated defects or singularities such as cracks, dislocations, shocks and contact lines. For these problems, the microscopic model is only necessary near defects or singularities. Further away it is adequate to use some macroscopic model. Such a combined macro-micro strategy should satisfy the minimum requirement if the micro scale model is limited to a small part of the computational domain.

Type B: These are problems for which a closed macroscopic model should exist for a properly selected set of macroscopic variables, but the macro scale model is not explicit enough to be used directly as an efficient computational tool. The task of multiscale modeling is to carry out macro scale simulations without making use of ad hoc constitutive relations. Instead, the necessary macro scale constitutive information is extracted from the micro scale models. The existence of a closed macroscopic model is often associated with time scale separation, and this can be exploited in order to design multiscale methods that satisfy the minimum requirement.

Type C: These are problems that have features of both type A and type B.

Type D: These are problems that exhibit self-similarity in scales. Examples include critical phenomena in statistical physics, fractals and turbulent transport."

Some "simple" multiscale examples for case A and B are discussed.

E W. and Ren W. [34] presented results from successful multiscale simulations for different

cases. Special emphasis was put on complex fluids and micro-fluidics, and results from type A and B problems. For case B problems atomistic-based constitutive modeling simulation results are shown by extracting the stresses from molecular dynamics simulations and results from pressure driven Poiseuille flow and dumb-bell flow with a Lennard-Jones fluid. Also type A problems are discussed with modeling of boundary conditions. Problems with complex fluid-solid interaction (lid driven flow), surface tension, contact line dynamics are shown with results. Molecular dynamics simulations are typically used to extract boundary conditions in a constrained region. Below a figure shows extraction of boundary condition for Marangoni flow at AB, from a domain decomposition. The picture at the right in Figure 2.7 shows the setup of the molecular dynamics simulations, from the extracted domain to the left. The strip CD is constrained by continuum velocity field, and the boundary conditions are extracted at the sampling region.

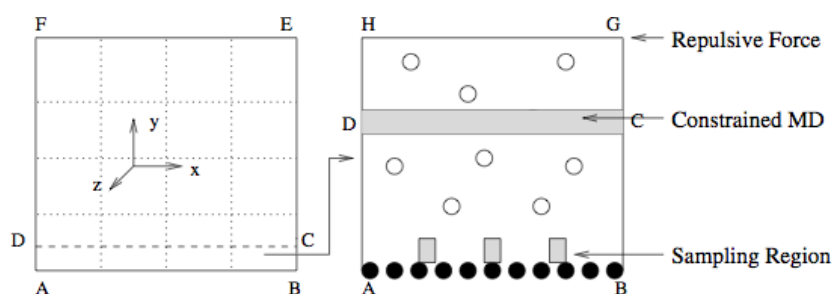


Figure 2.7: Schematic of multiscale method for Marangoni flow taken from [34].

2.4 Remarks on the literature review

The literature study performed in this Chapter provides a systematic overview of previous relevant works and establishes the state of the art. From the author's perspective, it was important to notice previous hinders as well as model and method limitations. From the reader's perspective, four important points are extracted from the review:

- Even with abundant experimental work, no one has been able to quantify thin film physics in slug flow for low Ca-numbers. As the film height becomes very small ($h < 100\text{nm}$) correlations from hydrodynamics fail, such phenomena have a dual nature from molecular dynamics and hydrodynamics.
- VOF is the classical method for interface tracking, but new development of the Level Set method increase its "marked value" and use. Both methods inherit strong geometrical (case) constrains and are computational expensive. The author could not report any findings in literature of previous attempts on a Sub-Grid Scale (SGS) thin film model in slug flow.

- Thin film dynamics have been approached in a numerous different ways. Advancement in Long Wave Theory shows it has matured, and capabilities to capture both natures (molecular dynamics and hydro dynamics). Since the LWT is recognized as a prospective avenue it has been further pursued in Chapter 5, where a SGS computational platform for the thin film equation have been developed, for the investigation of thin film dynamics.
- Recent development and results the Heterogeneous Multiscale Method makes it the most promising framework for a multiscale treatment. Multiscale coupling with a SGS thin film model is discussed in Chapter 6.

Although, thin film dynamics, experiments and numerical simulations on slug flow are separate fields of study, for the phenomenon of deposition thin film slug flow they are closely interacting in a synthesis. Perturbations from the micro-scale thin film can effectively propagate up-scale and influence the macro-scale slug flow, it is a *multiscale phenomenon*.

We notice that the theoretical models and numerical methods are ripe: this is capitalized on in a multiscale coupling. By applying a multiscale coupling we want to increase accuracy in the calculations, by accounting for the micro-scale perturbations, without a dramatic sacrifice of computational time.

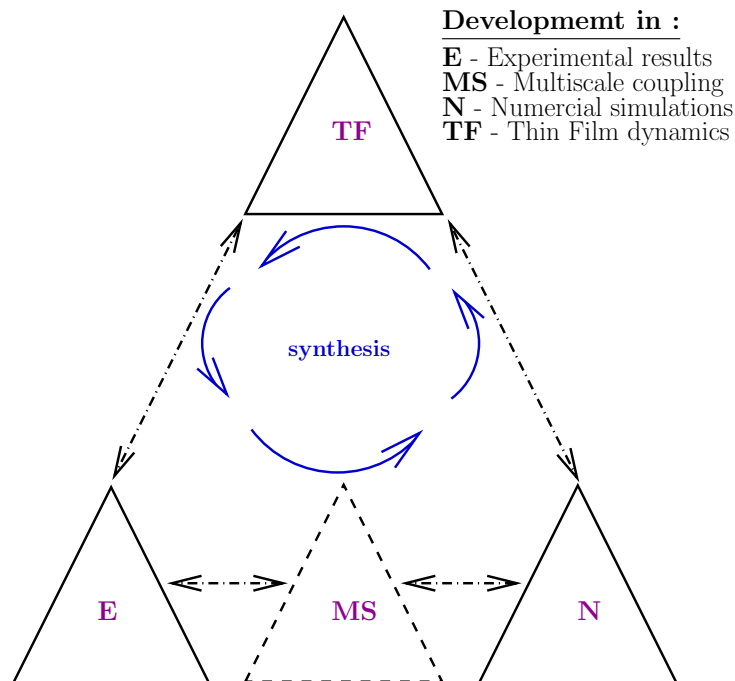


Figure 2.8: Synthesis between the different fields of study.

Chapter 3

Theoretical basis and numerical methods

The objective of this thesis is to establish a qualitative knowledge of the slug flow when the height of the liquid film formed between the wall and bubble interface is very small. The laws of hydrodynamics govern the gross picture with slug flow in a pipe. In the parts of the domain where the film is in the order of nano meters new forces appear between the interface of the fluid film and the wall. These new forces are not covered by hydrodynamics, and often referred to as a *disjoining pressure*. Molecular dynamics describe these forces by the intermolecular interaction between the molecules in gas, liquid and solid.

The fact that the theory behind hydro dynamics and molecular dynamics is well separated they are described separately. The theoretical section is divided into three parts, where the last subsection is devoted to the Long Wave theory for thin films. It merges both hydro dynamics and molecular dynamics theory to capture the dual nature of thin film dynamics.

3.1 Theoretical basis

The structure of the theoretical basis is given:

1. Intermolecular and surface forces
 - *Van der Waals and repulsive intermolecular forces*
 - *Surface forces*
 - *Surface and adhesion energies*
2. Macroscopic theory of two phase flow
 - *Multiphase flow phenomena*
 - *Governing Navier-Stokes equations*
 - *Micro-channel effects*
3. Thin film dynamics
 - *Long Wave Theory*

3.1.1 Intermolecular and surface forces

Many phenomena can be adequately explained without to the need to explicitly take into account intermolecular forces, even though they are always present. All-important forces should be implicitly accounted for through property and macro-representation. This does not always hold, and the intellectual challenge lies in determining where one needs to include a microscopic model in the phenomena. The effect of micro-scale forces on a macro scale phenomena is clearly shown in [14]. A nanoscopically treated surface of a spherical object released into a liquid pond, prove that the microscopic liquid-surface interaction makes a crucial impact on the macroscopic behavior if it leaves a splash or "plop". The phenomena inherits a multiscale nature.

The most important intermolecular and surface forces for thin film are discussed here. The theories are taken from the book of Israelachvili [22] which I would like to refer to for a more thorough and extended discussion.

3.1.1.1 Van der Waals forces and repulsive intermolecular forces

Different forces can appear between molecules, as electrostatic interaction involving charged or dipolar molecules. These forces are influenced by orientation and charge within each

molecule. Dispersion force is like gravity in continuum mechanics, always present between molecules even neutral ones, and plays perhaps the most important role in the Van der Waals forces. Here some of the most important effects from the dispersion force are summarized taken from [22]:

1. "They are long-range forces and, depending on the situation, can be effective from large distances (greater than $10nm$) down to interatomic spacing (about $0.2nm$)
2. These forces may be repulsive or attractive, and in general the dispersion forces between two molecules or large particles does not follow a simple power law.
3. Dispersion forces not only bring molecules together but also tend to mutually align or orient them, though this orienting effect is usually weak.
4. The dispersion interaction of two bodies is affected by the presence of other bodies nearby. This is known as *non-additive* of an interaction."

The dispersion force is originating from quantum mechanics. Consider a neutral atom, with a zero time average dipole momentum. At an instantaneous time there exists a dipole moment due to the shift of positions of the electrons around the nuclear proton. This instantaneous fluctuating dipole momentum is generating an electric field, which polarizes the nearby (neutral) atom, generating a dipole momentum in it. As a consequence the two dipole interaction induce an instantaneous attractive force between the two atoms, *dispersion force*. From quantum mechanical perturbation theory London (1937) derived an expression for the dispersion forces or London dispersion forces,

$$w(r) = \frac{-C_{disp}}{r^6} \quad (3.1)$$

r is the distance to the nearby atom. In more general terms the net Van der Waals forces consist of three parts for interaction of polar molecules, induction forces C_{ind} , orientation forces C_{orient} and dispersion forces C_{disp} :

$$\begin{aligned} w_{VDW}(r) &= -\frac{C_{VDW}}{r^6} = -\frac{[C_{ind} + C_{orient} + C_{disp}]}{r^6} \\ &= -\frac{[(u_1^2\alpha_{02} + u_2^2\alpha_{01}) + \frac{u_1^2u_2^2}{3kT} + \frac{3\alpha_{01}\alpha_{02}h\nu_1\nu_2}{2(\nu_1+\nu_2)}]}{(4\pi\epsilon_0)^2r^6}. \end{aligned} \quad (3.2)$$

Where the α_0 is the polarizabilities of molecule 1 and 2, ϵ_0 is the dielectric permittivity u is the instantaneous dipole moment, h is Planck constant and ν is electron orbiting frequency. London theory has two shortcomings with the assumption of just one ionization potential per atom/molecule and it cannot describe molecular interaction in a

solvent. McLachlan (1963) gathered the orientation, induction and dispersion forces in one equation also valid for molecular interaction in solvents.

$$w(r) = -\frac{6kT}{(4\pi\epsilon_0)^2 r^6} \sum_{n=0,1,2,\dots}^{\infty} \prime \frac{\alpha_1(i\nu_n)\alpha_2(i\nu_n)}{\epsilon_3^2(i\nu_n)} \quad (3.3)$$

$i\nu_n$ is the imaginary frequency, \prime in the summation is for the zero frequency $n = 0$ that needs to be multiplied by 0.5. This equation covers the whole spectrum of frequencies to obtain the total polarizability effect, and it is also valid for molecular interaction in a solvents medium. The dispersion forces are in general exceeding the dipole dependent induction and orientation effects except for small highly polar molecules such as water. It should also be noted that both McLachlans and London's theory is only valid for separation of molecules larger then atomic separation $r \gtrsim 0.2\text{nm}$.

Retardation effects originate from the same mechanism as attractive dispersion forces. Considering two neutral atoms with, zero time averaged dipole moment, separated by a substantial distance. One of them has a fluctuating dipole moment and the time for the electric field to reach the second atom and return becomes comparable to the time of the fluctuating dipole moment. As this electric field returns the orientation of the dipole moment is changed and less favorable to an attractive interaction. This is called *retardation* effect or in terms of dispersion forces, *retarded* force.

Repulsive forces play a dominating role at very small interatomic distances as electron clouds overlap and strong repulsive forces arise. Usually these forces have been labeled: exchange repulsion, hard-core repulsion, steric repulsion, Born repulsion (for ions). Unlike dispersion forces the short range repulsion forces do not have a general description. Instead several empirical functions have been proposed to describe their dependence with distance. They seem all to be satisfactory as long as they have a steep rising repulsion at small separations. By summing both attractive and repulsive forces on can obtain a intermolecular pair potential. The most known and widely used of these pair potentials is the Lennard-Jones potential or "6-12" potential given;

$$w(r) = \frac{A}{r^{12}} - \frac{B}{r^6} = 4\epsilon \left[\frac{\sigma}{r^{12}} - \frac{\sigma}{r^6} \right]. \quad (3.4)$$

The σ is a cut-off length, one should note that it is different from the molecular diameter. The first term is a repulsive (power law) potential and second term originates from the Van der Waals dispersion forces from London's theory. $w(r) = 0$ at $r = \sigma$ is the distance where the attractive and repulsive forces are even. Minimum energy is $w(r) = -\epsilon$ with contribution from the attractive Van der Waals, -2ϵ . Eq.(3.4) is simple and widely used,

even though it can not be proved as rigorously as the Van der Waals potential. It is expected that the repulsion potential would in reality be higher than the order of 12 and the London theory underestimate the Van der Waals term since it only accounts for a single absorption frequency. Results from experiments on typical Lennard-Jones fluids (apolar fluids) match the potential well.

3.1.1.2 Surface forces

The discussion so far has been limited to molecule-molecule interaction; here the analogy is extended for forces between surfaces and interfaces. For two adjacent bodies one may sum the energies of all atoms in one body with all the atoms in the second body to obtain a "two-body" potential for an atom at the surface. The Van der Waals interatomic pair potential strongly decays between neighboring atoms, to the inverse power of six. Clearly the Van der Waals potential between macroscopic bodies decays much slower than the interatomic pair potential Figure 3.1 so it can be effective over larger separations and their interaction energy is proportional to their size.

ρ_1 and ρ_2 are the number of atoms per volume (atom density) in the bodies, C is the coefficient in the atom-atom pair potential and A is the *Hamaker* constant here in conventional form from Hamaker(1937).

$$A = \pi^2 C \rho_1 \rho_2. \quad (3.5)$$

The Hamaker constant does in a large extent determine the behavior of the Van der Waals forces between macroscopic bodies. Usually the Hamaker constant is in the order of $\sim \pm(10^{-19} - 10^{-20})$, by knowing its value and the distance between the bodies their potential can be calculated. It is a puzzle that we still can not explain the Hamaker constant in detail, strictly speaking it is never truly a constant, but changes with the separation distance D . Still a great deal of insight is needed to explain its behavior and then intermolecular forces.

Lifshitz (1956) proposed a theory for interacting macro bodies, which completely avoids the problem with additive. The atomic structure is neglected and the (continuous) interaction force between the two bodies is determined from continuous bulk properties as refraction index and dielectric constant. The theory springs out from quantum field theory, and was adopted late in the scientific community due to its complexity.

Israelachvili showed Van der Waals interaction energy between a molecule or small particle

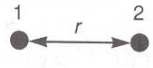
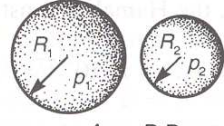
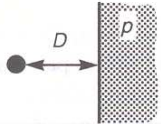
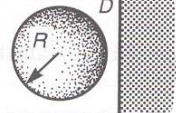
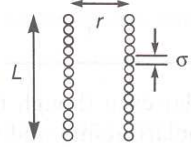
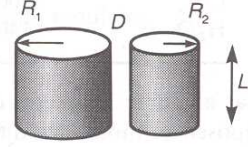
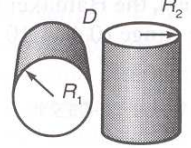
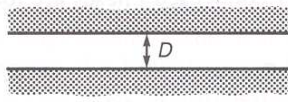
<p>Two atoms</p>  <p>$w = -C/r^6$</p>	<p>Two spheres</p>  <p>$W = \frac{-A}{6D} \frac{R_1 R_2}{(R_1 + R_2)}$</p>
<p>Atom-surface</p>  <p>$w = -\pi C p / 6D^3$</p>	<p>Sphere-surface</p>  <p>$W = -AR/6D$</p>
<p>Two parallel chain molecules</p>  <p>$W = -3\pi CL / 8\sigma^2 r^5$</p>	<p>Two cylinders</p>  <p>$W = \frac{AL}{12\sqrt{2} D^{3/2}} \left(\frac{R_1 R_2}{R_1 + R_2} \right)^{1/2}$</p>
<p>Two crossed cylinders</p>  <p>$W = -A\sqrt{R_1 R_2} / 6D$</p>	<p>Two surfaces</p>  <p>$W = -A / 12\pi D^2$ per unit area</p>

Figure 3.1: Non retarded Van der Waals forces for different geometries with pair wise additive. Hamaker constant A calculated from eq.(3.5), taken from [22].

1 in a medium 3 with the surface medium 2 can readily be written as:

$$\begin{aligned}
 W(D) &= -\frac{\pi C \rho_2}{6D^3} \\
 &= -\frac{3kT a_1^3}{2D^3} \sum' \left[\frac{\epsilon_1(i\nu_n) - \epsilon_3(i\nu_n)}{\epsilon_1(i\nu_n) + 2\epsilon_3(i\nu_n)} \right] \left[\frac{\epsilon_2(i\nu_n) - \epsilon_3(i\nu_n)}{\epsilon_2(i\nu_n) + \epsilon_3(i\nu_n)} \right] \\
 &\approx -\frac{A a_1^3}{3D^3}.
 \end{aligned} \tag{3.6}$$

The intermolecular potentials that have so far been discussed are always present in a system. For ionic solutes or highly polar molecules also electrostatic or double layer repulsion forces can play an important role. Electrostatic "double layer" forces can emerge in two different ways: either from ionization (or dissociation) of surface groups or by adsorption (binding) of ions on the previously uncharged surface. These electrostatic forces can be both attractive and repulsive depending on the charges of the surfaces and

can be dominating. Derjaguin and Landau, Verwey and Overbeek proposed a theory for including both van der Waals and double layer repulsion forces. This is called the *DLVO theory*.

3.1.1.3 Surface and adhesion energies

Several different phenomena arise from the surface energies γ between phases, where γ is usually referred to as *surface tension*. Surface energies originate from intermolecular forces between two media, for two identical media $W = -A/12\pi d^2$. Consider the case with two media and then by performing a pair wise summation of all molecules one would obtain two additional terms:

$$W = -constant + \frac{A}{12\pi D_0^2}. \quad (3.7)$$

Where the first term arises from the cohesive bulk energy with the atoms of their immediate neighbors. The second term, which is always positive, originates from unsaturated "bonds" at the two surfaces. Consider the case with air suspended in water. Water molecules feel attraction from their neighbor water molecules. At the interface there are a reduced number of molecules for the water molecules to "bind" with, since the amount of liquid molecules (water) exceed the number of gas molecules (air). This process is energetically unfavorable. Energy is needed to transport molecules from the bulk to the interface. Creation of a new surface is energetically costly and the fluid system will try to minimize the surface area as seen in the second term. Which is the reason for the spherical shape of a gas suspended in a liquid. Same analogy is true for immiscible liquids.

The energy needed to separate to different media, from contact to infinity is referred to as the work of *adhesion*, if they are similar it is the work of *cohesion*. Surface energies are an effect of the adhesion.

The description above is a *phenomenological* description of surface tension. The same description is extended mathematically by the Gibbs-Helmholz law for free energy from thermodynamics, which is defined by the enthalpy S , temperature T and internal energy U in the system. Gibbs law is given,

$$G = TS + U. \quad (3.8)$$

Surface tension is defined,

$$\gamma = \left(\frac{\partial G}{\partial A} \right)_{T,P} \quad (3.9)$$

where the temperature T and pressure p is constant. All thermo dynamical systems tend to the equilibrium state by minimizing the free Gibbs energy in the system. As a consequence the surface will try to minimize its area by creating a spherical shape.

Three phase contact line dynamics is a problem for the interaction of multiple phases. For instance consider a droplet lying on a surface with a surrounding vapor. This treatment of the contact angle have been described by Young's or Young-Duprè's equation.

$$\text{Young's equation: } \gamma_{12} + \gamma_2 \cos \theta_0 = \gamma_1. \quad (3.10)$$

$$\text{Young-Duprè's equation: } \gamma_2 (1 + \cos \theta_0) = W_{12}. \quad (3.11)$$

The angle between the contact point and droplet interface is the contact angle, which is also used as a macroscopic variable to determine if the liquids wet the solid. As is seen from the Figure 3.2 the contact line dynamic is a microscopic problem where at the contact point are governed by molecular interaction. As the drop does not move this is referred to as a *static contact angle*. If the droplet should move in time this referred to as *dynamic contact angle*.

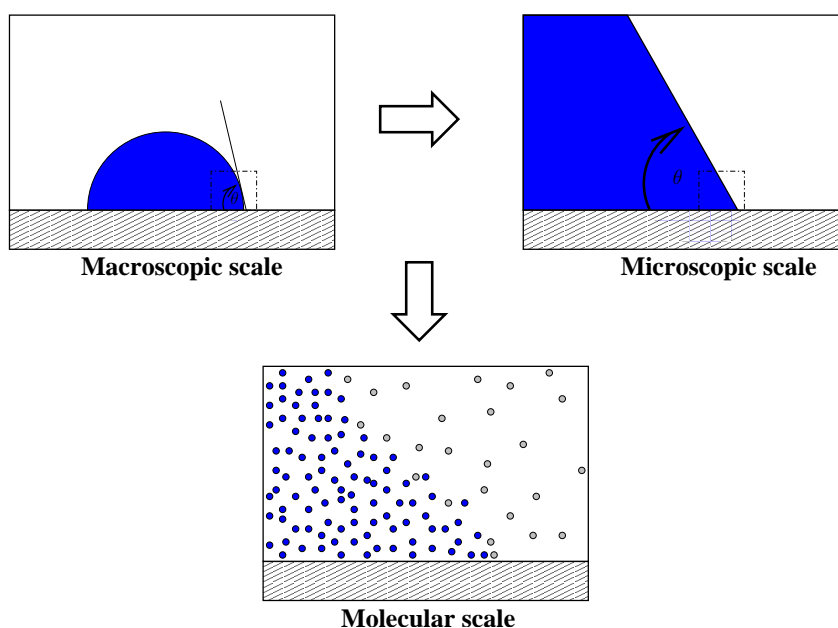


Figure 3.2: Static contact line from [22].

3.1.2 Theory of multiphase flow

Historically the research on single phase flow has been extensive compared to multiphase flow. This has given us a great insight and knowledge in even complex single phase flow phenomena like (for some cases of) turbulent flow. Qualitative knowledge of the multiphase flow pattern can often be of crucial importance as determining turbulent behavior in single phase flow. The multiphase flow patterns often appear where there is

both heat and mass transfer. In the picture one can see the flow pattern in a circular vertical pipe; from finely dispersed flow, slug flow and annular flow.

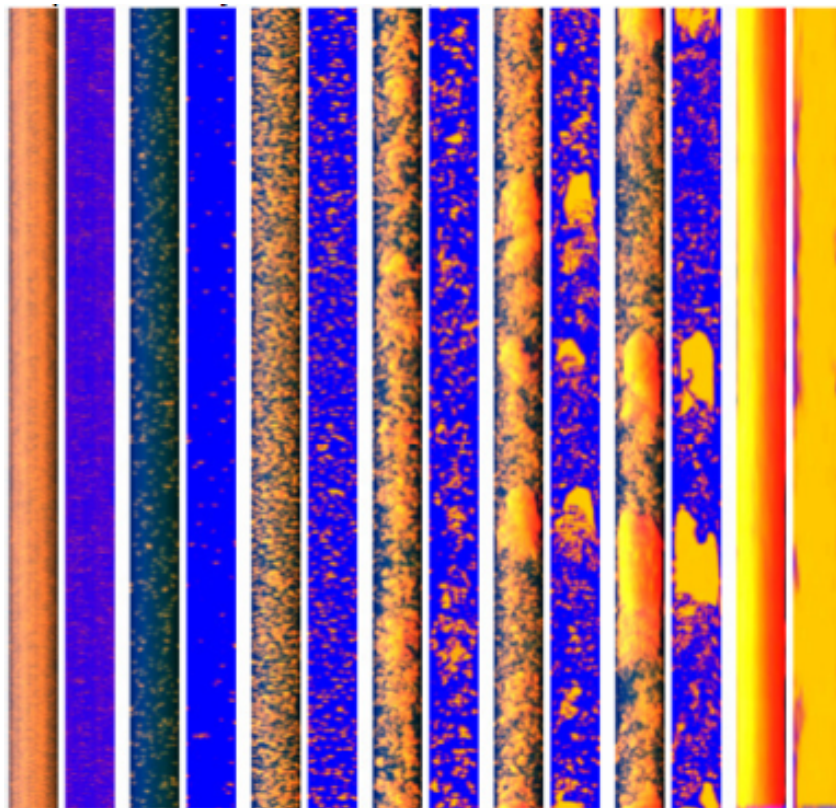


Figure 3.3: Multiphase flow pattern in a circular vertical pipe, experiments from Prasser et al. FZR.

3.1.2.1 Governing equations single phase flow

The Navier-Stokes equations are today well accepted as the solution for macroscopic flow phenomena in fluid mechanics. Here the discussion is limited to the case where the flow is assumed to be *incompressible*, *adiabatic* and *laminar*. Incompressibility means that the density is constant and not effected by pressure. This then neglects compressibility effects. The cases are adiabatic which implies that there is no heat transfer. Laminar flow is a term for flow with stable, structured flow pattern (streamlines) and with no typical separation of time and length scales. The Reynolds number is used as a measure to determine if the flow is laminar or turbulent:

$$Re = \frac{\rho u L}{\mu}. \quad (3.12)$$

A usual threshold for laminar single phase flow in a pipe is that $Re < 2300$. The complexity of laminar flow is incomparable with the case of turbulent flow. Phenomenological

the turbulent flow phenomenon is depending on geometry, it is inertia driven, the structure of the flow is partly stochastic and with a large transfer of momentum. It has an unsteady nature (never steady state) with small and large eddies that can be separated in both time and space. The smallest whirls (eddies) are down to the Kolmogorov dissipating scales, and the largest eddies are up to several order of magnitude larger. In the governing equations the disturbance in the flow must be accounted for. New highly non-linear terms originate from the disturbances, where especially the Reynolds stresses play an important role. The Reynolds stresses (6 new terms) along with the other new terms generate a *closure problem*, the presence of more unknowns than equations creates the need for turbulence modeling. In this thesis the Reynolds numbers are so small that the flow is assumed laminar. Here are the governing equations for laminar incompressible flow continuity and momentum conservation:

$$\nabla \cdot \mathbf{u} = 0 \quad (3.13)$$

$$\rho \left(\frac{\partial \mathbf{u}}{\partial t} + \mathbf{u} \cdot \nabla \mathbf{u} \right) = -\nabla p + \nabla \cdot 2\mu \mathbf{S} + \mathbf{F}. \quad (3.14)$$

The \mathbf{S} or S_{ij} is the rate of deformation tensor also used the viscous stress tensor $2\mu S_{ij}$:

$$S_{ij} = \frac{1}{2} \left(\frac{\partial u_i}{\partial x_j} + \frac{\partial u_j}{\partial x_i} \right). \quad (3.15)$$

The \mathbf{F} is typically a body force term that comes from additional body forces as the gravitational force or the surface tension force.

The *Laplace pressure* is often used to describe the pressure at the interface connected to the constant surface tension coefficient and curvature. This is a macroscopic or measurable surface tension force. The pressure difference is the jump between the bubble and surrounding pressure. Young-Laplace formula defined,

$$p_s = p_2 - p_1 = \Delta p = \sigma \kappa \quad (3.16)$$

κ is the interfacial curvature. As for the case of slug flow in a channel or a rising (buoyancy driven $\rho_b < \rho_l$) bubble suppressed a liquid medium, there is a different curvature between the tail and front of the bubble. As a consequence there is a different pressure at the tail and front generated by the Laplace pressure.

Considering the change in free energy by expanding a curved surface following the analogy of Gibbs law, one obtains the same Young-Laplace equation.

3.1.2.2 Definitions and modeling of two-phase flow

Some of the basic concepts and terms in two phase flow will be discussed here. As well as a short introduction to the approach on the conservation laws for two phase flow.

Usually the amount of liquid or gas that are in the domain plays an important role. The void fraction is the variable that defines this quantity and $0 \leq \alpha \leq 1$. To obtain the void fraction α different averaging operations can be performed as (also valid for other variables): cross section averaging eq.(3.17), volumetric averaging, time averaging.

Cross section area averaging operator in space for a generic quantity, for the given phase k :

$$\langle f_k \rangle_k = \frac{1}{A_k} \int_{A_k} f_k dA. \quad (3.17)$$

This gives then the cross section averaged void fraction for the given phases:

$$\langle \alpha_G \rangle = \alpha_G = \frac{A_G}{A_L + A_G}. \quad (3.18)$$

There can be a number of different velocities that can be defined. The different phases will in general not have the same velocity, so that there can be a relative velocity between them.

True velocity or velocity u_G and u_L is the instantaneous velocity of the phases, which is the actual speed they are traveling.

Superficial velocity or volumetric flux j_G and j_L are based on the true velocity multiplied with the void fraction of the phase. Their physical interpretation is the velocity of each phase as if they were flowing each alone,

$$j_G = \alpha_G \cdot u_G. \quad (3.19)$$

The total local superficial velocity is:

$$j = j_L + j_G. \quad (3.20)$$

The averaged quantities are as well used, $\langle j_G \rangle$, $\langle j_L \rangle$, $\langle u_G \rangle$, $\langle u_L \rangle$ Also the velocity ratio or *slip-ratio* is a commonly used term given:

$$S = \frac{\langle j_G \rangle_G}{\langle j_L \rangle_L}. \quad (3.21)$$

The above Section 3.1.2.1 considered the governing conservation equations for single phase flow. There exist also an exact formulation of the two phase flow equations based on the Navier-Stokes equations. For the two phase flow description the evolution of the fields (velocity, pressure, temperature) are required for both phases as well as a prediction of

the geometry of the interface. These equations are laborious and for most phenomena unpractical. A short description of some of the modeling approaches for two phase flow will be described: two-fluid approach, mixture model and field models. The equations and their rigorous derivations are out of the scope of this thesis.

Two-fluid formulation is based on treating each fluid as separate media through six equations. It is based a probabilistic approach on the void fraction of the local phase. In reality the phases are separated and interact together in a symbiosis with interfacial transfer of momentum (shear) and energy. As in the for case of single phase turbulence described, new closure terms are needed in the equations. These *closure laws* are interfacial mass, momentum and energy exchange.

Mixture model is based on only one set of equations for the mixture. No information can be subtracted about the interfacial geometry, and no exchange of mass, momentum and energy over the interface are considered. This means that the evolution of the mixture is externally set and does not evolve freely.

Multifield models are based on the conservation equations, but the idea is to divide the flow into different fields. From the perspective of multifield model annular flow would consist of three fields: film flow, droplet and vapor. Closure of the model is based on the knowledge from single phase flow. The multifield model works best for flow patters where the phases are relatively uncoupled. Closely coupled flows as bubbly flow or mist flow needs a more complex closure relationship (interfacial shear and mass transfer). The model predicts poorly intermittent flows as slug flow.

3.1.2.3 Micro-channel effects

At this point the discussion has not included the effect of micro channels compared to larger channels. The term micro-channel is in it self a bit blurry, what defines the threshold for what is or is not a micro channel? Bretherton [8] showed analytically that the rise velocity of elongated bubbles in a sealed liquid capillary vanishes for

$$Bo = \frac{\rho g d^2}{\sigma} < 3.368. \quad (3.22)$$

This implies that for air-water the diameter should be less than $5mm$ to be considered as a micro channel. The correlation is not perfect since the geometry or viscosity is not accounted for. Based on experimental evidence the correlation holds well as there is a significant deviation for channels of air-water with $d \sim 5mm$ in agreement with eq.(3.22). Effects from the viscous ($\sim \rho\mu/d$) and interfacial ($\sim \sigma/d$) stress are scaled by the inverse of the diameter and considered dominating. The inertia ($\sim \rho u^2$) and gravitational ($\sim \rho g H$) stresses are often neglected. Gihaasen et al. [2] equivalently showed that, given the

Laplace length scale for micro-channel

$$\lambda = \frac{\sigma}{\sqrt{g\Delta\rho}} \quad (3.23)$$

one should not have $D < 0.3\lambda$, to be insensitive to channel orientation. The Laplace length scale is the ratio between a capillary length scale and the gravitational length scale.

3.1.3 Long Wave Theory

Long Wave Theory (LWT) or lubrication theory is one approach, which is explored to describe and understand thin film dynamics. The LWT is an asymptotic expansion of the governing equations for the study of thin film. This approach is based on reduction of the governing equations and boundary conditions. This simplification often reduces the equations into a single nonlinear partial differential equation formulated in terms of local film thickness. Other unknowns like velocity, temperature and pressure are obtained by functional solution of the differential equations. This simplification removes the well-known complexity of free boundary problem. Nonetheless the asymptotic reduced equations inherit a highly nonlinear nature with higher order spatial derivatives. A Linear Stability Theory (LST) been applied to more easily investigate the equations. The LST is concerned with the behavior and effect of perturbations in the equation. Initially, LWT assumes that the instability is of long wave, which means that the length of the initial disturbance in longitudinal direction is much larger than the film height. Consequently the disturbance $h = h_0 + h'$, $h \gg h'$. So the disturbances are small, compared with the mean film height. By inserting $h = h_0 + h'$ in the governing film equation for LWT and linearizing in primed quantities one obtain the linear stability equation. Separate solution for perturbations in time and space is sought by typically assuming a known nature of the disturbance

$$h' = \exp(ikx + st) \quad (3.24)$$

where both coefficients are independent of x and t . These are a complete set of "natural" modes that, that can be used to represent and believed to describe any disturbance. Using this in the linear equations one obtain a characteristic equation for s , in terms of wave numbers. Depending on the nature of s it is possible to predict if the perturbations will grow or they will be damped. If they are decaying (damped) the film will obtain a steady state and no film rupture. On the other hand, should they grow they are believed to rupture the film. In the case of film rupture it is of interest to obtain the most unstable wave number. This mode is presumed to be the dominant in the rupture process. The validity of the LST have been argued in literature since there seem to be a discrepancy

between results from the nonlinear equations compared with the results from the LST. Nonlinearities are especially important near film rupture.

Intermolecular forces are important when the film becomes $< 1000\text{\AA}$. Dealing with Van der Waals, repulsive and electro static forces in the film equations means that they need to be modeled. As discussed by [22] the distance between the solid and the interface governs these forces. The forces appear in the film equations as new additional source terms. The nature of the effective Hamaker constant, liquid and solid media are crucial and determining for the effects of the intermolecular forces. A correct representation is a bottle neck for obtaining a correct evolution of the fluid interface motion and rupture time.

Different models for electrostatic forces, Lennard-Jones potential and Van der Waals forces are reported in literature. All usually inherit the standard Van der Waals term from Ruckstein and Jain [23], $\phi = \frac{A'}{6\pi h^3}$. A' is the Hamaker constant. Long range molecular forces usually imply the Van der Waals forces which are presumed important in the rang of, $100 < h < 1000\text{\AA}$. It should though be noted that also electrostatic double layer forces can also be effective over a relative long range. The dimensional film equation is defined

$$\mu\partial_t h - \frac{1}{3}\partial_x[h^3\partial_x(\phi - \sigma\partial_x^2 h)] = 0. \quad (3.25)$$

The first term is representing a pseudo viscous unsteady force, the second term is excess intermolecular forces (modeled in ϕ) and the last term is stabilizing surface tension force due to local curvature. Different ways have been approached to model ϕ and some are mentioned in the review [30].

3.1.4 Summary

The theoretical basis of intermolecular forces shows that dispersion forces are always present between molecules, where the most important contribution is from the Van der Waals forces. Van der Waals forces can be significant between macroscopic bodies, as the sum of the intermolecular forces translates into an interbody force, that can either attract or repel adjacent bodies.

A macroscopic flow phenomenon is described by the governing Navier Stoke's equations i.e. hydrodynamics. Although the theoretical foundation exists, the equations are laborious and unsolvable without simplification and additional closure models. Different methods have been pursued in CMFD, interface tracking methods (one fluid formulation) are the most well developed and widely applied. Two types of interface tracking methods are applied in this thesis: VOF and Level Set method.

Thin film dynamics ($h < 100\text{nm}$) inherits a nature that can be partly described by both of the two theories: molecular dynamics and hydrodynamics. In the Long Wave Theory (LWT) these two are merged so that effects from both theories can be accounted for. The LWT shows maturity and is seen as an prospective avenue that is further pursued in this thesis. Chapter 5 shows results from, a developed computational platform for the thin film equation the LWT.

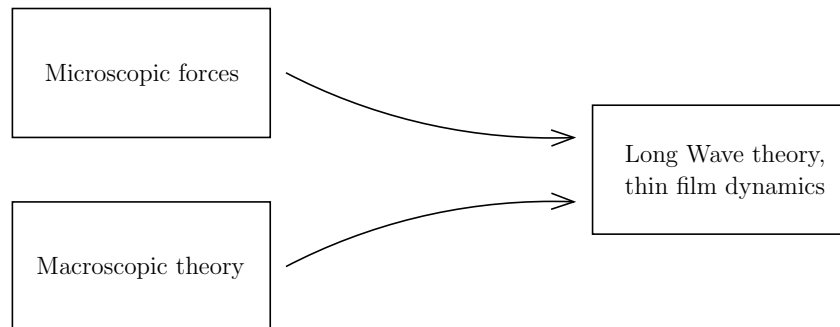


Figure 3.4: Basic forces and macroscopic theory are merged into LWT.

3.2 Numerical methods

For many problems there exist a set of governing equations, which are very difficult or impossible to solve analytically for real cases. This is the case of the Navier-Stokes equations. For such problems a discrete numerical solutions are often sought, by applying a mesh that contains discrete points where the information is defined. By interpolating between the points (Finite difference method) or between the faces a very close approximation to the analytical solution can be obtained, depending on the mesh spacing and the order of the scheme.

With the increase in CPU power the feasibility and use of Computational Multi Fluid Dynamics (CMFD) have expanded. Historically the use of numerical methods has been hindered by the CPU time, and experiments have rather been performed. In recent years this trend has shifted into a more broadened use of numerical methods in both industry and academy. The development and commercialization of CMFD codes have with growing CPU power shifted the economical costs as well it is now often cheaper to perform numerical simulations than performing experiments. Numerical simulations and physical experiments are together in a symbiosis. Good numerical simulations rest on experimental results, since results from numerical simulations always needs validation. By validating the results against experimental results, one can look at small scale features from the CFD results in which could not be visible in experiments. Physical insight on what is happening on small scale, can extend the knowledge about the large phenomena.

In this thesis, CMFD has been used as a tool to obtain insight in the slug flow phenomena in a micro channel. This section is devoted to the numerical approach where some of the basic concepts are discussed as well as methods and algorithms in multiphase flow, *Volume of Fluid* 3.2.2.1 and *Level Set* 3.2.2.2.

3.2.1 Finite Volume Method

There are different methods for solving the conservation equations. Two methods that are often used are: the Finite Volume Method (FVM) and Finite Element Method (FEM). FEM is not as widely applied as FVM in CFD. The strength of the FEM is the use of unstructured grids, which makes it easier to apply the method for complex geometries, and the method is often used for calculation in structural mechanics. Both the codes (FLUENT and TransAT) used in this thesis are based on the FVM, and for this reason a short description of the method is given.

The numerical domain consist of a grid of several discrete points, these points define small finite Control Volumes (CV). The FVM employs the conservation equations and for each of the finite CV in the domain. The discrete equations are conserving all variables in the finite control volume, just as the original equations. This is done by applying an integral form of the conservation equations for every CV and the volume integral gives us that \underline{U} (mean cell value) is represented at some point within the cell.

$$\int_{\Omega} \underline{u} dV = \underline{U} \Omega \quad (3.26)$$

$$\frac{\partial}{\partial t}(\underline{U} \Omega) + \oint_S \underline{F}(\underline{u}) \cdot \underline{n} dS = 0. \quad (3.27)$$

Where the $\underline{F}(\underline{u})$ is a flux tensor and corresponding scalar equation for U can be obtained.

$$\frac{\partial}{\partial t}(U \Omega) + \oint_S \underline{F}(u) \cdot \underline{n} dS = 0. \quad (3.28)$$

3.2.1.1 Discretization schemes and time integration methods

The accuracy of the numerical solution depends strongly on the mesh spacing, order of the scheme and time integration method. Some of the schemes that have been used are described, for interested readers I would refer to the book by Ferziger and Pèric [18].

The order of the scheme is usually determined by a Taylor expansion to find the leading discretization error also called the *truncation error*. The magnitude of the truncation error shows the accuracy of the scheme compared to the analytical solution. By enlarging the stencil (number of faces in the interpolation) the order of the scheme increases along with the accuracy. To show the methodology a first order upwind scheme is explained, for a cell centered FVM, with the flux estimated over the cell sides. The cell-value that is used for the calculations depends on the direction of the convection (fluxes) and the surface normal vector \underline{S} . So the flux is calculated from the upstream cell ($\Omega_{i,j}$) over the side AB, Figure 3.5.

$$f_{AB} = f(U_{AB}) \quad (3.29)$$

with

$$U_{AB} = U_{i,j} \text{ if } (\underline{A} \cdot \underline{S}) > 0 \text{ (outbound flux)} \quad (3.30)$$

$$U_{AB} = U_{i+1,j} \text{ if } (\underline{A} \cdot \underline{S}) < 0 \text{ (inbound flux)}. \quad (3.31)$$

For the calculations performed higher order spatial discretization schemes have been applied as the Quadratic Upwind Interpolation for Convective Kinetics (QUICK), Monotone Upstream-Centered Scheme for Conservation Laws (MUSCL), Hybrid Linear / Parabolic Approximation (HLPA) and Weighted Essentially Non-Oscillatory (WENO, for the Level Set function). The QUICK scheme is a third order scheme in the convection direction, and can inherit a small numerical overshoot. It takes three cell faces into its interpolation, as seen below, depending if there is inbound or outbound flux. For an equidistant mesh the stencil for the QUICK scheme:

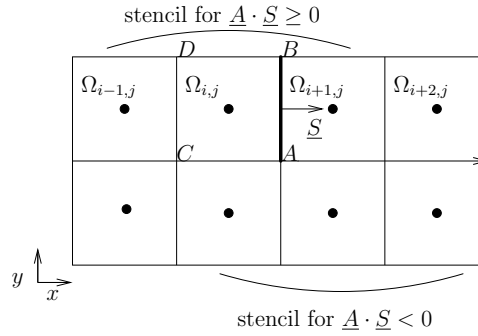


Figure 3.5: Stencil for QUICK scheme on an equidistant mesh.

$$U_{AB} = \frac{6}{8}U_{i,j} + \frac{3}{8}U_{i+1,j} - \frac{1}{8}U_{i-1,j} \quad (3.32)$$

An implicit or also called *backward Euler* method has been applied for the time integration of the conservation equations for the FLUENT calculations. We are considering the solution at the new time level and it is solved through an iterative method.

$$u_i^{n+1} = u_i^n + \Delta t F(t_{n+1}, u_i^{n+1}). \quad (3.33)$$

For the Volume of Fluid transport equation for void fraction is solved through an explicit or *forward Euler* method.

$$u_i^{n+1} = u_i^n + \Delta t F(t_n, u_i^n). \quad (3.34)$$

Also a Runge Kutta method has been applied for the calculations in TransAT. The Runge Kutta method is using the point between t_n and t_{n+1} . The method consists of several steps to obtain the solution at the next time step. For the 4th order Runge Kutta the first half $t_{n+\frac{1}{2}}$ predictor step is an explicit Euler, and the corrector step is an implicit Euler. The full step t_n is taken by a midpoint predictor step, followed by a Simpson's rule for the corrector step.

$$u_{i*}^{n+\frac{1}{2}} = u_i^n + \frac{\Delta t}{2} F(t_n, u_i^n) \quad (3.35)$$

$$u_{i**}^{n+\frac{1}{2}} = u_i^n + \frac{\Delta t}{2} F(t_{n+\frac{1}{2}}, u_{i*}^{n+\frac{1}{2}}) \quad (3.36)$$

$$u_{i*}^{n+1} = u_i^n + \Delta t F(t_{n+\frac{1}{2}}, u_{i**}^{n+\frac{1}{2}}) \quad (3.37)$$

$$u_i^{n+1} = u_i^n + \frac{\Delta t}{6} \left(F(t_n, u_i^n) + F(t_{n+\frac{1}{2}}, u_{i*}^{n+\frac{1}{2}}) + 2F(t_{n+\frac{1}{2}}, u_{i**}^{n+\frac{1}{2}}) + F(t_{n+1}, u_{i*}^{n+1}) \right). \quad (3.38)$$

Compared to multipoint methods, Runge-Kutta methods are of higher accuracy at the same order and the method inherits a larger stability domain. The problem is that it gets more expensive, since the derivatives of an n order scheme need to be calculated n -times at every step, especially for higher-order schemes compared to multipoint methods.

As the integration methods have been shortly discussed special attention needs to be devoted to the stability of these schemes. To avoid numerical instabilities it is of great importance that the stability criterion of the scheme is not violated. A Von Neumann stability analysis can be performed to determine the stability criteria for the different schemes, [18]. Special attention need to be taken for the *Explicit* methods, which are sensitive to time-step size. The Courant-Friedrich Leavy (CFL) number is often used as a measure to avoid numerical instabilities. The CFL number,

$$CFL = \frac{a\Delta t}{\Delta x} \quad (3.39)$$

express the ratio between the physical advection a and the numerical advection. For explicit methods the CFL number is strongly restricted, $CFL \leq 1$. Implicit methods can deal with higher time stepping without having numerical instabilities. A violation of the CFL condition occurs when the physical advection, a , is traveling numerically over more than a cell during one time step of the calculations, Figure 3.6.

3.2.1.2 Velocity-pressure coupling

When solving the incompressible Navier-Stokes equations numerically there can occur a problem with the coupling between of velocity and pressure. This problem with velocity and pressure coupling can give unphysical solutions, such as an oscillating pressure field. Part of the cause for this is that velocity is coupled in two equations, contrary to the pressure that is appearing just in the momentum equation. So the pressure term has no reference equation to ensure that the right pressure is obtained.

Definition of the CFL-number

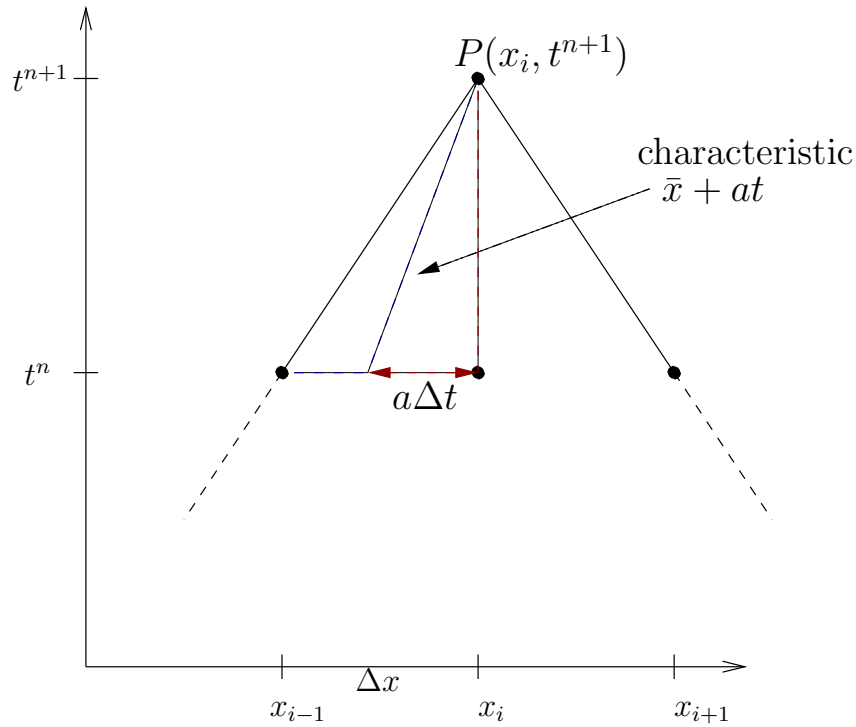


Figure 3.6: Sketch of CFL-number definition on a three point scheme, defining numerical and physical advection characteristics.

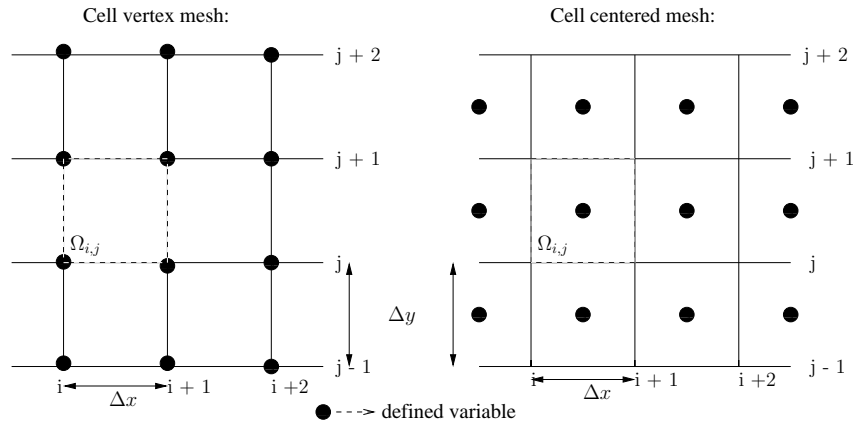


Figure 3.7: Equidistant cell centered and cell vertex meshes, (•) indicates where the variables are defined.

To avoid a velocity-pressure coupling a staggered mesh can be applied, where the pressure can be stored at the cell center and the velocity at the cell edges. The use of staggered grids can make the computations more complicated, and limit the geometry of the grid to be quadratic. The PRESsure Staggered Option (PRESTO) has been applied for the FLUENT calculation along with a Pressure-Implicit Split Operator (PISO). TransAT calculations are performed with the use of standard discretization and a Semi Implicit Momentum Pressure Linked Equations (SIMPLE).

Pressure-velocity coupling

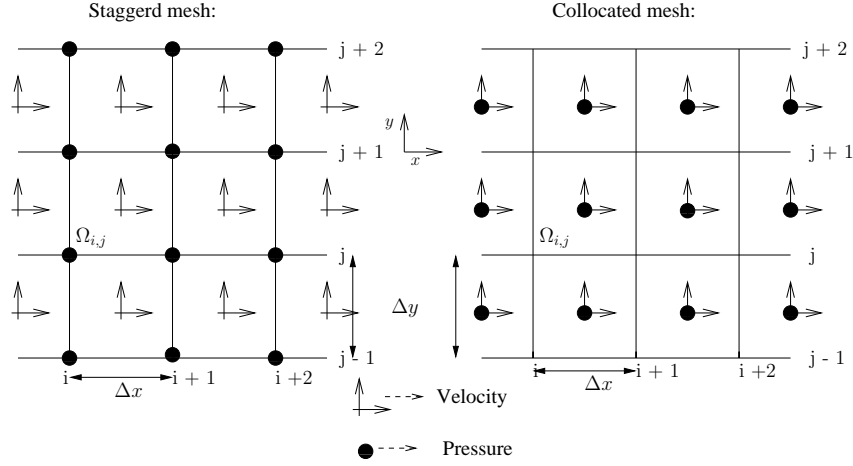


Figure 3.8: Staggered equidistant mesh, (\rightarrow) indicates velocity in x-direction, velocity (\uparrow) y-direction and (\bullet) indicates where the pressure are defined.

The velocity-pressure coupling is attained with internal iterations in the SIMPLE algorithm, that was developed in the end of the 70's by Patankar. The continuity and momentum equations are linearized with,

$$u_i^n = u_i^{n-1} + \Delta u_i \quad (3.40)$$

and neglecting the non-linear term $\Delta u_i \Delta u_j$. By some manipulation of the equations we obtain the equations for the pressure and velocity correction. u^* is the intermediate solution of the velocity. The corrections are defined as $u_i' = u_i^n - u_i^{n*}$ and $p' = p^n - p^{n-1}$. Below is a calculation steps for the SIMPLE algorithm, and similar methods taken from [18].

1. "Start the calculation for the fields at the new time t_{n+1} using the latest solution u_i^n and p^n as starting estimates for u_i^{n+1} and p^{n+1} .
2. Assemble and solve the linearized algebraic equation systems for the velocity components (momentum equation) to obtain u^{n*} .
3. Assemble and solve the pressure-correction equation to obtain, p' .
4. Correct the velocity and pressure to obtain the velocity field u_i^n , which satisfies the continuity equation, and the new pressure p^n .

For the PISO algorithm, solve the second pressure-correction equation and correct both velocity and pressure again.

For SIMPLER, solve the pressure equation for p^n after u_i^n is obtained above.

5. Return to *step 2* and repeat, using u_i^m and p^n as improved estimates for u_i^{n+1} and p^{n+1} , until all corrections are negligibly small.
6. Advance to the next time step.”

There is also other algorithms that can be used such as the SIMPLE-Revised (SIMPLER) or SIMLPE-Consistent (SIMPLEC), that are well known and extensively used.

3.2.2 Approaches on Computational Multi Fluid Dynamics

There are several different methodologies used to describe the evolution of multiphase flow. The methods discussed in 3.1.2.2 have been extended to numerical simulations.

The different types of models can be separated into field models, interface tracking methods and cellular models. Field models as the multifield models (or two equation model) solve for a void in the numerical domain, two-fluid formulation. Closure relations between the different phases or fields are crucial to correctly model and predict the transfer of mass, energy and momentum between the phases. These models typically do not explicitly predict the evolving interface between the phases, but solve the different equations depending on a preset field or phase. Many of these models are used in system codes as for reactor safety in RELAP or as in the pipe flow code OLGA.

Interface tracking methods are developed in the context of one-fluid formulation where a single set of equations are solved. These methods are applied when it is important to qualitatively determine the topology of the interface. A scalar variable is introduced in the numerical domain and solved in an additional transport equation, which is functioning as a indicator between the different phases. Consequently this means that properties are changing through the domain depending on the phase indicator. Changes in these properties are accounted for by the advection of the scalar variable. Exchange between the phases as mass and capillary forces are accounted for by introducing new source term in the equations.

Volume of Fluid, Level Set and Front-tracking are the most applied methods. VOF and Level Set will be discussed in more detail later in this section. A front tracking or Marker method is tracking the discrete particles (markers) that evolve with the flow. Two different methods can be applied Volume markers (markers are present in the whole domain) or Surface markers (at the interface). For two phase flow Surface markers are more accurate, since the interface is finely resolved. Volume markers can inherit problems with distortion of markers and may need re-meshing. Since the interface is not directly linked to the grid spacing but the number particles, this model can handle well interfaces with

complex geometries. What limits the accuracy is then the fact that the variable (velocity, pressure) scales for the fine structures at the interface is not resolved without the use of fine grids. A problem is that the particles can cluster together (need re-meshing) and that the model is unfeasible to deal with interface separation. Interface separation would for instance mean bubble break-up.

Lattice Boltzmann spring out from Lattice Gas Cellular Automata theory. The difference is that the Lattice Boltzmann Method is solving for an averaged population of the particles. Particles jump and collide from site to site, and are represented by a variable. The Lattice Boltzmann method has several attractive features as exact mass and momentum conservation. The method is also more physical than other numerical methods (as VOF and Level Set). Its downside is the strong restrictions in density ratio and the fact that it can only deal with low Re number flow.

Phase field methods as Lattice Boltzmann method inherit a more physical realism. The different phases are described through a potential field or the free energy in the system. Additional equations for the free energy is solved and linked to the NS equations. This method has been strongly restricted by computational time earlier, but recent progress of Cahn-Hilliard NS modeling show promising results, [46].

3.2.2.1 Volume of Fluid method

Volume of Fluid (VOF) is an interface tracking method that originates from Hirt and Nichols [20] in the early eighties, and is implemented in the CFD code FLUENT. VOF is a one-fluid formulation, which solves a single set of conservation equations. The different phases are distinguished by a coloring function, and is labeled *volume fraction* or area fraction for 2D. The volume fraction has no physical meaning, but is rather a numerical property. It is a scalar with the purpose to color the domain so that the different phases can be identified. If we are in the domain of liquid $c = 1$ or gas $c = 0$, and the interface is present between $0 < c < 1$.

The VOF algorithm consists of two steps: reconstruction and propagation of the interface. There exist different reconstruction methods for the interface. Most known are the 1st order Simple Line Interface Calculation (SLIC, using only horizontal and vertical lines) and 2nd order Piecewise Linear Interface Calculation (PLIC).

Of crucial importance in the reconstruction is to determine the segment orientation in the interfacial cells. This is equivalent with calculating the unit normal vector n to the segment. By the normal vector and the volume fraction one can uniquely specify the straight line in the cell (PLIC). The reconstructed interface consist then of a number of

Volume of Fluid methodology

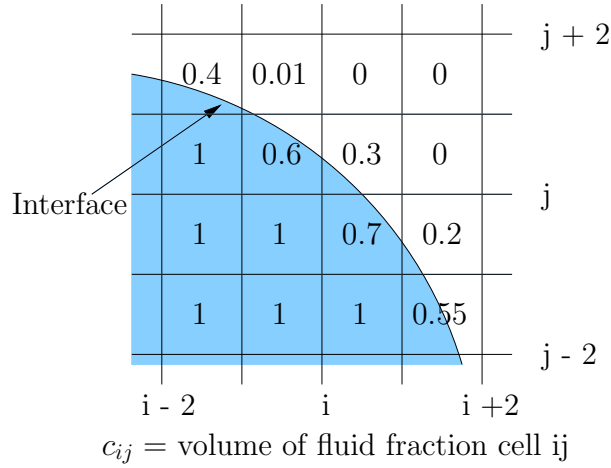


Figure 3.9: Volume of fluid methodology, by coloring of the domain by the volume fraction.

Interface reconstruction method

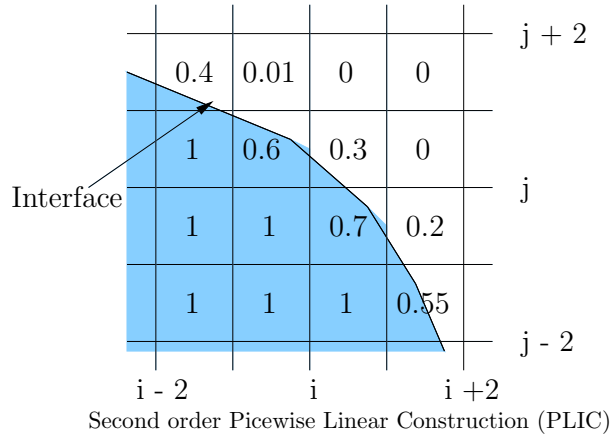


Figure 3.10: Interface reconstruction method, Piecewise Linear Interface Calculation (PLIC).

aligned segments. The accuracy of the reconstruction is crucial to determine the topology of the interface. Once the interface has been reconstructed the second step is the propagation of the volume fraction. The interface is advected with the flow field through the numerical domain. An additional scalar transport equation for the volume fraction is solved.

$$\frac{\partial c}{\partial t} + \mathbf{u} \cdot \nabla c = 0. \quad (3.41)$$

It is advected along one spatial direction at time, by either a fractional step or operator split method. This is computationally more expensive (reconstruction and solution of an additional transport equation), if compared with single phase flow calculations.

The interface that separates the two media has a value of c between 0 and 1. This

means that the interface is diffused or smeared over a number of computational cells, and the sharpness of the interface strongly depends on the mesh size Δx and Δy . The fluid and gas properties (μ, ν, ρ) are coupled through the void fraction in the domain. This can either be arithmetically or harmonically averaged. The VOF method implemented in FLUENT is using an arithmetic averaging method.

$$\mu = c_1 \cdot \mu_1 + (1 - c_1) \mu_2. \quad (3.42)$$

Other properties like density ρ are calculated in a similar manner. For the treatment of the surface tension force at the interface the Continuum Surface Force (CSF) model is implemented. This method will be discussed in more detail in 3.2.2.3.

VOF inherits a nature that has positive and negative sides. Starting with the aspects that make VOF attractive for two-phase flow simulations, we can say that it naturally conserves mass and topological changes like break-up does not need special treatment. Even though it should be noted that scale separation can then be a problem. The accuracy of the VOF method is limited for the case where the curvature κ becomes comparable with the grid spacing Δx . Then all detailed information would be lost for length scales less than Δx . Since the interface is only depending on the local values of the volume fraction the method can be fairly easily parallelized. Negative features: spurious velocity currents and smearing of material properties. The spurious velocity currents are a well-known drawback with the VOF method. They originate from the calculation of the surface tension force acting on the interface. More specifically it is an effect of the calculation of the interfacial curvature in the CSF model. Since the interface is smeared over several cells the curvature becomes "wiggly" or oscillatory. As a consequence, of the local change in curvature, spurious currents arise. The spurious currents in VOF can be reduced by employing a smoothing kernel function which takes more cell faces in its calculations, but it is computational expensive. Also the coupling of the material properties between the gas and liquid acts as a drawback to the method. Averaging eq.(3.42) between the phases implies applying incorrect material properties in the interfacial cells. This generates a numerical error, especially severe for high density and viscosity ratios. The outcome is incorrect shear stress between the two phases, a more thorough discussion of this problem is given in Section 4.3. This influences the flow pattern and then topology of the gas phase. Which then causes a global influence in the calculations.

3.2.2.2 Level Set method

As VOF the Level Set method is a one fluid model and is a similar method for interface tracking. The Level Set method was developed by Sethian and Osher [31], and imple-

mented in TransAT. A Level Set ϕ coloring function is applied to indicate the different phases. It is a geometrical function and continuous through the computational domain. The interface is explicitly located where the Level Set function is equal zero, $\phi = 0$. Material properties (μ, ρ) are based on ϕ and smoothed across the interface by a Heaviside function, $H(\phi)$. This implies that there is an amount of smearing of the properties. The ϕ function is advected with the velocity field and an additional transport equation for the Level Set function must be solved.

$$\frac{\partial \phi}{\partial t} + \mathbf{u} \cdot \nabla \phi = 0. \quad (3.43)$$

The Level Set function is in practice a signed distance function from the interface $\phi = 0$. This creates a problem for the Level Set method as the ϕ function is advected in time. As the topology of the interface changes in time, the Level Set function gets distorted. To avoid the distortion of the Level Set function it is *reinitialized* at every time step. Actually it is re-distancing the function near the interface $\phi = 0$ setting the level, so that

$$|\nabla \phi|_{\phi=0} = 1. \quad (3.44)$$

This re-distancing problem is solved in TransAT by satisfying (Sussman 1994):

$$\begin{aligned} \frac{\partial d}{\partial \tilde{t}} - \text{sgn}(\phi) (1 - |\nabla d|) &= 0 \\ d(x, 0) &= \phi(x, t) \end{aligned} \quad (3.45)$$

\tilde{t} is a pseudo time step and $\text{sgn}(\phi) = 2H(x) - 1$ is a sign function. The distance function is to be iterated until $|\nabla d| = 1$ and then correct/update the ϕ field, $d(x, \epsilon) = \phi(x, t)$, where ϵ is the elapsed time to reach convergence(, Lakehal [41]). Since eq.(3.43) is a hyperbolic equation there is no problems associated with imposing new boundary conditions (initial value) by reinitializing the ϕ function at every time step. This also assures that the interfacial thickness is uniform throughout the calculations.

Surface tension forces are modeled with the CSF model, and will be discussed in more detail in the next section.

Different aspects with the Level Set method makes it appealing for two-phase flow calculations. Since the interface is located at $\phi = 0$ there is no complications involved with the calculation of the curvature. This removes to a large extent the problem, as discussed for VOF, with spurious currents. As the interface is explicitly located, and that the material properties are smeared over few cells (1 – 2), it is feasible to couple the (almost) correct shear stress between the phases. It should though be noted that, as with VOF, even a small amount of smearing of material properties generates a numerical error. Although

Level Set has many appealing features, it also inherits unfavorable sides. Its most important disadvantage is mass loss. This comes as a consequence of the re-initialization of the ϕ field and it needs to be monitored closely. Even a small amount of mass loss can influence the accuracy in the simulation results. Especially cases with rapidly changing topology, and with curvature $\kappa \sim \Delta x$ can cause sever mass loss. Accuracy of the method is limited for the case where the curvature κ becomes comparable with the grid spacing Δx .

3.2.2.3 Continuum Surface Force model

Both FLUENT and TransAT use the surface tension forces model developed by Brackbill et. al. [7]. Brackbill et. al. wanted to specially address the accuracy of the modeling of the normal boundary condition at the interface between two inviscid incompressible fluids, $\mathbf{F}_{\text{sa}} = \mathbf{F}_{\text{sa}}^{(n)}$. For non-inviscid cases the total surface force also consist of a tangential contribution: $\mathbf{F}_{\text{sa}} = \mathbf{F}_{\text{sa}}^{(n)} + \mathbf{F}_{\text{sa}}^{(t)}$. They deduced from the Young-Laplace equation eq.(3.16) (interfacial pressure boundary condition), a normal force per unit interfacial area A at point x_s . Given for an inviscid fluids:

$$\mathbf{F}_s(\mathbf{x}_s) = \sigma\kappa(\mathbf{x}_s)\hat{n}(\mathbf{x}_s) \quad (3.46)$$

where $\hat{n}(\mathbf{x}_s)$ is the unit normal to A at the point x_s . By exploiting the use of a coloring function in multiphase flow simulations a smooth variation is obtained by interpolation. This gives the finite width of the interface h which is comparable to the grid resolution. This replaces the boundary condition problem into a continuous model. The surface tension force is then reformulated into a volume force.

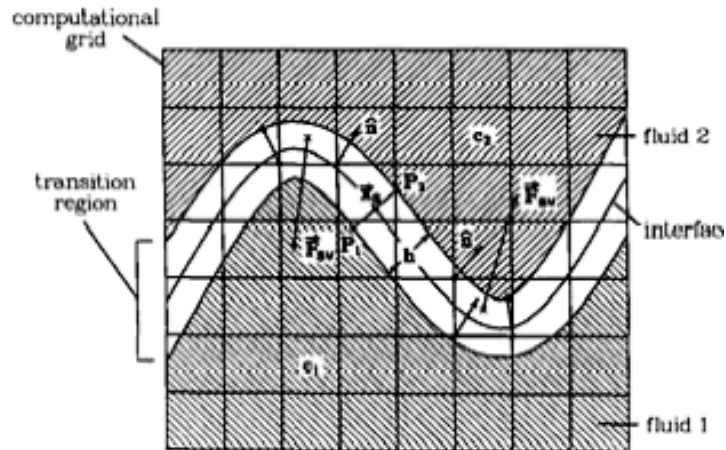


Figure 3.11: Schematic drawing of the transition region for the CSF model taken from [7].

Color function contours for media 1 c_1 and 2 c_2 , \tilde{c} are the contours in the interfacial

area where $c_1 \leq \tilde{c} \leq c_2$. The interfacial transition region has a finite width h . The normals (at cell vertices) $\hat{n} = \frac{\nabla \tilde{c}}{|\nabla \tilde{c}|}$ in the region h and the surface tension force $\mathbf{F}_{\mathbf{SV}}$ (given at cell center) from the divergence of \hat{n} .

$$\mathbf{F}_{\mathbf{SV}}(\mathbf{x}) = \sigma \kappa(\mathbf{x}) \frac{\nabla \tilde{c}(\mathbf{x})}{[c]} \quad (3.47)$$

$[c]$ is the color jump by, $c_2 - c_1$. A summary of the properties for the F_{SV} is taken from [7]:

1. "The volume force in the transition region, where the color varies smoothly from c_1 to c_2 , is designed to simulate the surface pressure on the interface between the fluids. Thus, the line integral of F_{SV} across the transition region, e.g., from P_1 to P_2 in Figure 3.11, is approximately equal to the conventional surface pressure \mathbf{x}_s is the interface point on the line $\overline{P_1 P_2}$):

$$\begin{aligned} & \int_{P_1}^{P_2} \mathbf{F}_{\mathbf{SV}}(\mathbf{x}) d(\hat{n} \cdot \mathbf{x}) \\ & \int_{c_1}^{c_2} \sigma \kappa(\mathbf{x}) \hat{n}(\mathbf{x}) \frac{d\tilde{c}(\mathbf{x})}{[c]} \\ & \simeq \sigma \kappa(\mathbf{x}_s) \hat{n}(\mathbf{x}_s) \quad \text{for } h > 0. \end{aligned} \quad (3.48)$$

2. In the limit that the width of the transition region in a direction to the interface goes to zero ($h \rightarrow 0$), the volume force becomes

$$\lim_{h \rightarrow 0} \mathbf{F}_{\mathbf{SV}}(\mathbf{x}) \delta[\hat{n}(\mathbf{x}_s) \cdot (\mathbf{x} - \mathbf{x}_s)], \quad (3.49)$$

which yield the conventional surface pressure given $\Delta p = \sigma \kappa$ "

The curvature is evaluated by the color function so that,

$$\kappa = -(\nabla \cdot \hat{n}), \quad (3.50)$$

where \hat{n} is the unit normal to the surface and the unit normal is given from the color function in the interfacial area:

$$\hat{n}(\mathbf{x}) = \frac{\nabla \tilde{c}(\mathbf{x})}{|\nabla \tilde{c}(\mathbf{x})|}. \quad (3.51)$$

So that $\kappa \cdot \nabla \tilde{c} = -\mathbf{n}(\nabla \cdot \tilde{n})$. "Since \tilde{c} is only non-zero in the transition region, the surface volume force is non-zero only in the transition region."

Calculations of the curvature and unit normal vector are done typically by the adjacent four values of \tilde{c} . $\mathbf{F}_{\mathbf{SV}}$ is introduced on the face-center or cell vertex depending on the scheme.

3.2.2.4 Remarks on the CMFD methods

VOF and Level Set are the two most widely applied interface tracking methods and current state-of-the-art. To depict both methods performance two CMFD codes have been applied, FLUENT (VOF) and TransAT (Level Set). In spite of the fact that both of these methods have previously been applied for slug flow simulations, no comprehensive comparison have been found reported in literature. By conducting such a comparison we are numerically validating the codes. Our aim is to identify numerical artifacts and suggest mitigative strategies.

Although their methodologies are similar they inherit a substantial difference, as the Level Set creates explicitly a "sharp" interface while VOF has no recollection of exact interface location. Smearing of the interface in VOF generates spurious currents, which originate from the calculation of the interfacial curvature in the CSF model. Spurious currents are a well-known drawback with the VOF method. The most important disadvantage with the Level Set method is mass loss due to the re-initialization of the Level Set function.

We notice the most attractive properties of the methods: VOF is naturally conserving mass. Level Set locates explicitly the interface. This diminishes spurious currents and makes it more comprehensible to couple properties between the phases.

The positive and negative features in the VOF and Level Set method are summarized in Figure 3.12.

Method:	POSITIVE:	NEGATIVE:
VOF	<ul style="list-style-type: none"> ● Conserving mass 	<ul style="list-style-type: none"> ● Spurious currents ● Smearing of material properties (min 2 cells) ● CPU expensive
Level Set	<ul style="list-style-type: none"> ● "Sharp" interface ● Negligible spurious currents 	<ul style="list-style-type: none"> ● Mass loss ● Smearing of material properties (min 1 cell) ● CPU expensive

Figure 3.12: Positive and negative features with the VOF and Level Set method.

Chapter 4

Evaluation of existing computational technology

4.1 Technical approach used for simulations of slug flow in a micro channel

A problem statement with gas and liquid flow in an already flowing pipe is studied with the material properties for air and water. The reason for the chosen problem is that it is interesting to study a case where a natural generation of slugs should appear. This problem statement is similar to the one studied experimentally by Pan et. al. [12]. A sketch of the initial condition for the cases used in for the simulations, Figure 4.1. The

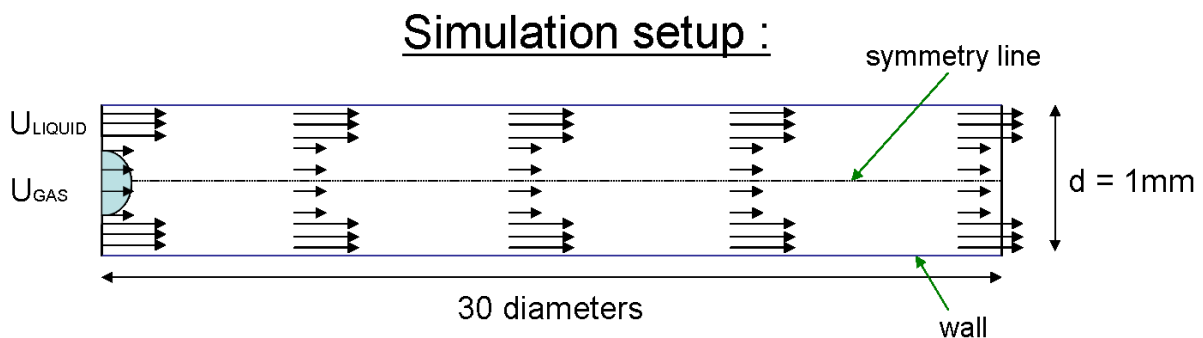


Figure 4.1: Initial condition of the simulations.

length of the pipe is long compared to the diameter, for FLUENT $\frac{L}{D} = 30$ and TransAT $\frac{L}{D} \sim 24$. This large domain is chosen to obtain a far-field effect in the axial direction. For the simulations an equidistant grid has been applied. The Table 4.1 show the different numerical schemes applied, like pressure-velocity (P-V) coupling methods:

Code	Time int.	Momentum	P-V decoupling	P-V definition
FLUENT	Implicit 1 st order	QUICK	PISO	PRESTO
TransAT	RK 2 nd order	HLLP	SIMPLE	standard

Table 4.1: Applied numerical schemes and methods.

The discretization and treatment of the color function (C-F) are gathered in a table.

Code	C-F treatment	C-F time int.	Cells	CFL_{max}
FLUENT	PLIC	Explicit 1 st order	108000	0.1
TransAT	WENO	RK 2 nd order	~ 86400	0.2

Table 4.2: Applied numerical schemes and treatment of color function (C-F), number of cells and max CFL number.

4.1.1 Comparison of simulation results with FLUENT and TransAT

The results for the three different cases are gathered and compared in the pictures below. What is clear is that there is a substantial difference in the result. These FLUENT calculations clearly show the needs for special treatment of the near wall cells as a numerical dry-out occur. This dry-out is a numerical artifact as the length scale for the fluid film (h) becomes less than the grid spacing, $h < \Delta x$. All information about length scales less than the grid spacing is lost. Physically the film height is "pushed" towards the pipe wall by the capillary forces, typically for low Ca number. As the volume fraction (for the case of FLUENT) smears the wall a numerical dry-out occur. This effect generates a unphysical solution, it is a numerical artifact. Figure 4.2, 4.4 clearly visualize the numerical dry-out. Starting with the initial conditions and material properties:

Case	U_L [$\frac{m}{s}$]	U_G [$\frac{m}{s}$]	ρ_G [$\frac{kg}{m^3}$]	ρ_L [$\frac{kg}{m^3}$]	μ_G [$\frac{kg}{ms}$]	μ_l [$\frac{kg}{ms}$]	D [m]	σ [$\frac{N}{m}$]	α [-]
1	1.11	0.66	1.22	998	$1.78 \cdot 10^{-5}$	0.0010	10^{-3}	0.0727	0.25
2	1.11	0.66	1.22	998	$1.78 \cdot 10^{-5}$	0.0010	10^{-3}	0.0727	0.36
3	1.11	1.57	1.22	998	$1.78 \cdot 10^{-5}$	0.0010	10^{-3}	0.0727	0.49

Table 4.3: Material properties, Case 1 – 3.

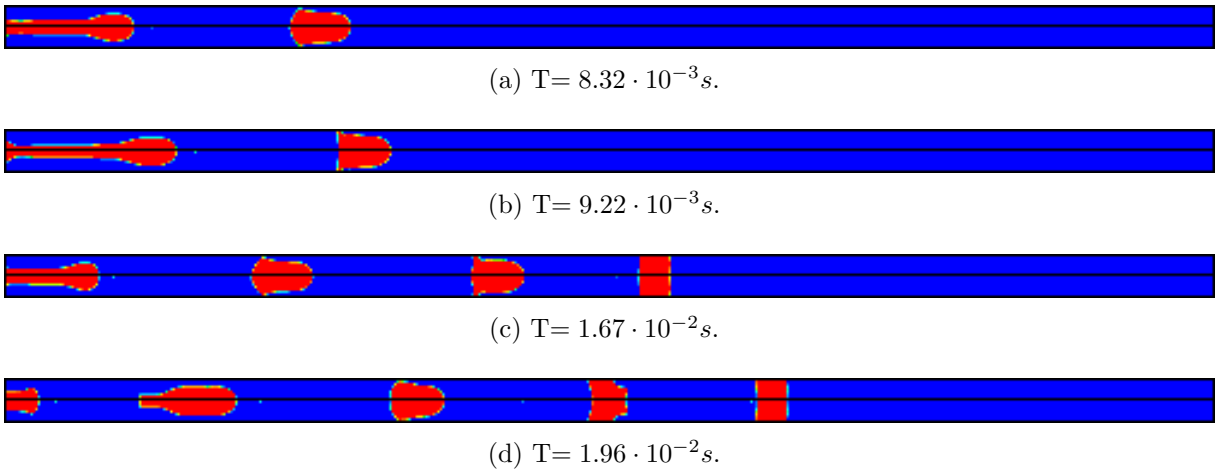


Figure 4.2: $\alpha = 0.25$ FLUENT calculations, Case 1.

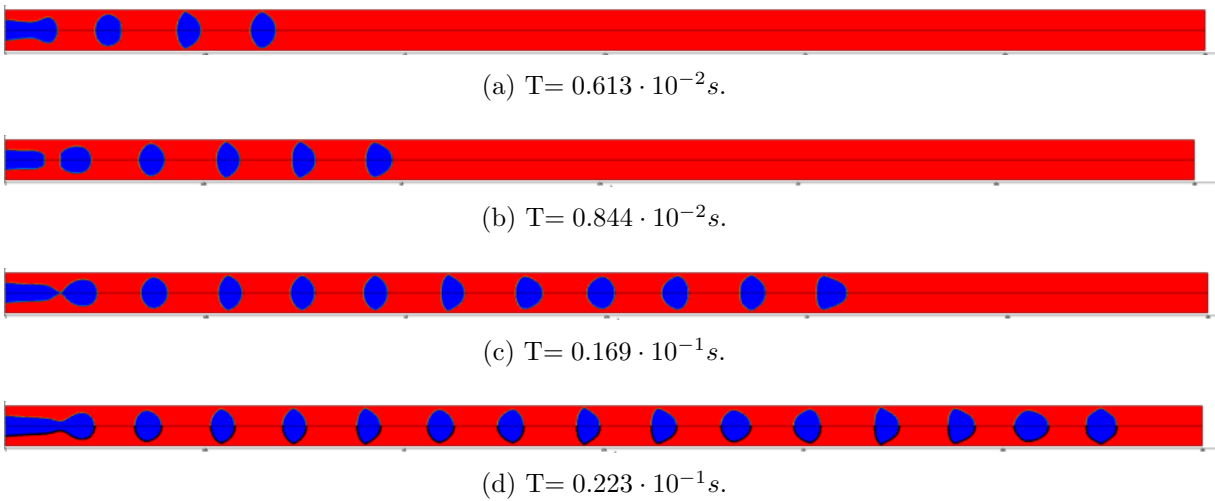


Figure 4.3: $\alpha = 0.25$ TransAT calculations, Case 1.

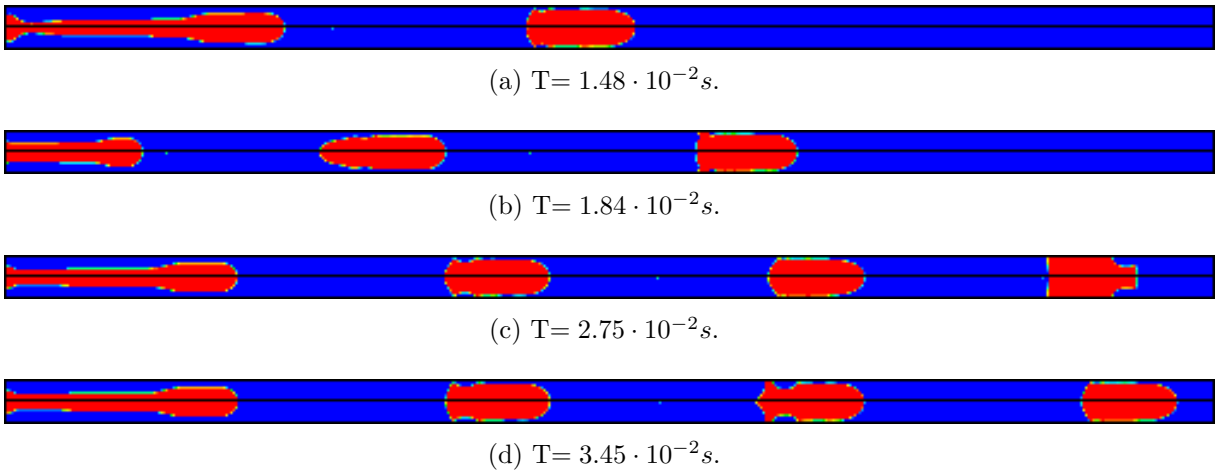


Figure 4.4: $\alpha = 0.36$ FLUENT calculations, Case 2.

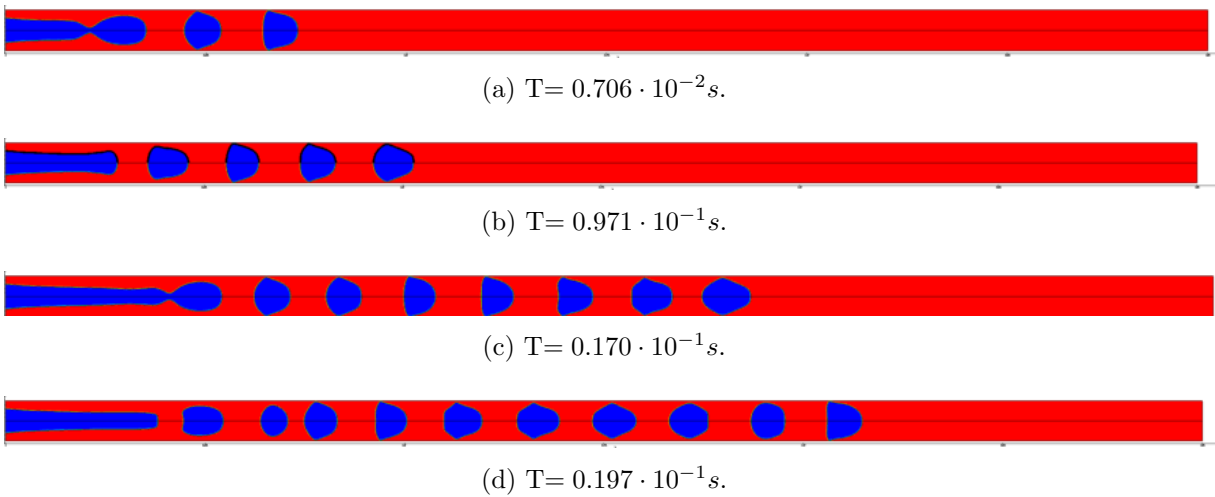


Figure 4.5: $\alpha = 0.36$ TransAT calculations, Case 2.

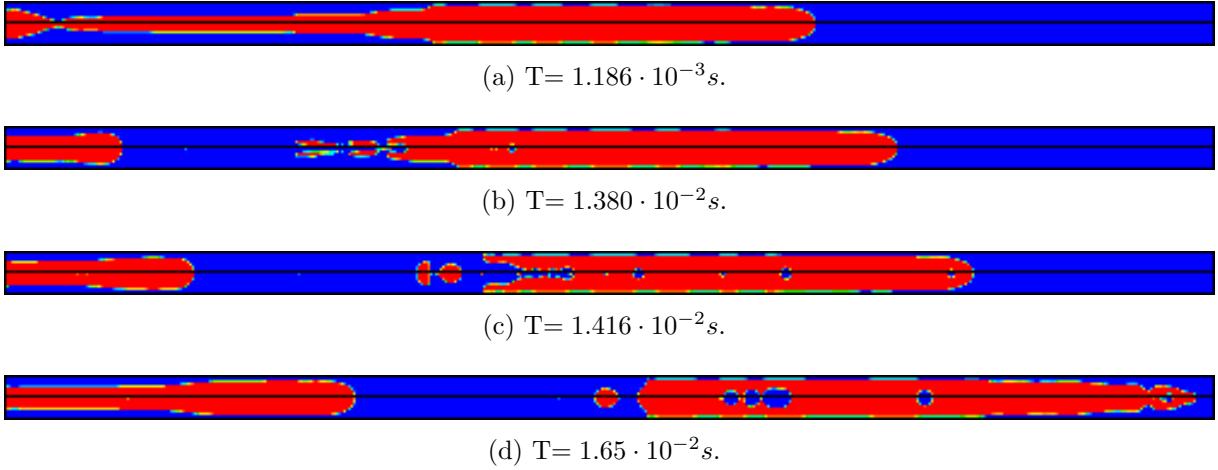


Figure 4.6: $\alpha = 0.49$ FLUENT calculations, Case 3.

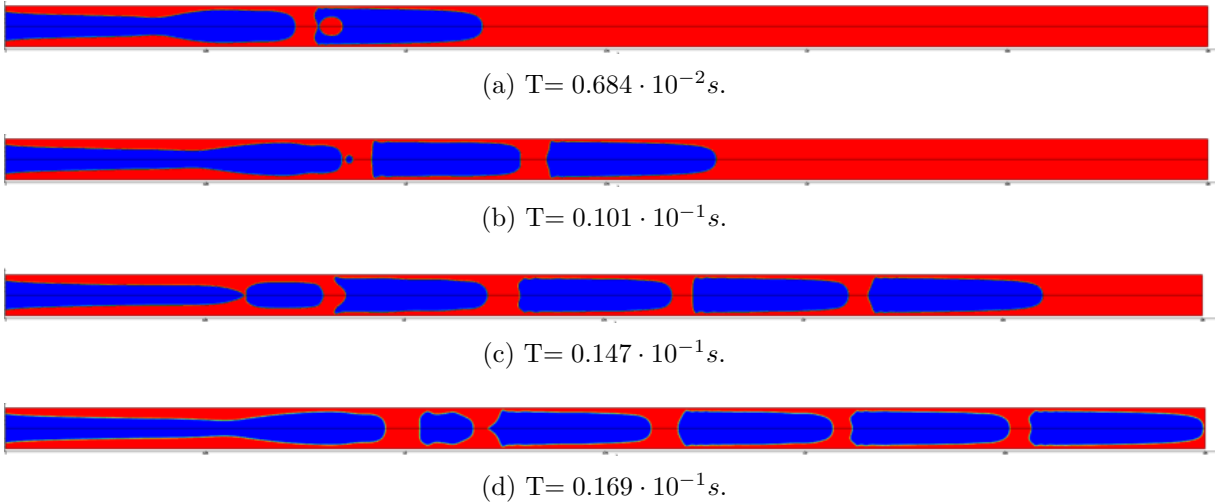


Figure 4.7: $\alpha = 0.49$ TransAT calculations, Case 3.

4.2 Adaptive Mesh Refinement in FLUENT

FLUENT compared to TransAT has a larger extent of features implemented, which we are capitalizing on. One of these features is mesh adaptation. The FLUENT calculations showed in Section 4 that a numerical dry-out occur. To overcome this problem an Adaptive Mesh Refinement (AMR) method has been applied. AMR method is a classical approach on multiscale phenomena. The AMR method is refining the mesh where the spatial volume fraction gradient is non zero, $\frac{\partial c}{\partial x_i} \neq 0$. So that the refined mesh is moving with the interface motion. Since the mesh is refined only at the interface the mesh topology are un-structured, although the mesh containing the interfacial cells is structured. The advantage with this method is that we can obtain a much sharper interface. So that small interfacial scales can be captured without the dramatic increase of computational

time, it would imply on an equidistant mesh with the same mesh resolution. A higher order spatial discretization scheme has been applied as well as a 2^{nd} order reconstruction scheme.

Code	C-F treatment	C-F time int.	Cells	CFL_{max}
FLUENT	CISAM	Explicit 1 st order	Initial ~ 108000	0.1 – 0.2

Table 4.4: Numerical schemes and treatment of color function (C-F), number of cells and max CFL number for AMR simulations.

Code	Time int.	Momentum	P-V decoupling	P-V definition
FLUENT	Implicit 1 st order	MUSCL	PISO	PRESTO

Table 4.5: Numerical schemes and methods for AMR simulations.



(a) $T = 0.315 \cdot 10^{-3} s.$



(b) $T = 0.3368 \cdot 10^{-3} s.$

Figure 4.8: FLUENT AMR results for $\alpha = 0.25$, Case 1.



(a) $T = 0.315 \cdot 10^{-3} s.$



(b) $T = 0.3368 \cdot 10^{-3} s.$

Figure 4.9: FLUENT AMR results for $\alpha = 0.36$, Case 2.

The results from the AMR simulations showed a disturbing effect, no slug flow is generated. It must be concluded that the previous results obtained with FLUENT were not converged in space. This implies that the results are mesh dependent. Slug generation on an uniform equidistant mesh is believed to be an effect of spurious current from the CSF model for the surface tension forces. By applying an AMR method the length scales for the spurious currents are separated from the "coarse" mesh. This prevents a global

influence of the spurious currents on the simulations, and localizes the effect Figure 4.10. Generations of spurious currents are clearly visible in the figure as small local numerical interfacial disturbances.

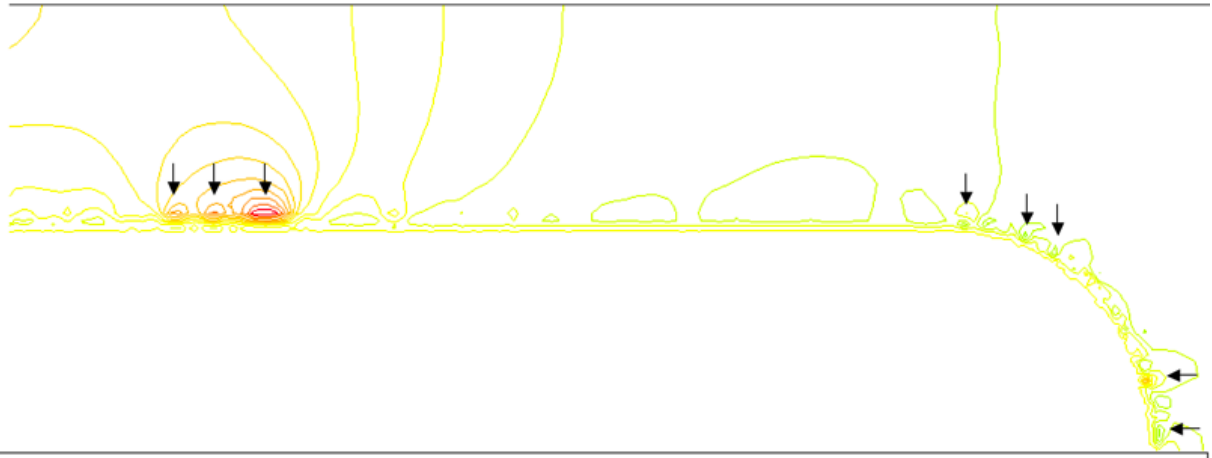


Figure 4.10: Localized effects of spurious currents localized with $\leftarrow \downarrow$ in the refined interfacial area, pressure contours.

4.2.1 AMR simulation with disturbed liquid inlet flow

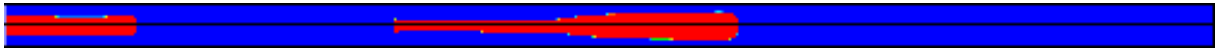
A way to numerically investigate the effects of interfacial disturbances is to introduce a disturbance in the flow at the liquid inlet. To establish if the imposed disturbance then could generate an interfacial instability that would grow into bubble pinch-off and then slug flow. T_{break} is the time for the first slug generation from the TransAT simulations for Case 1, inlet liquid velocity given,

$$U_L = 1.11 + \beta \sin\left(\frac{\pi \cdot t}{T_{break}}\right). \quad (4.1)$$

FLUENT does not generate these interfacial instabilities "naturally" which would be physical explainable. This is believed to be an effect of the smearing of the material properties in the interfacial cells along with the shear coupling. This will be discussed in more detail in 4.3.



(a) $T = 1.01 \cdot 10^{-2} s.$



(b) $T = 1.50 \cdot 10^{-2} s.$



(c) $T = 1.82 \cdot 10^{-2} s.$



(d) $T = 2.22 \cdot 10^{-2} s.$

Figure 4.11: FLUENT AMR results for $\alpha = 0.25$, $\beta = 0.1$, Case 1.



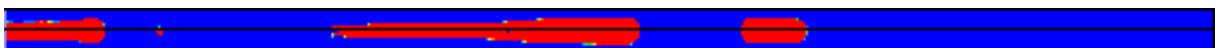
(a) $T = 3.68 \cdot 10^{-3} s.$



(b) $T = 9.13 \cdot 10^{-3} s.$



(c) $T = 1.26 \cdot 10^{-2} s.$



(d) $T = 1.63 \cdot 10^{-2} s.$

Figure 4.12: FLUENT AMR results for $\alpha = 0.25$, $\beta = 0.2$, Case 1.



(a) $T = 3.65 \cdot 10^{-3} s.$



(b) $T = 7.01 \cdot 10^{-3} s.$



(c) $T = 1.00 \cdot 10^{-2} s.$



(d) $T = 1.30 \cdot 10^{-2} s.$

Figure 4.13: FLUENT AMR results $\alpha = 0.25$, $\beta = 0.5$, Case 1.

4.2.2 Adaptation method in FLUENT

AMR is a promising method that for free surface flows can increase the accuracy and sharpness of the interfacial topology without compromising too much CPU time. It inherits some bad features, one of these is the increasing residual at every adaptation. This influences the amount of iterations needed to make the code converge. When looking at the adaptations done in the FLUENT calculations another small feature is noticed. Around the interface there is supposed to be a structured mesh with spacing $0.25\Delta x$. For curved surfaces FLUENT is too "cheap" in its adaptation method. A perfect adaptation method would not only refine the interfacial cells but also the adjacent cell. This is not required in the adaptation in FLUENT. So that for curved surfaces numerical "spikes" spring out from the interface. This is caused by the adaptation method, as an effect of small interfacial cell adjacent to a large cell. A small numerical error is expected from this. This error does not seem to grow or influence the simulation results significantly.

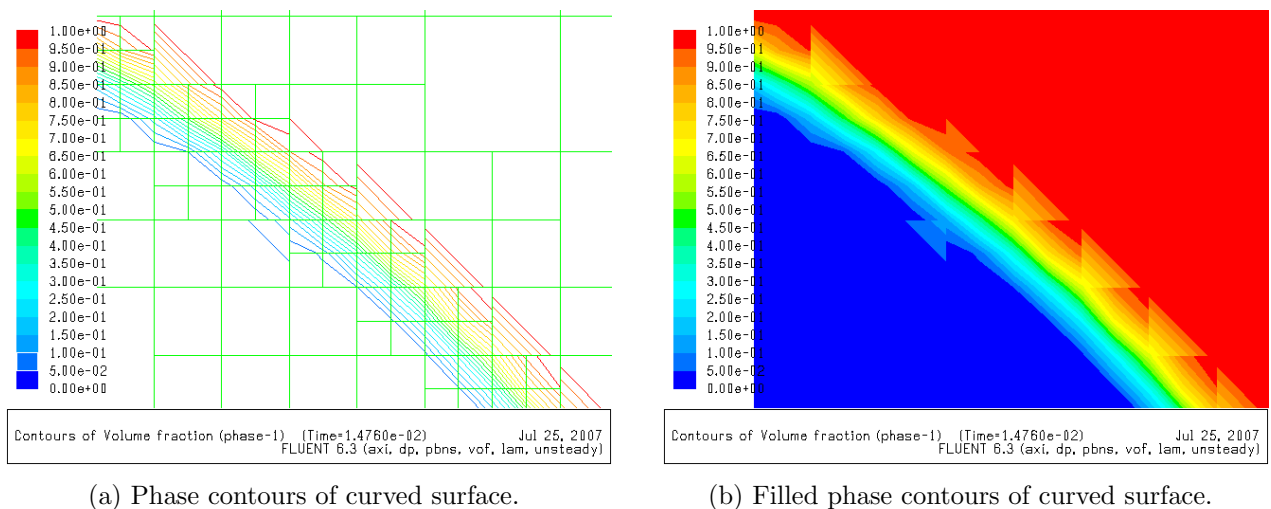


Figure 4.14: Close up on the adaptation in FLUENT on curved surface.

4.3 Critical comments on Diffuse Interface Tracking Methods

Both the VOF and Level Set methods belong to the family of interface tracking methods, that smear/diffuse the material properties over an interface of finite width. As a consequence, the shear stress and surface tension forces are smeared over the same region. Even though the region might seem to be of insignificant width, it can become a source of a plausible numerical errors. It is expected that the issue becomes severe for the problem studied in the Thesis, namely a classical stratified flow problem, where transfer of shear

stress is of crucial importance.

In a short communication Nourgaliev et al. [28] discussed previously published results from stratified flow CMFD results compared against a novel sharp interface tracking technology. Their study suggests that with the current state-of-the-art diffuse interface methods treatment it is problematic to achieve accurate description of interfacial topologies, as correct wave number for stratified flow. They relate such outcome to the property of diffuse interface.

A diversity in the obtained results from the CMFD codes highlight similar problems experienced by Nourgaliev et al. [28]. As to mitigate the numerical shortcomings and unknown artifacts the results were carefully investigated.

4.3.1 Comparison of FLUENT (VOF) and TransAT (Level Set)

At an early stage of this study a substantial difference between Fluent and TransAT simulation results was observed. These dissimilarities were visible in the topology and generation of flow field. Since already TransAT has been validated against experimental results in [26], and that the generated flow field seemed physical, a thorough investigation of the FLUENT simulations were conducted. We wanted to explain the shortcomings in the VOF in FLUENT. Three important findings are believed to cause the lack of reproduction of physics:

- Diffusion of parameters in the interfacial cells.
- Arithmetical averaging of material properties.
- Imposed parallel flow in the interfacial cells.

FLUENT diffuses the interface over 2 cells, and within these cells the parameters are smeared. The parameters can be treated in different ways within the interfacial mixed cells, either *arithmetical* or *harmonically* averaging. In either way a considerable numerical error emanates from averaging of material properties for high viscosity and density ratios. The magnitude of the numerical errors corresponds to the viscosity and density ratio.

FLUENT is arithmetically averaging the material properties, based on the volume fraction. Arithmetical averaging is favourable when the interface is perpendicular to the flow, Zaleski et. al. [6] Harmonically averaging is optimal when the interface is parallel with the flow. Arithmetical averaging with parallel interface and flow is inappropriate, since

no interfacial orientation can then be extracted. Expected recirculation patterns were not produced with FLUENT and part of the cause for this is due to the averaging. The author has experience from FLUENT VOF simulations, with high viscosity ratios ($\frac{\mu_L}{\mu_G} = 50$) and density ratios ($\frac{\rho_L}{\rho_G} = 100$), which produced expected recirculation patterns. The difference compared with the present problem statement is that the interface was perpendicular to the flow direction, Appendix A. As a consequence of the diffusion and averaging, there exists almost no interfacial shear stress in the FLUENT simulations. In spite of the fact that a shear flow is imposed in the initial condition and at the inlets, a parallel flow prevails in the mixed cells, so the two phases become "over coupled". This makes a dramatic impact on the shear stress constraint given by

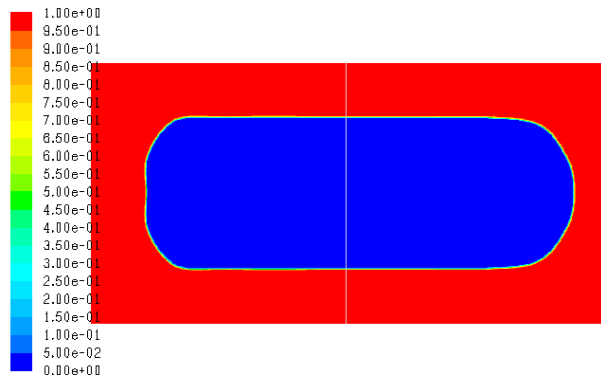
$$\mu_L \frac{\partial(u_i)_L}{\partial x_j} = \mu_G \frac{\partial(u_i)_G}{\partial x_j} \quad (4.2)$$

between the two phases. In other words, the shear stress constraint is fulfilled by no transfer of shear stress. It implies that $\mu_L \frac{\partial(u_i)_L}{\partial x_j} = \mu_G \frac{\partial(u_i)_G}{\partial x_j} \approx 0$. This makes it unfeasible to generate physical sound results, due to substantial errors in the velocity distribution. As a consequence it directly influences the two phase flow topology.

To illustrate the consequences of these effects a cross section of a slug in an AMR FLUENT simulation has been extracted. In Figure 4.15 a line visualizes the extracted cross section in the domain. Also the velocities, derivative of the velocity (in radial direction) and viscosity distribution in the cross section are plotted. A plausible "correct" velocity profile is added with red and blue lines with the assumption of a linear velocity profile. From the "correct" profile the shear stress is calculated, keeping in mind that $(\tau_L)_{FLUENT} \approx 0$ is estimated by FLUENT. The interfacial shear stress was calculated with the assumptions above: $\tau_L = \mu_L \frac{\partial(u_i)_L}{\partial x_j} = \mu_L \frac{\partial U}{\partial y} = -5.77 Pa$, proved to be far from zero.

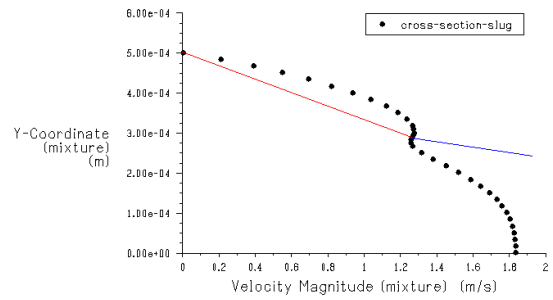
Keeping the same analogy we show the effect of property averaging in the mixed cells. We extract the viscosity from FLUENT calculations and apply it for the shear stress with the "correct" velocity derivatives: $\tau_{L,FLUENT} = \mu_L (\frac{\partial U}{\partial y})_{predicted} = -2.875 Pa$. As foreseen a large error, by 50%, is caused by the averaging alone even with the "correct" velocity derivative.

TransAT smears the interface within one cell. Since TransAT's interfacial diffusion is less and as the shear can be directly calculated at the interface $\phi = 0$, a more correct flow field is generated. The experienced recirculation patterns will not only influence the slug generation, but most certainly the bubble behaviour. Calculation of a correct recirculation pattern is of crucial importance for the diabatic case. It will have a profound effect on the temperature profile and creating an incorrect heat removal.



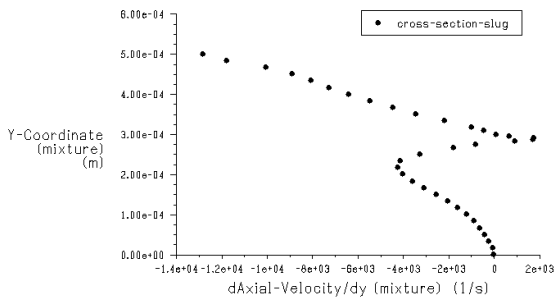
Contours of Volume fraction (phase-1) (Time=1.4760e-02) Jul 25, 2007
 FLUENT 6.3 (axi, dp, pbns, vof, lam, unsteady)

(a) Section of bubble, line where variable properties are extracted.



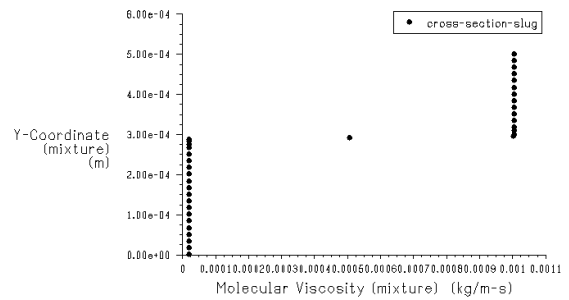
Y-Coordinate (mixture) vs. Velocity Magnitude (mixture) (Time=1.4760e-02) Jul 25, 2007
 FLUENT 6.3 (axi, dp, pbns, vof, lam, unsteady)

(b) Plotted velocity, with "predicted" (velocity red and blue lines).



Y-Coordinate (mixture) vs. dAxial-Velocity/dy (mixture) (Time=1.4760e-02) Jul 25, 2007
 FLUENT 6.3 (axi, dp, pbns, vof, lam, unsteady)

(c) Plotted derivative axial velocity in radial direction.



Y-Coordinate (mixture) vs. Molecular Viscosity (mixture) (Time=1.4760e-02) Jul 25, 2007
 FLUENT 6.3 (axi, dp, pbns, vof, lam, unsteady)

(d) Plotted viscosity in radial direction.

Figure 4.15: Effect on interfacial smearing of properties.

The generation of slug flow was briefly considered, but it needs further clarification. At the interface a disturbance generates a local curvature change, this affects the surface tension force. Inertia "stretches" the interface as the momentum (pressure) forces and surface tension force level out each other. As the surface tension forces becomes less than the momentum and inertia forces the interface pinches off and a slug is generated. For numerical simulations it is of importance to quantify if the generated interfacial disturbances are numerical or physical. Parasitic currents are assumed to cause slug flow on a "coarse" mesh in FLUENT, as this numerical disturbance gives a global influence on the results. it makes FLUENT unfeasible for this problem statement. The influence of disturbances and slug flow generation are shown by the introduction of a small disturbance in the liquid inlet in the AMR FLUENT simulations.

TransAT generates naturally a slug flow. A hypothesis is suggested for slug generation based on the insight gained from the numerical experiments in TransAT.

Slug generation: 4.3.1 *Generation of slug flow in a gas flowing into a moving liquid is assumed to be the effect of interfacial instabilities. These instabilities can be driven by: shear (recirculation), shear-inertia, and inertia.*

The rupture process is very different in FLUENT and TransAT. This is mainly due to the effect of smearing of the surface tension force. This will be discussed further in 4.3.2, but since FLUENT VOF smears the force over a larger region of mixed cells $h_{VOF} > h_{LS}$ compared with TransAT Level Set. It implies that the surface tension force is considerably different in Fluent and TransAT, in which creates a different rupture process. The author concludes that surface tension forces are wrongly estimated in FLUENT.

By comparing the performance between FLUENT and TransAT it is clear that TransAT is generating better results. FLUENT fails in delivering physically sound results, in contrary to TransAT. Computational time for the simulations is also substantially less with TransAT, even with higher residual (three magnitudes) it is roughly 30% less than in FLUENT. It is in general difficult to reach convergence with the VOF method in FLUENT.

In summary we have identified and discussed some important "unknown" numerical effects in the CMFD platforms, FLUENT and TransAT. FLUENT is incapable at the current status to deal with the horizontal slug flow phenomenon in a micro channel. Strong spurious currents generate numerical artifacts and unphysical results. TransAT captures the gross physics and is more suitable for simulations with the given problem statement.

Although a small amount of interfacial smearing generates a source term for numerical errors. The above evaluation of calculated results clearly suggests that *sharp interface method* is needed in two-phase flow simulations to overcome this problem.

4.3.2 Critical comment to the Continuum Surface Force model

The surface tension force between two media is present at the interface of an infinitesimal width. The CSF model is reformulating this force, or boundary condition, into a volume force in the diffused interfacial cells through a coloring function. Main advantage of this model is that it is general and numerically robust, and as in reality the surface tension force peaks or converges as the width of the interface reduces.

Although it inherits sides that can make it unable to accurately predict the interfacial forces. The model was originally developed for inviscid fluids, which means that the tangential force contribution is neglected. *This is not true for the problem statement in this thesis.* As observed already in the paper by Brackbill et al. [7] the oscillatory curvature (from VOF in that paper) can generate spurious currents, see [7] page 364 Fig.5. This numerical error can influence the global results in a numerical simulation, as seen from the FLUENT calculations. Even though spurious currents are not the only problem. By reformulating the surface tension force into a volume force we are automatically smearing it in the region of the mixed cells. If we would sum all contributions in the computational domain, we would come close to the analytical solution. Although, it does not correctly reproduce the physics of the surface tension force that would peak at an infinitesimal width as long as the interface has a finite width. In the CSF model it is smeared over several cells. As an unavoidable consequence this influences the calculations. For cases where the surface tension force needs to be accurately represented it fails to deliver. This is also the cause for the unphysical break-up in the FLUENT simulations, since the surface forces are diffused over the interfacial area. TransAT as well as FLUENT inherit numerical smearing of the surface tension forces. It is though substantially less diffusive, so the force is closer to the physical force (analytical solution). TransAT with Level Set is also profiting on the explicitly located interface $\phi = 0$, so that the calculation of the interfacial curvature does not produce spurious currents. Comparing the two codes one acknowledges that TransAT better captures the surface tension force, since it is less diffusive, than FLUENT.

Summarizing the findings we conclude that all diffuse interface tracking methods can inherit a substantial error for surface tension calculations with the CSF model. The simplification in the CSF model to treat both fluids as inviscid is only appropriate for limited cases, and not a generally applicable assumption. The above evaluation of calcu-

lated results clearly suggests that a *sharp interface method* is needed in two-phase flow simulations to overcome this problem.

4.4 Numerical experiments on slug flow in TransAT

4.4.1 Parameter domain

The results from FLUENT calculations proved that it is not to be feasible for horizontal slug flow simulations. TransAT produce reliable physical results and the results have been carefully investigated. Numerical simulations enable us to extract information from small-scales that are not conceivable in experiments. These small-scale details can be important to quantify for enhancement of engineering applications.

Buckingham's Pi-theorem has been applied to determine the similarity criteria (or non-dimensional numbers). The non-dimensional numbers are useful to separate the different effects. The Capillary number (Ca), Weber number (We) and Ohnesorge (Oh) number are defined:

$$\text{Capillary number: } Ca = \frac{\mu U}{\sigma}. \quad (4.3)$$

The Capillary number is expressing the ratio between viscous forces and surface tension forces.

$$\text{Weber number: } We = \frac{\rho D U^2}{\sigma}. \quad (4.4)$$

The Weber number is expressing the ratio between the fluid's inertia forces and the surface tension force.

$$\text{Ohnesorge number: } Oh = \frac{Ca}{We^{\frac{1}{2}}} = \frac{\mu}{\sqrt{\rho \sigma D}}. \quad (4.5)$$

The Ohnesorge number is expressing the ratio between viscous force and surface tension-inertia force.

Initial conditions and material properties:

Case	U_L [$\frac{m}{s}$]	U_G [$\frac{m}{s}$]	ρ_G [$\frac{kg}{m^3}$]	ρ_L [$\frac{kg}{m^3}$]	μ_G [$\frac{kg}{ms}$]	μ_L [$\frac{kg}{ms}$]	D [m]	σ [$\frac{N}{m}$]	α [-]
1	1.11	0.66	1.22	998	$1.78 \cdot 10^{-5}$	0.0010	10^{-3}	0.0727	0.25
2	1.11	0.66	1.22	998	$1.78 \cdot 10^{-5}$	0.0010	10^{-3}	0.0727	0.36
3	1.11	1.57	1.22	998	$1.78 \cdot 10^{-5}$	0.0010	10^{-3}	0.0727	0.49
4	1.11	1.57	1.22	998	$1.78 \cdot 10^{-5}$	0.0010	10^{-3}	0.0727	0.36

Table 4.6: Material properties, Case 1 – 4.

Case	U_B [$\frac{m}{s}$]	$S = \frac{U_L}{U_G}$	Ca_G	Ca_L	Ca_B
1	1.54	1.68	0.00016	0.01531	0.0212
2	1.41	1.68	0.00016	0.01531	0.0194
3	1.27	0.707	0.00038	0.01531	0.0176
4	2.53	0.707	0.00038	0.01531	0.0350

Table 4.7: Bubble velocity, slip ratio and Capillary number, Case 1 – 4.

Case	We_G	We_L	We_B
1	0.00731	16.91	32.4
2	0.00731	16.91	27.2
3	0.04136	16.91	22.27
4	0.04136	16.91	88.18

Table 4.8: Weber number, Case 1 – 4.

Case	Oh_G	Oh_L	Oh_B
1	0.00189	0.00372	0.00372
2	0.00189	0.00372	0.00372
3	0.00118	0.00372	0.00372
4	0.00118	0.00372	0.00372

Table 4.9: Ohnesoge number, Case 1 – 4.

4.4.2 Numerical results and discussion

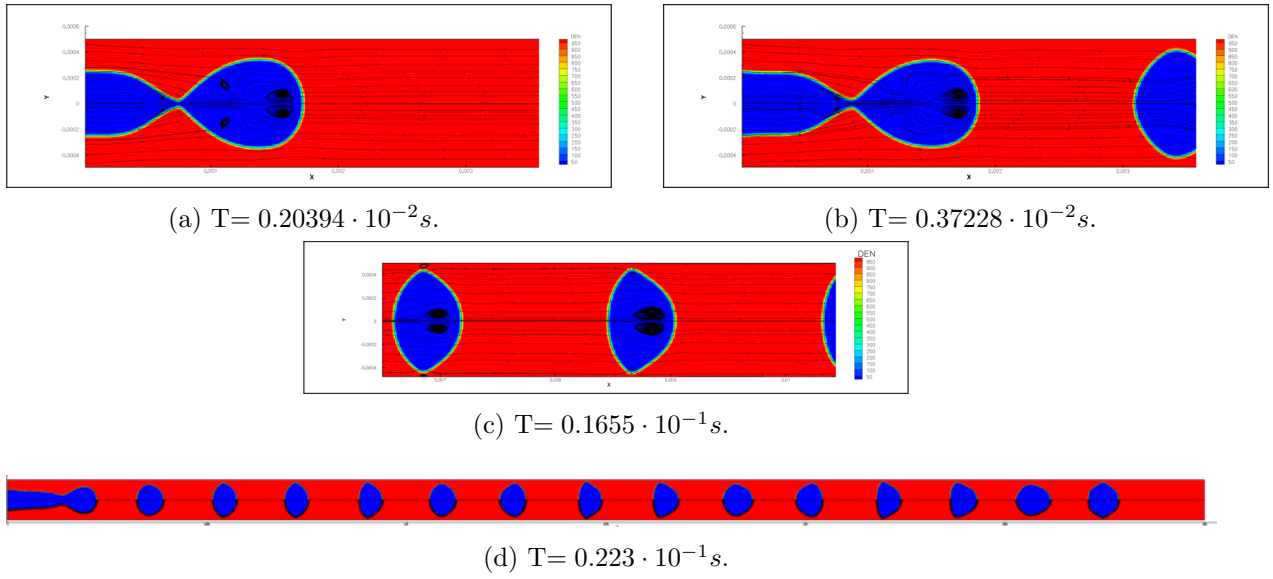


Figure 4.16: Contours of the densities with streamlines and isoline for $\phi = 0$, Case 1.

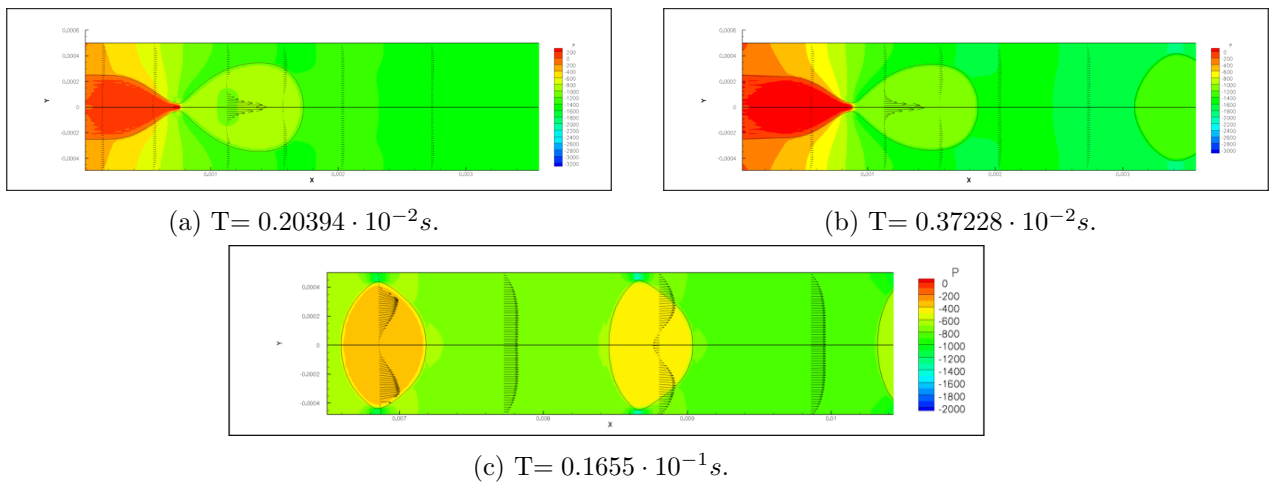


Figure 4.17: Contours of the pressure with velocity vectors and isoline for $\phi = 0$, Case 1.

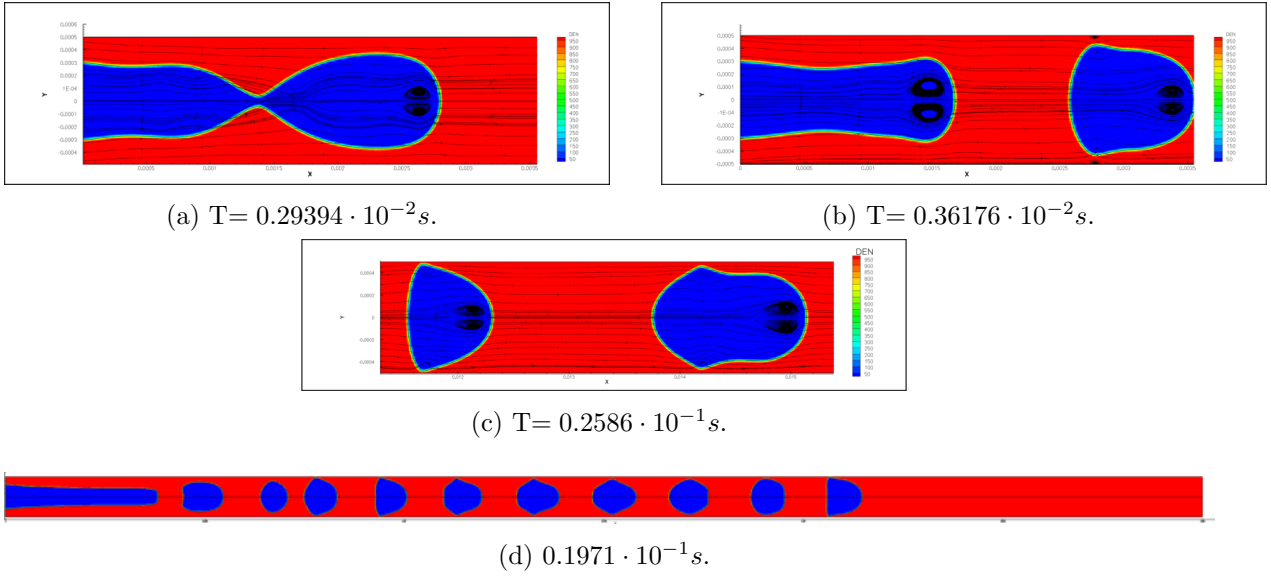


Figure 4.18: Contours of the densities with streamlines and isoline for $\phi = 0$, Case 2.

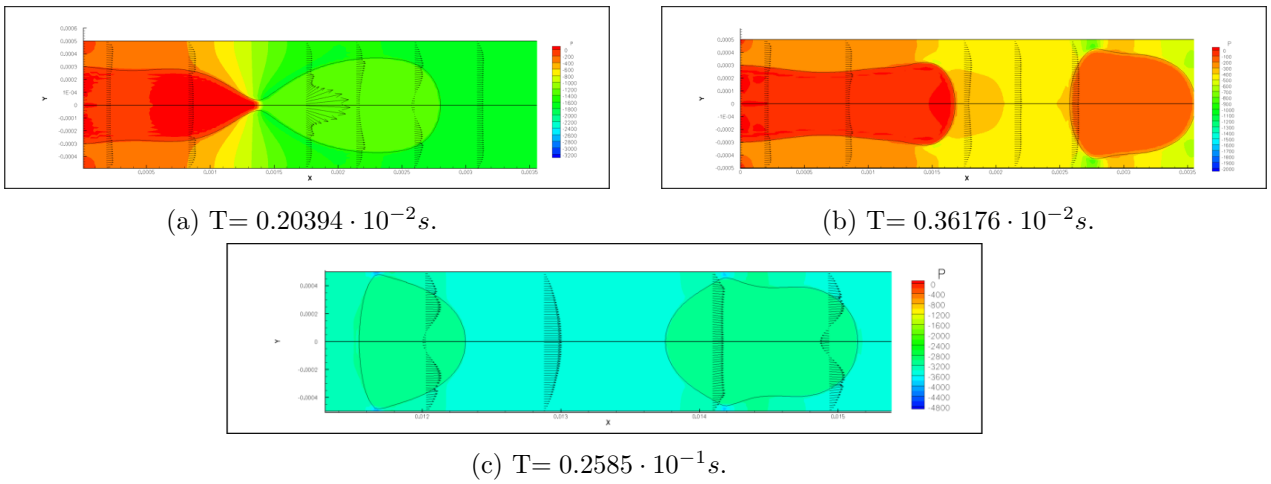


Figure 4.19: Contours of the pressure with velocity vectors and isoline for $\phi = 0$, Case 2.

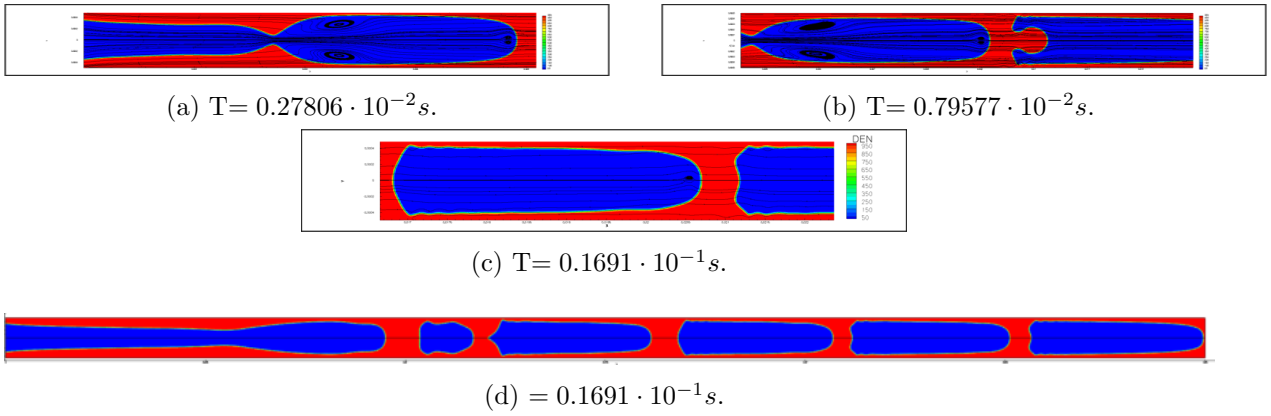


Figure 4.20: Contours of the densities with streamlines and isolate for $\phi = 0$, Case 3.

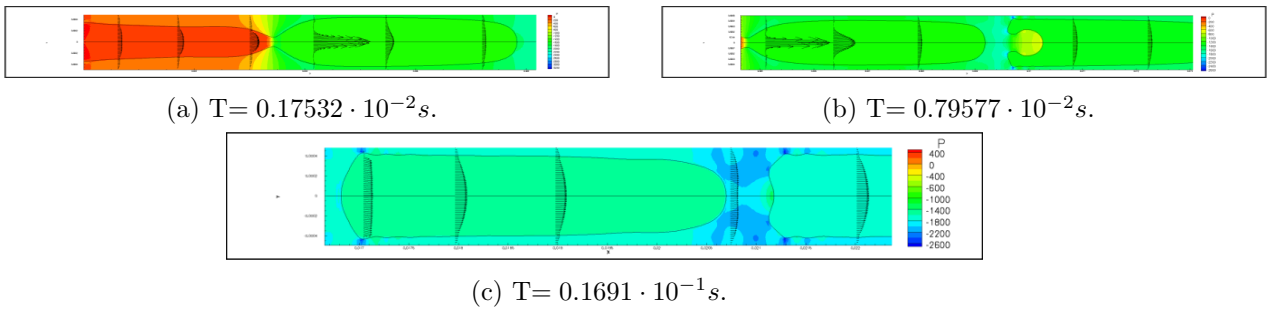


Figure 4.21: Contours of the pressure with velocity vectors and isolate for $\phi = 0$, Case 3.

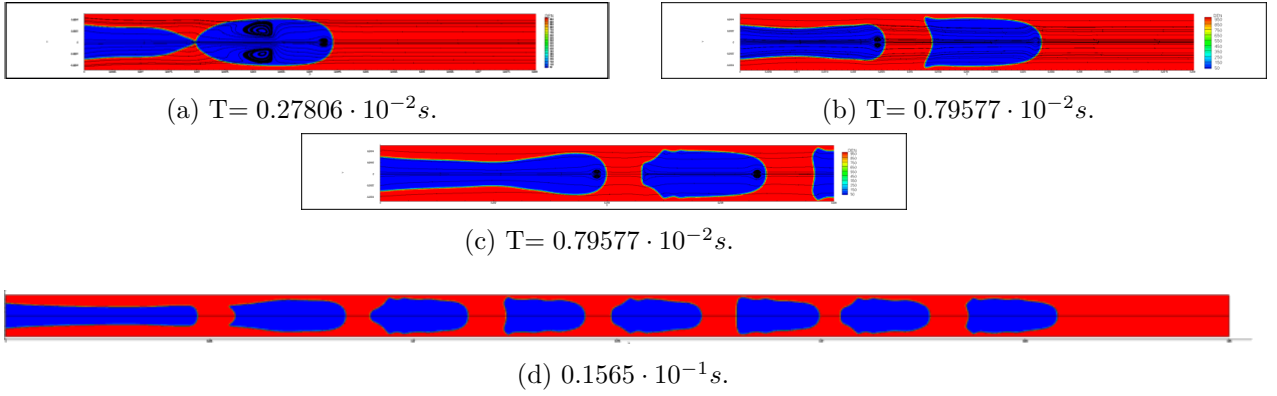


Figure 4.22: Contours of the densities with streamlines and isline for $\phi = 0$, Case 4.

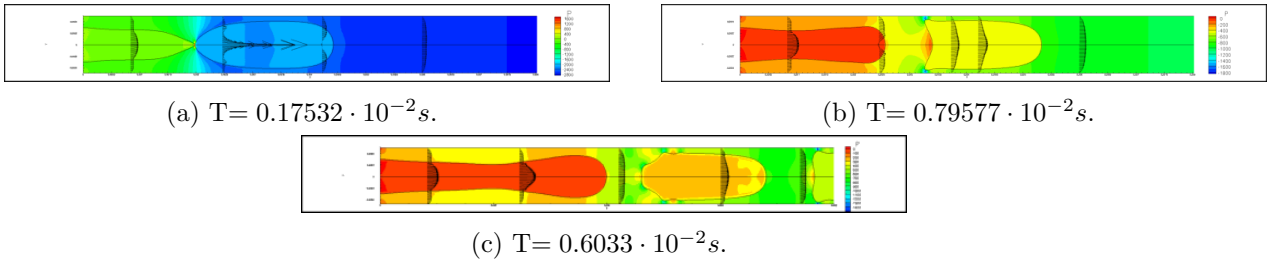


Figure 4.23: Contours of the pressure with velocity vectors and isline for $\phi = 0$, Case 4.

Four different cases have been examined with dissimilar inlet void fraction, velocity and slip ratio. We want to quantify flow features as: recirculation pattern, flow field and pressure drop. These aspects are visualized in the figures above and below.

Case 1 and 2 generates a bubbly flow pattern. As the bubbles travels downstream their front and rear are contract and expand, a "wobbling" nature. Case 2 shows that with increasing inlet void fraction, the time and length to bubble pinch-off are prolonged.

Case 3 and 4 generates a slug flow pattern, elongated bubbles. Their topology are similar to the experimental results from Pan et. al. [12], and they labeled these patterns in micro channels as a "slug train" pattern. Case 4 has a topological characteristics that are often mentioned for slug flow, a comparison of Figure 2.3 shows striking similarities. The slug has a smooth elliptic front with "ripples" along the sides and a round rear.

The effective pipe pressure drop has been mapped together in Figure 4.24. It is observed that each bubble generates a pressure drop. One can deduce that the pressure drop correlates to the inlet void fraction, bubble length and bubble velocity.

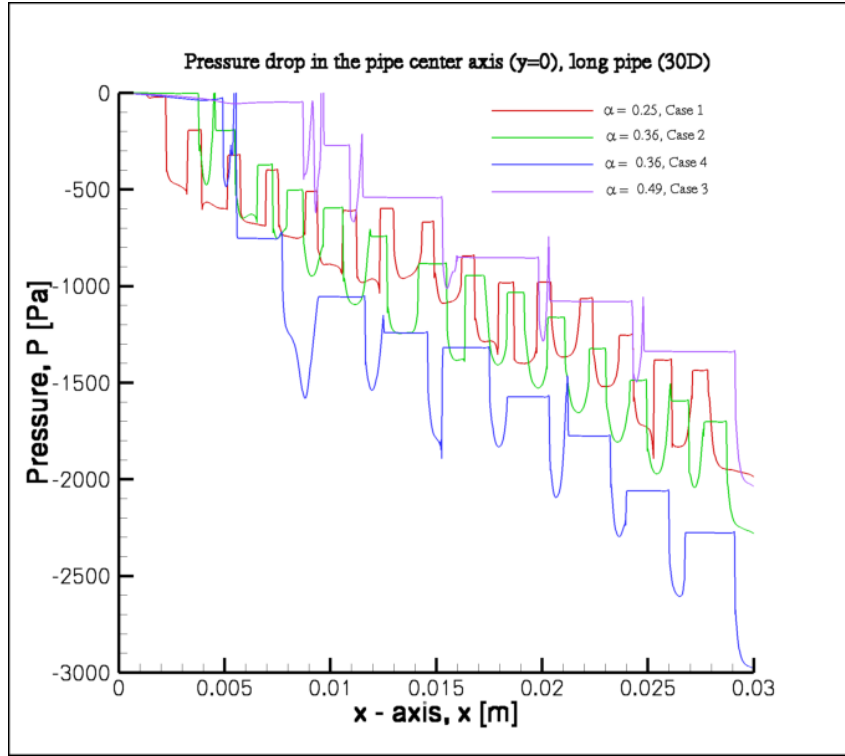


Figure 4.24: Pressure drop in long pipe ($\sim 24D$) for Case 1 – 4.

4.4.3 Remarks about the fidelity of TransAT

FLUENT VOF has already shown incapacities to generate accurate physical results for thin film slug flow. Although TransAT generates physical sound results for macroscopic slug flow, we suspect that within a certain parameter domain it will fail to deliver. Our aim is here to depict the fidelity of TransAT.

A parameter domain of low Ca number has been generated in order to form a thin bounding liquid film;

Case	U_L [$\frac{m}{s}$]	U_G [$\frac{m}{s}$]	ρ_G [$\frac{kg}{m^3}$]	ρ_L [$\frac{kg}{m^3}$]	μ_G [$\frac{kg}{ms}$]	μ_l [$\frac{kg}{ms}$]	D [m]	σ [$\frac{N}{m}$]	α_i [-]
5	0.111	0.066	1.22	998	$1.78 \cdot 10^{-5}$	0.0010	10^{-3}	0.0727	0.36

Table 4.10: Material properties, Case 5.

As the interface approaches the wall the bounding film is "lost" in the wall adjacent cell, and as a consequence a numerical dry out occur. The dry-out is a numerical artifact as an effect of discrete grid spacing. The unphysical behavior can be observed immediately as the dry-out takes place, as an instantaneous change in bubble topology. The fact that the bounding lubricating film is lost causes the gas to get in direct contact with the wall.

Case	$S = \frac{U_L}{U_G}$	U_B [$\frac{m}{s}$]	Ca_G	Ca_L	Ca_B
5	1.68	—	$1.6 \cdot 10^{-5}$	0.00153	—

Table 4.11: Bubble velocity, slip ratio and Capillary number, Case 5.

Case	We_G	We_L	We_B
5	$7.31 \cdot 10^{-5}$	0.1691	—

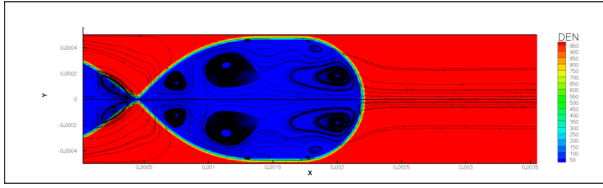
Table 4.12: Weber number, Case 5.

Case	Oh_G	Oh_L	Oh_B
5	0.00188	0.00372	—

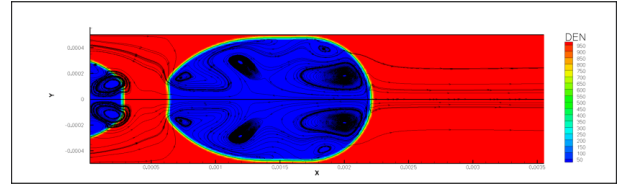
Table 4.13: Ohnesoge number, Case 5.

This implies that the shear stress at the bubble interface and wall inherits a substantial numerical error.

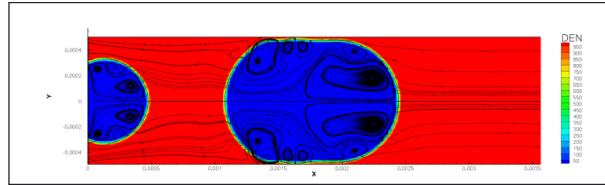
The results verify our suspicions about the fidelity of TransAT for thin film slug flow. It demonstrates that special treatment is needed to adequately capture the physics in the multiscale phenomenon thin film slug flow.



(a) $T = 0.2623 \cdot 10^{-1} s.$



(b) $T = 0.2652 \cdot 10^{-1} s.$

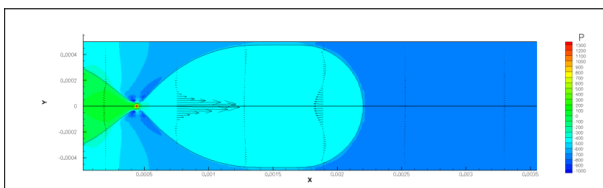


(c) $T = 0.2891 \cdot 10^{-1} s.$

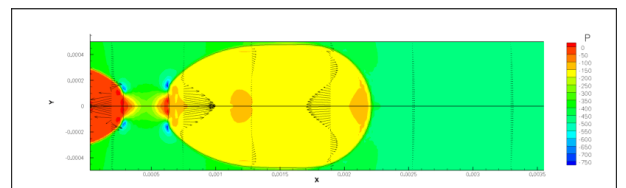


(d) $T = 0.293 \cdot 10^{-1} s.$

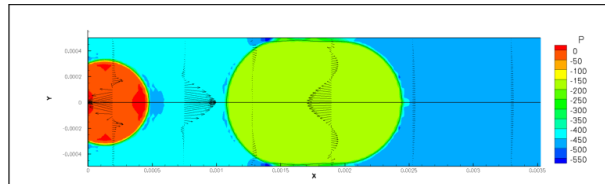
Figure 4.25: Contours of the densities with streamlines and isline for $\phi = 0$, Case 5.



(a) $T = 0.2623 \cdot 10^{-1} s.$



(b) $T = 0.2652 \cdot 10^{-1} s.$



(c) $T = 0.2891 \cdot 10^{-1} s.$

Figure 4.26: Contours of the densities with streamlines and isline for $\phi = 0$, Case 5.

4.4.4 Multiscale phenomena in slug flow

Simulation results from both CMFD codes show that they fail to deliver physically sound results for the multiscale phenomenon of thin film slug flow, Figure 4.2, 4.4, B.11. To visualize clearly the multiscale nature of the phenomena a sketch is given.

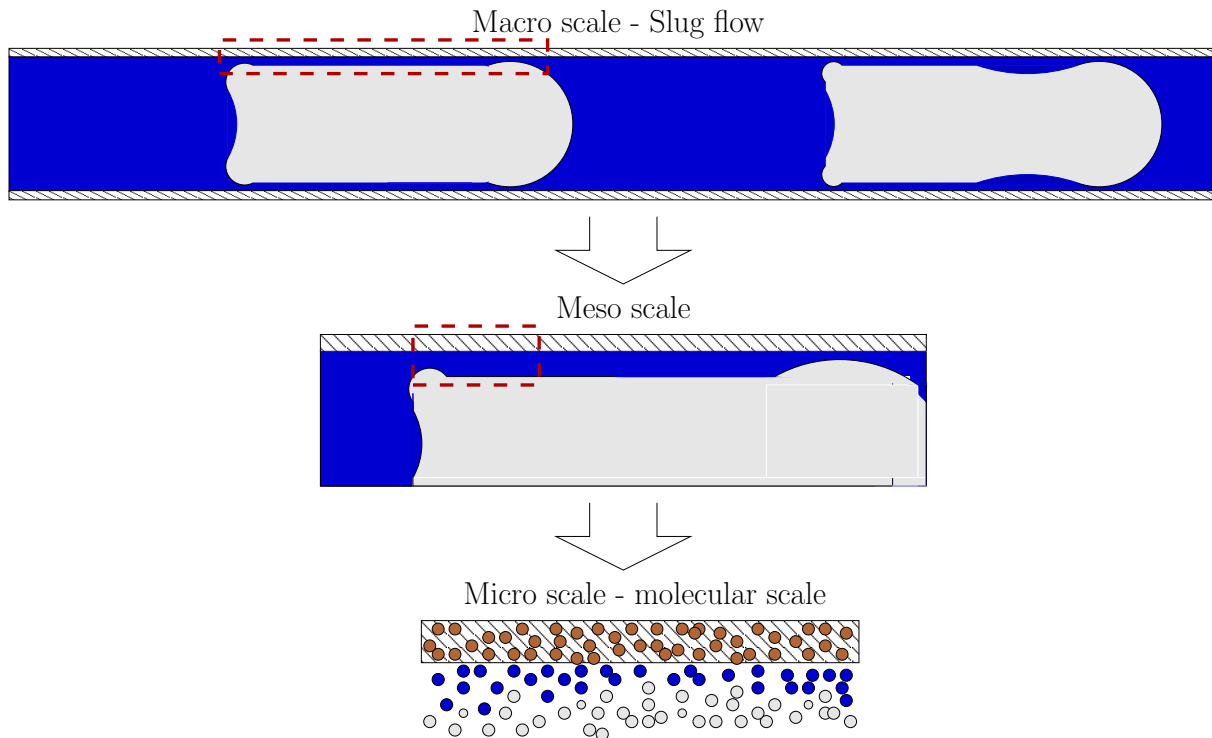


Figure 4.27: Multiscale problem in slug flow.

The problem statement has used material properties for air and water. If we make the assumption of fused quartz as the pipe material, the effective Hamaker constant would be $A = 0.83 \cdot 10^{-20}$. Molecular dynamics theory guarantees that the water film, bounded by quartz and air, will never rupture. This implies for the isothermal case that there will always be a film lubricating the pipe wall. The thin film can be resolved by CMFD, but with a high computational cost. If the height h becomes less than $100nm$ new intermolecular forces will determine the film topology. This makes CMFD simulations unfeasible to capture the physics in the thin film. To capture the dual nature and influence from the micro-scale on a macro-scale solver, a multiscale methodology is proposed. A micro-scale solver is introduced as a Sub-grid Scale model for the microscopic thin film, coupled with a macro-scale CMFD code. This preserves that perturbations from the micro scale can propagate up scale and evolve on the macro-scale. This novel technique for a multiscale coupling between a SGS thin film model and a CMFD code is developed and further discussed in Chapter 6.

Chapter 5

Development and evaluation of a mechanistic micro-scale model for thin film dynamics

The existing computational methods for multiphase flow (VOF, Level Set) simulations failed to deliver accurate results for the multiscale phenomenon of thin film slug flow. This proves the need for special treatment of the lubricating film formed between the pipe wall and the bubble interface. To numerically study thin film slug flow a multiscale approach is needed to obtain high fidelity simulations without the sacrifice of unreasonable high computational time. In the spirit of multiscale methodology a coupling between the micro/meso and macro scale is needed. A computational platform has been developed to capture the physics of the micro/meso scale through the Long Wave Theory for thin film dynamics. This advanced micro-scale model from LWT is proposed coupled with the macro-scale CMFD model with a Level Set method (TransAT). By coupling the micro- and macro-scale model the main tendencies or behavior from the micro scale can evolve on the macro scale through a *multiscale coupling*. Multiscale methodology will be discussed in detail in Chapter 6.

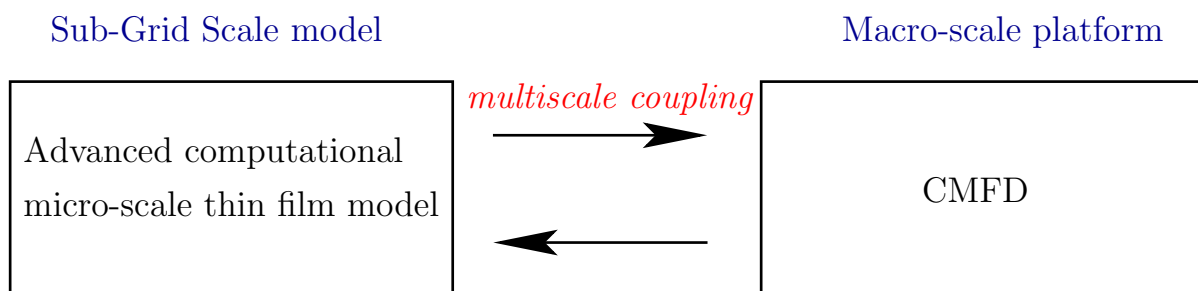


Figure 5.1: Multiscale coupling between two developed computational platforms.

Before going into the multiscale coupling methodology, validation and physical insight are sought by investigating results obtained from the micro-scale thin film model. Both a parametric study as well as a case study have been performed to determine the influence of: *retardation forces, antagonistic attractive forces, mean initial film height, Hamaker constant.*

5.1 Development of a computational platform for the thin film equation

A computational platform for the dimensional 3.25 and non-dimensional 5.3 thin film equation have been developed in MatLab. This is a 4th order stiff partial differential equation in terms of local film thickness H , that has been solved numerically with a finite difference method. Since the equation is stiff special care must be taken since it is sensible to space and time stepping, it becomes easily numerically unstable. This is solved by applying a *Gear method* for the time integration which has been reported with good results in literature [24]. The Gear method is suitable for solving stiff partial differential equations since it is adjusting size of the time stepping to avoid numerical instabilities. Periodic boundary conditions have been applied at the axial ends (east and west).

5.2 Evaluation of the computational platform for the non-dimensional thin film equation with intermolecular forces

The isothermal thin film model with inclusion of intermolecular forces has been chosen to be appropriate for the present work. To determine the effect of antagonistic attractive (Van der Waals) forces, stabilizing surface tension force and repulsive forces the non-dimensional film equation have been investigated, following the analogy from Bruelbach et. al. [9]. Starting point is the film equation eq.(3.25), that are non-dimensionalized. Using $S(a, b) = \nu^a h_0^b$ to non-dimensionalize the equation a and b are parameters tuned to make the terms non-dimensional in space. The non-dimension film height is given $H = \frac{h}{h_0}$ where h_0 is the initial mean film thickness, h is local film thickness. The non-dimensional equation with the use of $\phi = \frac{A'}{6\pi h^3}$ is:

$$\partial_t h + \frac{A'}{6\pi\mu} \partial_x \left(\frac{\partial_x h}{h} \right) + \frac{\sigma}{3\mu} \partial_x (h^3 \partial_x^3 h) = 0 \quad (5.1)$$

Substituting $H = \frac{h}{h_0}$,

$$\partial_t H + \frac{A'}{6\pi\mu} \partial_x \left(\frac{\partial_x H}{H} \right) + \frac{\sigma}{3\mu} \partial_x (H^3 \partial_x^3 H) = 0 \quad (5.2)$$

Non-dimensionalizing the Hamaker terms and surface tension terms $A = \frac{A'}{6\pi\mu} * S(-2, -1) = \frac{A'}{6\pi\mu\nu^2 h_0}$, and $C = \frac{\sigma}{3\mu} * S(-1, 1) = \frac{\sigma h_0}{3\mu\nu}$ gives the non-dimensional film equation,

$$\partial_t H + A \partial_x \left(\frac{\partial_x H}{H} \right) + C \partial_x (H^3 \partial_x^3 H) = 0 \quad (5.3)$$

similar to the one obtained in Burelbach et al. [9]. Scaling the equations with the help of two scaling parameters, $X = \left(\frac{A}{C}\right)^{\frac{1}{2}} x$ in space and $T = \frac{A^2}{C} t$ in time, and by applying the chain rule for the derivatives one obtain the scaled non-dimensional equations for film height with constant surface tension coefficient and long range Van der Waals forces as in [9], non-dimensional scaled film equation:

$$\partial_T H + \partial_X \left(A \frac{\partial_X H}{H} \right) + \partial_X (C H^3 \partial_X^3 H) = 0 \quad (5.4)$$

This is a 4th order stiff partial differential equation in terms of local film thickness H . The non-dimensional film equation consist of three terms: pseudo viscous term, excess intermolecular forces and surface tension forces. ϕ is the intermolecular forces that contains the sum of long range attractive (destabilizing) and repulsive (stabilizing) short range potentials. Surface tension force is always trying to stabilize the film. For the validation of the code the result for the non-dimensional isothermal thin film with intermolecular Van der Waals potential $\Phi = AH^{-3}$ from [9] has been reproduced. With the use of the constants in eq.(5.4) $A = C \sim 1$ also used in [9], results from both film topology and rupture time match well. In figure 5.2 the effect of long range Van der Waals forces are obvious. The attractive long range forces accelerate the film toward the solid surface and it results in film rupture. To state the effects of short range stabilizing repulsive forces a typical Lennard-Jones potential defined,

$$\phi = a_3 h^{-3} - a_9 h^{-9} \quad (5.5)$$

has been investigated, similar to the one used by Mitlin and Petviashvili [27]. Mitlin and Petviashvili [27] investigated Born repulsion in the film and the results showed kinetically stable film structures or patterns. Including the non-dimentional form of eq.(5.5) in the eq.(5.4) shows the effect of the repulsive forces. Kinetically stable patterns are generated and the results coincide with the results obtain by Mitlin and Petviashvili et. al. [27]. A pseudo wetting behavior is experienced, as the system goes into equilibrium, where a droplet resting on a thin liquid film of H_{min} . A short analysis shows that the minimum film height is depending on the ratio between the constants A_3 and A_9 . For stable steady state

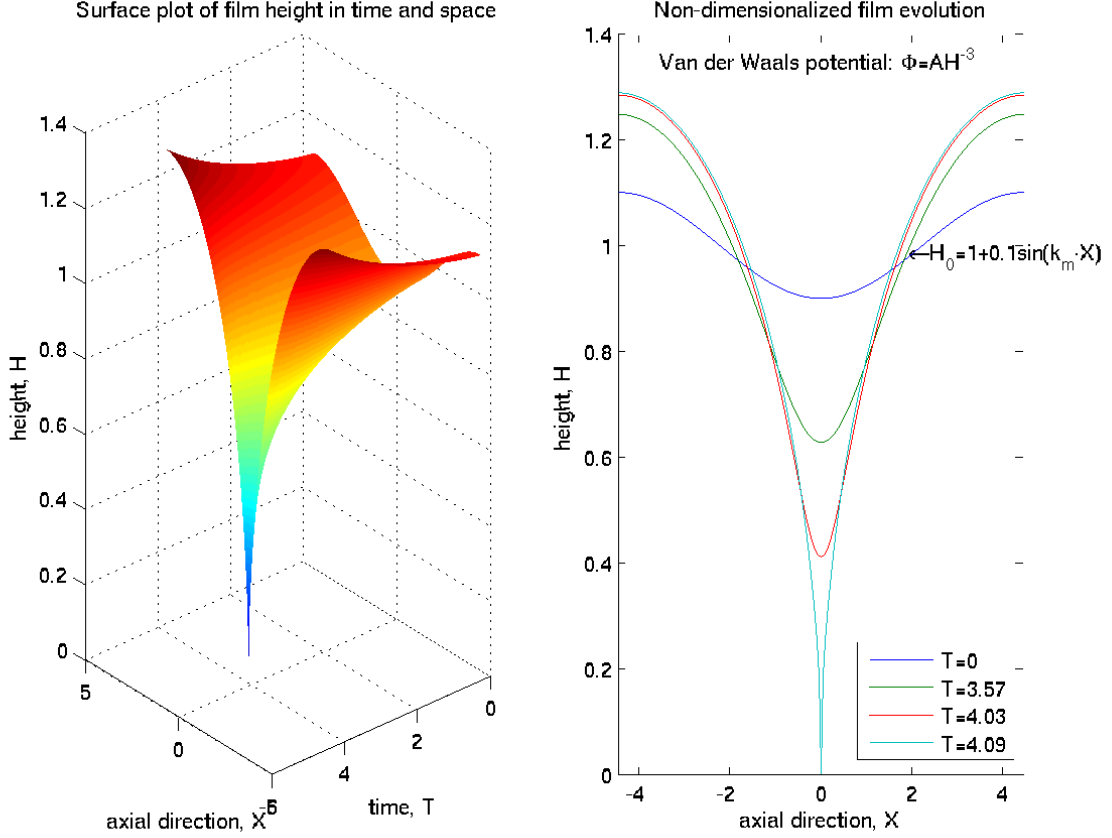


Figure 5.2: Solution of the non-dimensional scaled film equation eq.(5.4) with Van der Waals potential $\Phi = AH^{-3}$.

structures, $\partial_T H \simeq \partial_X(CH^3\partial_X^3 H) \simeq 0$ so that the attractive and repulsive intermolecular forces are dominating.

$$\begin{aligned} \Rightarrow A_3 H_{min}^{-3} - A_9 H_{min}^{-9} &= 0 \\ \Leftrightarrow H_{min} &= \left(\frac{A_3}{A_9}\right)^{-\frac{1}{6}} \end{aligned} \quad (5.6)$$

The deviation can be due to the simplifications in the analysis above, although the deviation seem to not vary significantly.

5.3 Evaluation of computational platform for the dimensional thin film equation with intermolecular forces

The use of the developed microscopic model is to gain physical insight from the molecular forces on the dimensional thin film. We can then also quantify typical time and

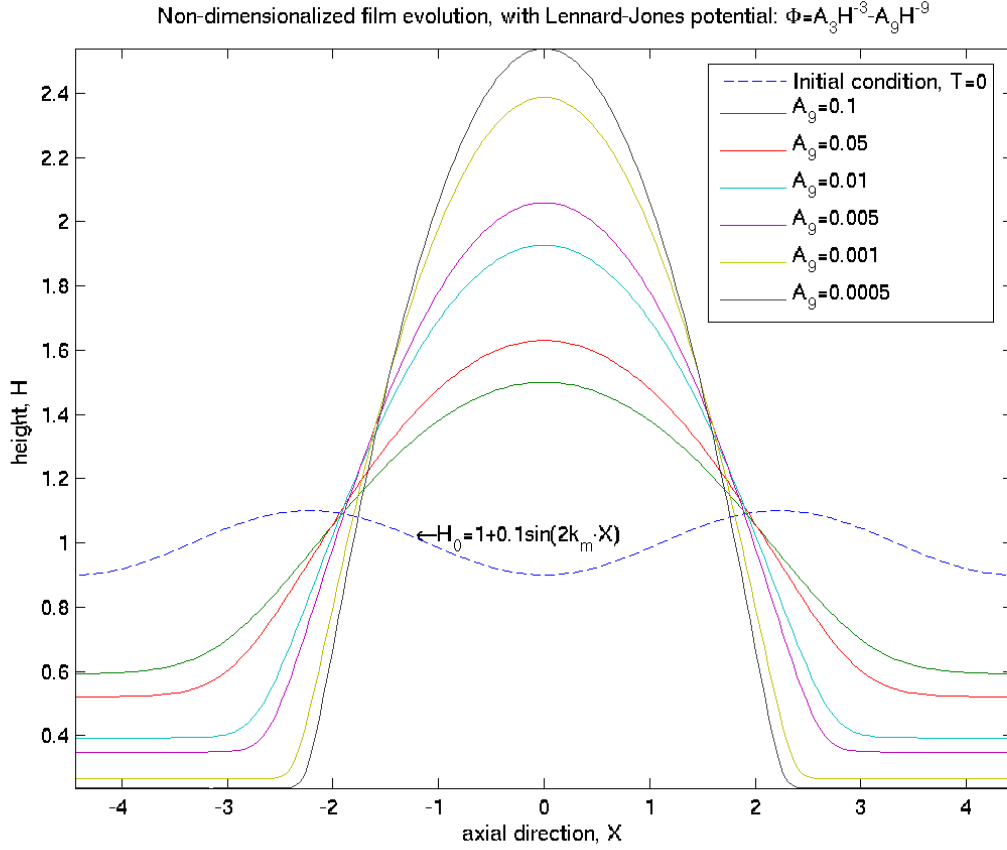


Figure 5.3: Solution of the non-dimensional scaled film equation eq.(5.4) with Lennard-Jones potential $\Phi = A_3 H^{-3} - A_9 H^{-9}$.

A_3	A_9	H_{min} model	H_{min} analytical	% deviation
1	0.1	0.593	0.681	12.9%
1	0.05	0.521	0.607	14.1%
1	0.01	0.393	0.464	15.3%
1	0.005	0.349	0.414	15.7%
1	0.001	0.265	0.316	16.1%
1	0.0005	0.236	0.282	16.3%

Table 5.1: Analytical and computed minimum film height with LJ-potential, $\Phi = A_3 H^{-3} - A_9 H^{-9}$.

length scales from the computations that will be exploited in a multiscale coupling with a macroscopic CMFD code. For this reasons some cases with physical properties have been investigated with the computational thin film platform. It was also of importance to demonstrate the fidelity with physical properties. Also for the purpose to validate the derivation of the non-dimensional equation.

Some of the reported applied physical quantities in the open literature for the study of thin liquid films are listed in Table 5.3.

Author	A' [J]	μ [$\frac{kg}{ms}$]	ν [$\frac{m^2}{s}$]	σ [$\frac{N}{m}$]	ρ [$\frac{kg}{m^3}$]	Film media
Bruelbach et al. [9]	10^{-20}	$2.88 \cdot 10^{-4}$	$3 * 10^{-7}$	0.059	960	Water
Bruelbach et al [9]	10^{-20}	$2.88 \cdot 10^{-4}$	$5 * 10^{-7}$	0.020	790	Ethanol
Mitlin et al.[27]	-10^{-20}	10^{-4}	10^{-7}	0.020	1000	Water like
Blossey et al. [4]	$2.2(4) \cdot 10^{-20}$	1200	-	0.0308	-	Polystyrene (PS)

Table 5.2: Properties for media used for film study.

Parameters from Burelbach et al. [9] (water like fluid) have been applied, and as for the case of the non-dimensional equation film rupture was experienced. The effective length of the long range Van der Waals forces have been examined by consequently changing the Hamaker constant A' .

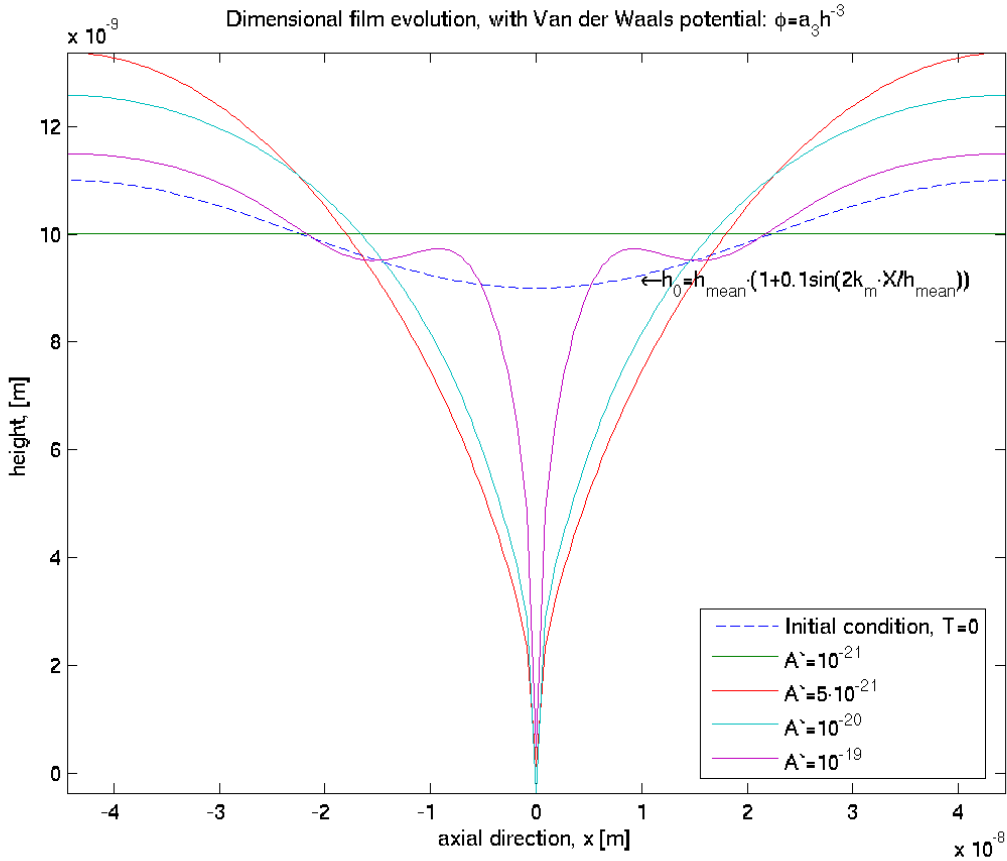


Figure 5.4: Solution of the dimensional film equation eq.(3.25) with Van der Waals potential $\phi = \frac{A'}{6\pi} h^{-3}$, with different Hamaker constants A' and $h_{mean} = 10nm$.

The results show the effective attractive forces, and as the Hamaker constant increases

the strong acceleration of the interface results in a steep rupture. As the Hamaker constant is decreased the surface tension force starts stabilize the film. This is seen for $A' = 10^{-21}$ when the surface tension force flattens the film, and it transforms into a planar state.

Parameters from Blossey et al. [4] have also been investigated and a remarkable dewetting scenario was captured. This morphology resemble hole formation in the dewetting, and similarity can be drawn to the results obtained in [4]. The intermolecular forces have been included in a model, for the potential with both an attractive and repulsive part, that was proposed by Oron et. al. [30].

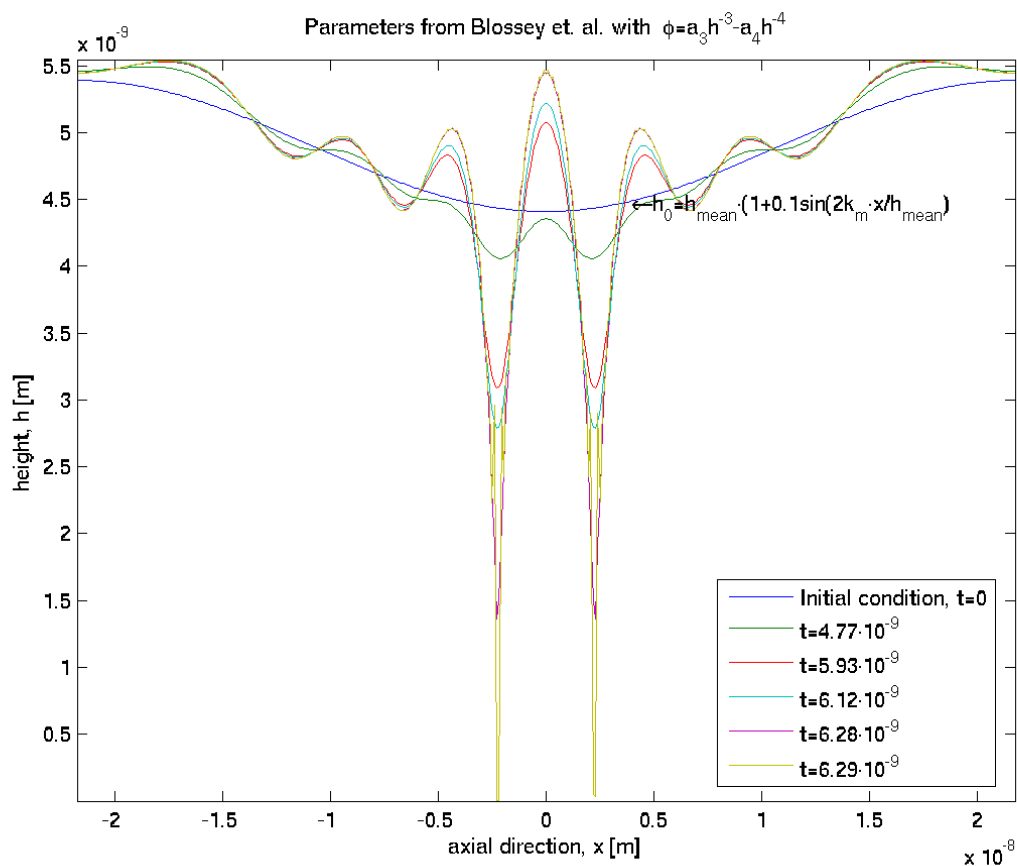


Figure 5.5: Solution of the dimensional film equation eq.(??), $\phi = a_3 h^{-3} - a_4 h^{-4}$, $h_{mean} = 4.9nm$.

5.4 Findings

The advanced microscopic model shows that the interfacial dynamics of thin films can not be solely explained by hydro dynamics, but new governing intermolecular forces starts to influence the film as its film height decreases. Some of the results that have previously been reported in literature are reproduced to validate the code. The obtained results shows that the final thin film topology are strongly influenced by: material properties (Hamaker constant), initial disturbance and mean film height, attractive and repulsive forces.

By critically inspecting the LWT we became aware of some shortcomings that should be noted. It is developed from a simplification of the Navier Stokes equations with its boundary conditions, with inclusion of source terms from molecular dynamics. Inclusion of source terms from molecular dynamics in hydrodynamics is questionable, since their theoretical basis is well separated. To fully capture all the intermolecular effects the usage of Hamaker constant and surface tension coefficient generate a plausible error, both these constants are actually never truly constant. Additional equations or simulations at every time step for the calculations of the Hamaker constant and surface tension coefficient would increase its accuracy. This would imply the development of new models or use of molecular dynamics simulations.

As film rupture takes place special treatment is needed as the film height approaches zero, $h \rightarrow 0$. The code is limited to discrete grid spacing and the physics down to the level of molecular distances are not captured. To capture these physics an additional model is needed to increase its fidelity.

The treatment of the surface is not in accordance with its molecular physics. The model treats the surface as heterogeneous which never truly the case. Even a nano-scopically treated surface will inherit "hills" and "valleys". These impurities are of nanometric-scale and will influence the film topology.

Although LWT posses some short-comings, it has proven capable to perform high fidelity simulations for thin film dynamics. Simulation results obtained Figure 5.3 and in [4] coincide with experimental results [4]. This also proves that the theory is ripe and makes it a prosperous avenue as a SGS thin film model, applicable for a multiscale coupling.

Chapter 6

Development of a novel technology and multiscale platform for coupling of a Sub-Grid Scale thin film model to a CMFD code

The investigation of the existing computational technology clearly shows that special treatment is needed for the case of thin film slug flow. As the film decreases to length scales that are less than the grid spacing $h < \Delta x$ a numerical dry out occurs. A computational platform for a Sub-Grid Scale (SGS) model for the thin film dynamics is already developed. A novel technique for the treatment of the multiscale phenomena with a SGS thin film model coupled with a CMFD code is described and multiscale simulations from thin film slug flow are presented.

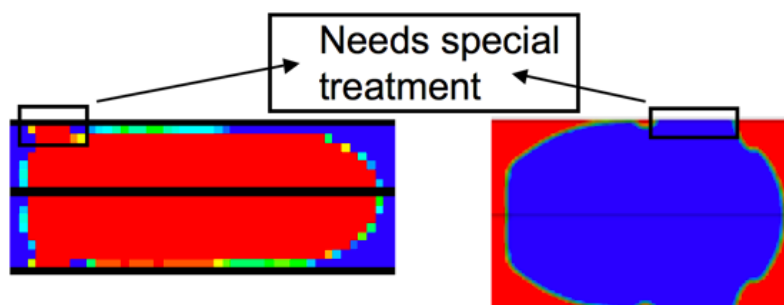


Figure 6.1: Results from FLUENT and TransAT shows numerical dry-out.

6.1 Hierarchy of descriptions for thin film Sub-Grid Scale model coupled to a macro solver

The author could not report any findings in literature of previous attempts of a SGS model for thin film slug flow. This is a new avenue that is pursued, that puts it at the frontier of science. A schematic Figure 6.2 of the level of description or accuracy of the microscopic length scales in the film that are captured with different film models coupled with a CMFD are shown.

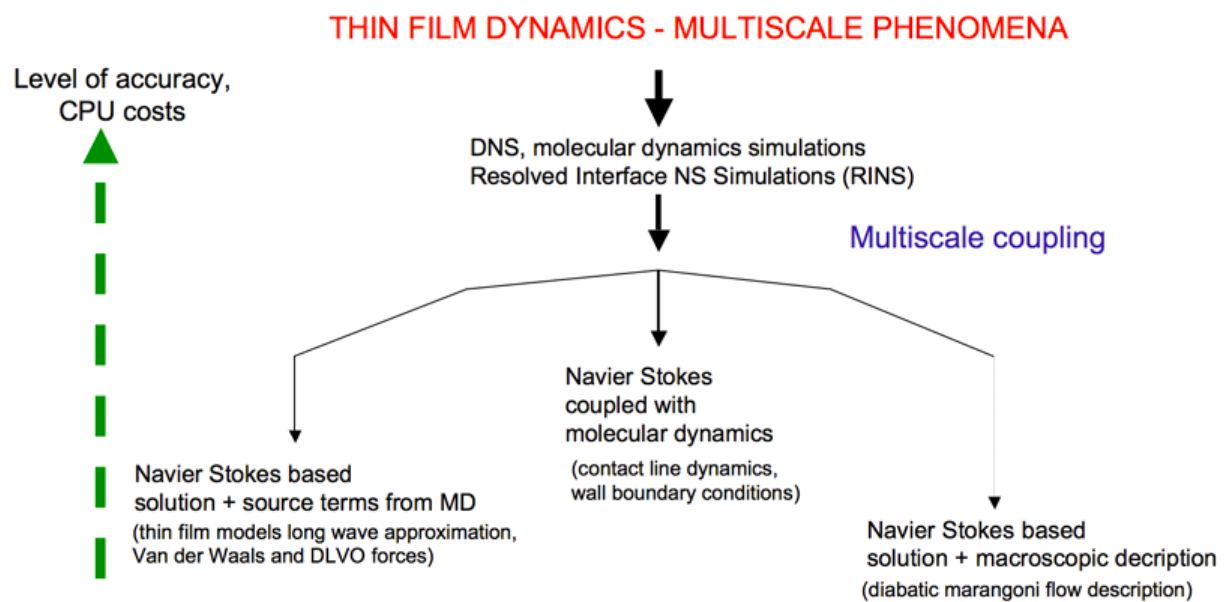


Figure 6.2: Hierarchy of micro thin film descriptions coupled to a macroscopic solver.

Different plausible models for the microscopic thin film have been proposed and examined by the author:

1. Model for free energy, local change of surface tension coefficient
 - *Coarse model.*
 - *Possibility to use already implemented CSF model in both VOF and Level Set.*
 - *Model dependent on local solid, liquid and gas material properties → capture different forces.*
2. Additional source terms in NS equations as an integral length scale model for filtered intermolecular and surface forces.
 - *Need to generate a model for length scales below a cut-off length.*
 - *The model plays an important role in parts of the computational domain.*

- *Model dependent on local solid, liquid and gas material properties→capture different forces.*

3. **Extracting and introducing advanced boundary conditions for local film height by coupling microscopic model and CMFD Level Set platform.**

- *Extracting the important microscopic variable (local film height) from additional advanced thin film SGS model.*

- *Coupling the microscopic model with the macroscopic computational platform through a novel multiscale methodology.*

- *Exploiting the Level Set distance function to impose the local film height.*

- *Model dependent on local solid, liquid and gas material properties→capture different forces.*

From these different branches the third (3.) proposed modelling approach was seen to be the most prosperous in terms of generating accurate results for thin film slug flow. Therefore the next section is devoted to further specification and explanation of the methodology behind the multiscale coupling of a SGS model with a CMFD code.

6.2 **Methodology and algorithm for a Sub-Grid Scale model coupled to a CMFD platform**

An advanced micro-scale computational platform has been developed for the dynamics of the thin liquid film. This model derived from Long Wave theory, has been validated against other published results. In the spirit of multiscale technology the goal is to couple the micro-scale model with a macro-scale CMFD platform. This means extracting quantities on the sub-grid level and "prolong" them on to the macro solver. Since it has been proved that the FLUENT with VOF code is unusable for such simulations the TransAT code with Level Set has been chosen as an appropriate macroscopic solver. The process of developing such an innovative computational platform was divided into three subsequent steps:

1. **Global minimum film height.**

A necessary first step is to show that the Level Set distance function can be used for such advanced boundary conditions. A numerical algorithm will control the preset minimum film height by imposing a distance from the wall by using the Level Set function.

$$\nabla\phi = \phi_{wall}(h) = constant. \tag{6.1}$$

This implies that when the film height in the domain becomes less than the minimum film height the minimum film height will be imposed. This solves the problem with

numerical dry out at the wall, and generates a physical solution with a lubricating thin film.

2. Correlation based film height with internal iteration loop for correct calculation of the interfacial shear stress.

In the calculations a bubble velocity is assumed from the first break up and bubble generation by using the correlations

$$U_B = \frac{L_{bubble}}{\frac{1}{f}}. \quad (6.2)$$

L_{bubble} is bubble length and f is the frequency of bubble generation. This is set as a reference bubble velocity in the calculations and the minimum film height is based on the correlation eq.(2.3). An iterative procedure is proposed for the calculation of the correct interfacial shear stress.

Iterative procedure for correct interfacial shear:

Parameters:

V_{TF} = velocity from thin film model on the interface.

U_{AD} = velocity in second adjacent wall normal cell.

$\tau_{TF,g/l}$ = interface shear stress thin film model, gas/liquid.

$\mu_{l/g}$ = viscosity liquid/gas.

δ = film height.

h_{AD} = height from wall to the node in second adjacent wall normal cell.

Continuum stress constraint: $\tau_{TF,g} = \mu_g \frac{\partial U_g}{\partial y} = \mu_l \frac{\partial U_l}{\partial y} = \tau_{TF,l}$.

Schematich drawing of thin film shear stress model

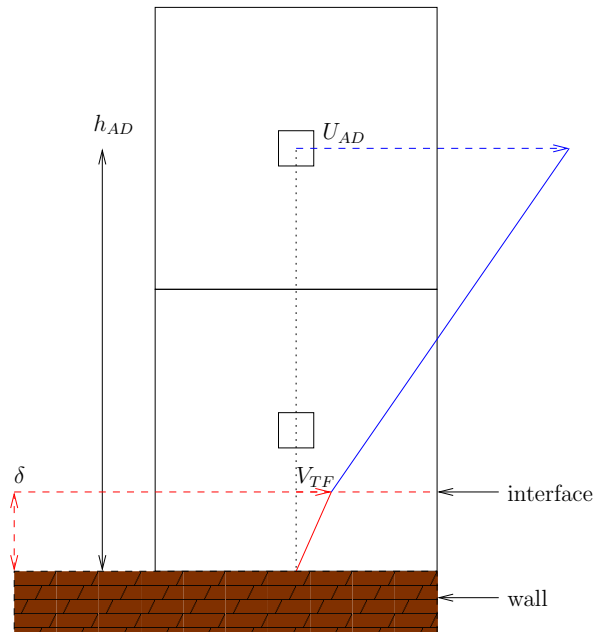


Figure 6.3: Schematic drawing of near wall cell and adjacent wall normal cell containing the interface.

- (a) Calculate bubble velocity from eq.(6.2) U_B .
- (b) Calculate film height from correlation $\delta \Rightarrow f(Ca(U_B))$, eq.(2.3)
- (c) The interface is filling the near wall cell.
- (d) Presume that we have a correct interface velocity, in the near wall cell at previous time-step (n-1) $V_{TF}^n = V_{TF}^{n-1}$, initial guess.
- (e) Calculate the new shear stress from the gas on the interface.

$$\tau_{TF,g} = \mu_g \frac{U_{AD}^n - V_{TF}^n}{h_{AD} - \delta} = \text{interface shear stress gas.} \quad (6.3)$$

- (f) Check if the stress obtained satisfy the continuum mechanics, $\tau_{TF,g} = \tau_{TF,l}$, if this is **TRUE** go out of the iteration loop.

$$\tau_{TF,l} = \mu_l \frac{V_{TF}^n}{\delta} = \text{interface shear stress liquid.} \quad (6.4)$$

- (g) **IF** $\tau_{TF,g} \neq \tau_{TF,l}$ find new velocity at interface $\Rightarrow V_{TF}^n = \frac{\tau_{TF,g} \delta}{\mu_l}$
- (h) Go to (c) to and run the iteration procedure until $\tau_{TF,g} = \tau_{TF,l}$.

Validation by comparing against published experimental results will ensure the correct calculation of shear interfacial stress to ensure correct bubble velocity. The procedure will need testing for the diabatic case and again validated against experimental results

3. Coupling of advanced micro-scale film model with macro-scopic CMFD model TransAT.

Step 1 and 2 have developed a solid platform for further an advanced multiscale coupling.

As the interface is filling the wall adjacent cell the local film height cannot be extracted from the CMFD simulation itself. To increase fidelity we can locally determine the film height from the equation from LWT eq.(5.1). Basically, the macro-scale model can be applied all over the computational domain once appropriate boundary conditions are selected. In a broad sense, the boundary conditions for the CMFD are the missing macro-scale *property* that has to be recovered with the micro-scale simulation. This class of problems (Type-B problems, according to the HMM classification due to Engquist et. al. [15]) is actually one of the most frequently encountered in the context of the HMM. This approach is especially convenient since the film properties depends on fluid conditions local in time and space, which means that the spatial domain for the solution of the micro-scale SGS model

can be limited to small areas around the dry-out. The information about the local film height is calculated by the computational SGS thin film platform on a locally refined sub-grid. An initial long wave disturbance is enforced in the initial micro solution extracted from CMFD. The mean cell film height is imposed by the Level Set ϕ function as a non-homogeneous wall boundary condition.

$$\nabla\phi = \phi_{wall}(h) \neq 0. \quad (6.5)$$

If several neighbouring wall adjacent cells need SGS treatment a smoothing function between them is proposed to ensure a smooth interface. As the last step the iteration procedure, described above, used to ensure that we obtain the correct interfacial shear stress.

A multiscale methodology is needed for the coupling between the macro CMFD and micro SGS model. Two features make the SGS model suitable for a multiscale coupling; in the first place, the SGS model is continuum based so that we can promote a stronger coupling between the model that would be feasible for molecular dynamics simulations; in the second place, scale separation is exploited and the much faster dynamics if the SGS thin film model relaxes to a steady-state solution within one macro CMFD time step $\delta t_{TransAT} \gg \delta t_{SGS-model}$. It simplifies the coupling as only the steady-state solution is needed from the SGS thin film model.

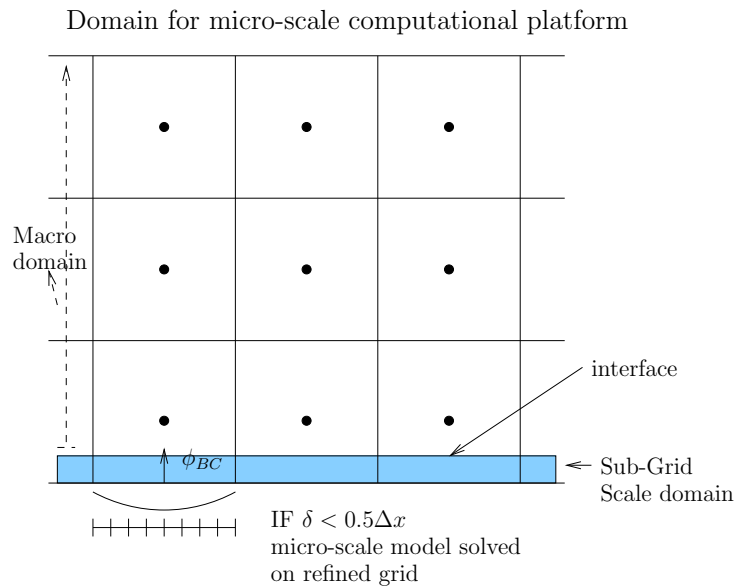
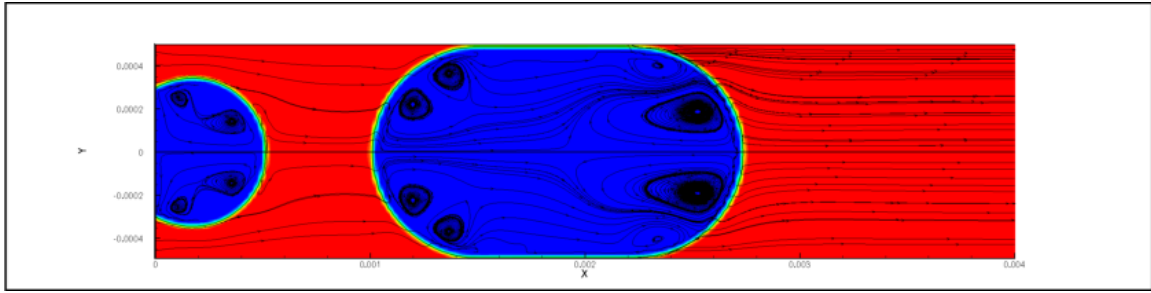


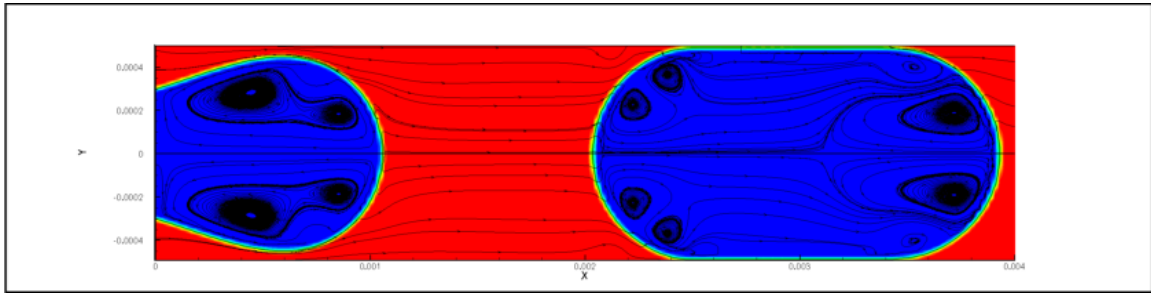
Figure 6.4: Domain for the microscopic thin film model for imposing boundary condition on the macro solver.

6.3 Multiscale simulations with a Sub-Grid Scale thin film model

A multiscale platform has been developed (step 1) to perform multiscale simulations for thin film slug flow, in collaboration with ASCOMP. An advanced boundary condition is used to impose the minimum film height at the pipe wall. This ensures that we will not have a numerical dry-out. High fidelity results are shown for two different minimum film heights. The first simulation shows results with a film height that is half of the cell width $h_{min} = 0.1\mu m$, the second simulation shows results with a film height that is one fourth of the cell width $h_{min} = 0.05\mu m$. Comparing the macro-scopic TransAT simulation Figure 4.25 with the first-of-a-kind multiscale simulation Figure 6.5, 6.7 one can conclude that the multiscale simulation produces a much more physical reality. The bubble topology as well as bubble speed correlates well with macro-scopic simulations. It illustrates that multiscale treatment generates results that with regular Level Set CMFD would be unattainable without a special treatment for the lubricating film.

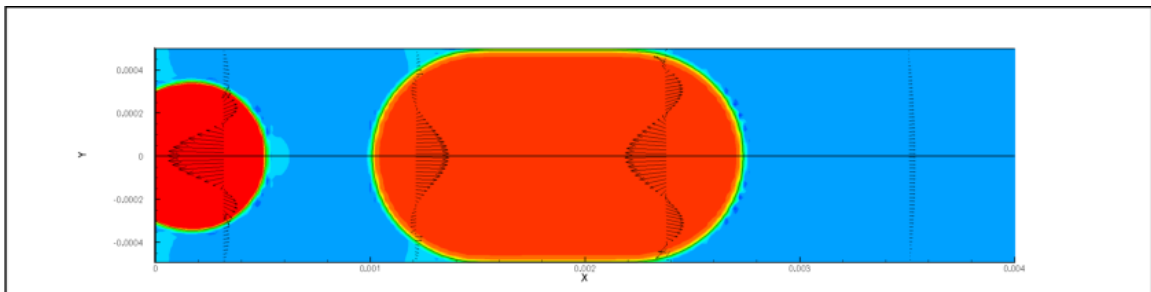


(a) $T = 0.301 \cdot 10^{-1} s.$

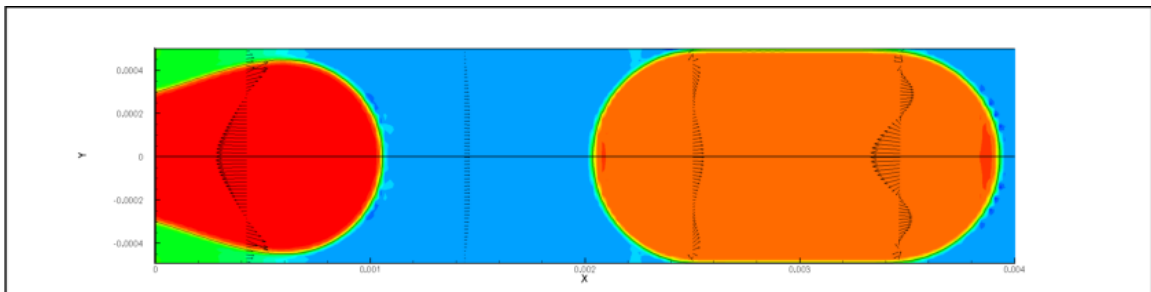


(b) $T = 0.408 \cdot 10^{-1} s.$

Figure 6.5: Multiscale simulation with $h_{min} = 0.1 \mu m$ contours of the densities with streamlines and isolate for $\phi = 0$, Case 5.

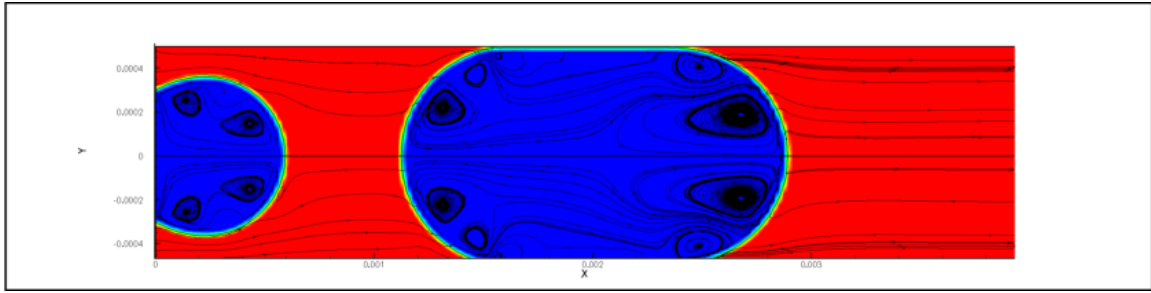


(a) $T = 0.301 \cdot 10^{-1} s.$

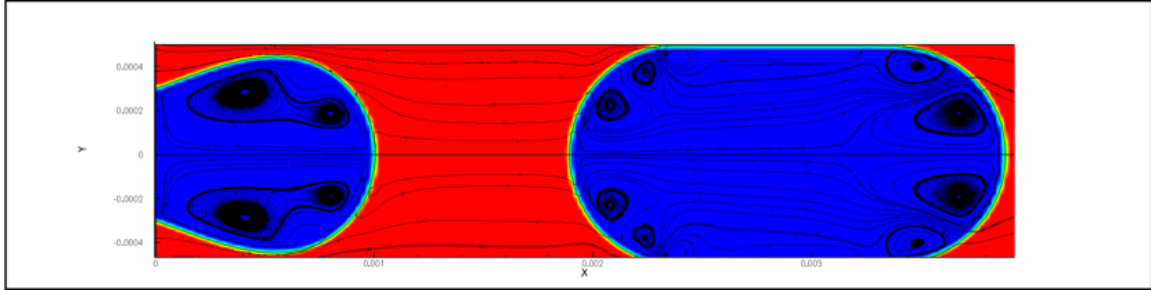


(b) $T = 0.408 \cdot 10^{-1} s.$

Figure 6.6: Multiscale simulation with $h_{min} = 0.1 \mu m$ contours of the densities with streamlines and isolate for $\phi = 0$, Case 5.

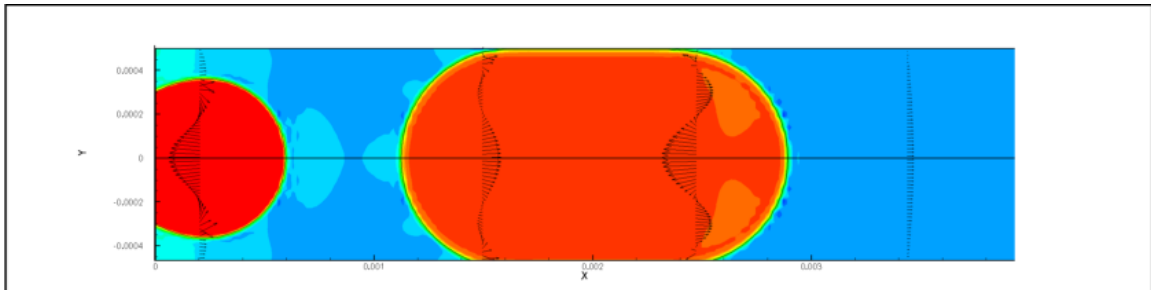


(a) $T = 0.314 \cdot 10^{-1} s.$

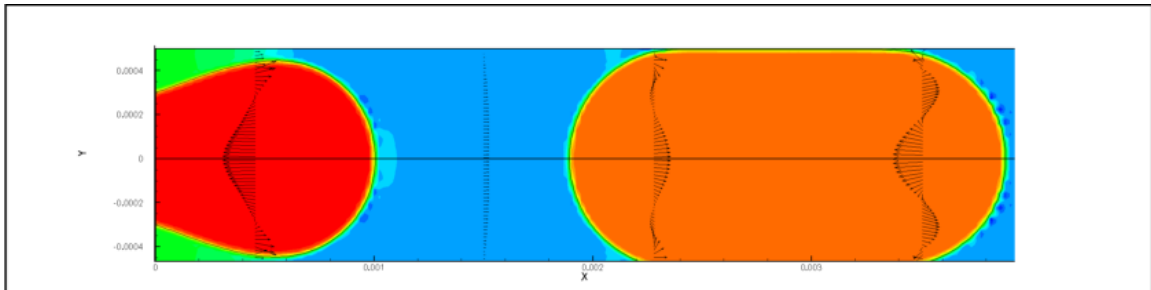


(b) $T = 0.400 \cdot 10^{-1} s.$

Figure 6.7: Multiscale simulation with $h_{min} = 0.05 \mu m$ contours of the densities with streamlines and isoline for $\phi = 0$, Case 5.



(a) $T = 0.314 \cdot 10^{-1} s.$



(b) $T = 0.400 \cdot 10^{-1} s.$

Figure 6.8: Multiscale simulation with $h_{min} = 0.05 \mu m$ contours of the densities with streamlines and isoline for $\phi = 0$, Case 5.

6.3.1 Summary

The standard CMFD treatment of this problem imposes a wall boundary condition on the Level Set function ϕ :

$$\nabla\phi = 0. \tag{6.6}$$

As we previously observed, the knowledge of the level set function ϕ lets us determine if we have gas or liquid in a computational cell, and, therefore, the film thickness in the whole domain. We notice that a problem arises when the presence of gas is detected in a wall adjacent cell; from the point of view of the CMFD solution this means that there is no liquid wetting the wall. However, with the quantities (quartz, water, air), intermolecular theory guarantees that the wall is wetted all the time. The result obtained from the CMFD solution is rather a *numerical* dry out, meaning that the film thickness is actually located somewhere inside the wall adjacent cell and, as a consequence, all information about the film is lost from a CMFD perspective. In order to have a physically sound solution, then, we have to ensure that the CMFD calculation *always* predicts the presence of liquid in the wall adjacent cell. This could actually be done, if the liquid film thickness h was known, by imposing a non-homogeneous boundary condition on the level set function:

$$\nabla\phi = \phi_{wall}(h) \neq 0. \tag{6.7}$$

Again, we remark that this information, namely the value of h , cannot be extracted by the CMFD simulation itself. The multiscale coupling between the CMFD model and some form of sub-grid scale model provides a solution to this problem for the calculation of the film thickness. In our case the sub-grid model is provided by the thin film equation eq.(5.1). This approach is particularly convenient for two reasons: in the first place, the film thickness in a cell depends on the fluid conditions locally in time and space, which means that the spatial domain for the solution of the thin film equation can be limited to a small area around the cell where numerical dry out is detected; in the second place, we can exploit the scale separation between the thin film dynamics and the much slower dynamics of the Navier Stokes equations: in this case, in fact, we can simply use the steady state formulation because the time dependent solution of the thin film equation will, in any case, relax to the steady state one on a time scale much smaller than a CMFD time step.

From a scientific point of view multiscale treatment is of great interest and importance, not only for this problem. For many phenomena what is happening on the small scales can influence the larger scales. In reality all physical phenomena are of multiscale nature. The difficulty and important aspect is to be able to separate the phenomena where advanced multiscale treatment is needed.

The treatment of thin liquid films in slug flow does not only have a great impact in science but also in engineering applications. Such special treatment makes it feasible to reduce mesh size and then reduce CPU time, without losing important film features and dry out. This implicates that shear, heat and mass transfer can be more correctly calculated. A new avenue for interface tracking methods does also open, where this new technology opens new avenues that currently is not possible with the existing technology. For such advanced film treatment the geometrical case limitations for the interface tracking methods can be removed. As a consequence pipe junction flow (Y-junctions and T-junction), can be simulated with high accuracy. In the junction a thin film is formed that prevents bubble break-up, that can be calculated in high fidelity simulations with a SGS thin film treatment. A bubble traveling in a micro channel with a junction is clearly visualized in the experiment performed by Fowlkes et. al. [10]. Present CMFD technology without multiscale treatment will fail to deliver accurate and physical sound results. The bubble will separate producing an unphysical solution (a numerical dry-out) as the bubble enters in the junction. Multiscale simulation of thin film slug flow shows high fidelity first-of-a-

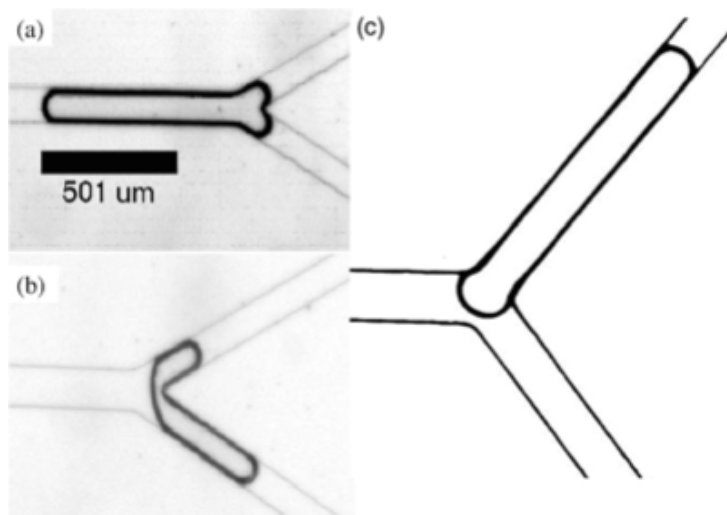


Figure 6.9: (a) Lodging state, (b) Lodging state, (c) Bubble lodged in on of the branches from [10].

kind simulations. The already developed model and platform has at current status (step 1), already an impact in micro-fluidic applications.

Chapter 7

Conclusion and future work

Evaluation of the CMFD codes FLUENT and TransAT shows that the multiscale nature of slug flow in a micro channel presents a formidable challenge to numerical simulations. Although full-scale microscopic simulations can still be attempted, such simulations are not practical. Multiscale treatment is needed to obtain high fidelity simulations without a dramatic sacrifice of computational time.

VOF (FLUENT) and Level Set (TransAT) are the two most widely applied interface tracking methods and they represent the state-of-the-art in CMFD. To assess performance of the two methods, two CMFD codes have been applied, FLUENT (VOF) and TransAT (Level Set). By comparing their performance we numerically validated the codes and examined numerical errors and artifacts. It became evident that FLUENT was incapable to generate physically sound results for macroscopic slug flow. A diffuse interface treatment and the averaging of material properties within their mixed cells lead to unphysical results. Arithmetically averaging based on volume fraction generates a substantial numerical error in simulations with high density and viscosity ratio. The outcome is that viscous shear stress transfer across interface is deficient. This effect suppresses "natural" interfacial instabilities and slug flow generation. The AMR FLUENT simulations suggest that spurious currents govern the generation of slug flow on a "coarse" mesh. The AMR FLUENT simulations with a disturbed liquid inlet were performed to demonstrate the effect of an imposed artificial instability on slug flow generation. The present study concludes that the VOF-based scheme in FLUENT is not appropriate for the numerical solution of shear-driven multiphase flow problems, with high density and viscosity ratios and dominant flow direction parallel to the interface. Consequently, the Level Set-based TransAT code is employed as the computational platform for implementing and testing a proposed scheme for multiscale treatment.

In spite of the fact that TransAT produces physically sound results for macroscopic slug flow, is unable to capture the micro-scale physics for thin film slug flow. Remarkably, the CMFD simulations (from both codes) generate a numerical "dry-out". This signifies a behavior that micro-scale perturbances can effectively propagate up scale, rendering the macro-scale description (CMFD) inadequate. A novel technology for multiscale coupling between a CMFD code and a Sub-Grid Scale (SGS) model is proposed, to preserve micro-scale perturbations. It enables high fidelity simulations without a dramatic increase in computational time.

First step, in the novel technology, was the development of a computational platform for a SGS thin film model. Numerical simulations for thin film based on the Long Wave Theory (LWT) agreed with experimental results in [4], suggesting that the theory is ripe as a proper SGS model. This fact is recognized and exploited. A computational platform has been developed and validated against previously published results. The results made it feasible to quantify effects from intermolecular forces and illustrated that the SGS model captures the dual nature of thin films, from hydro- and molecular- dynamics.

Second step, in the novel technology, was the development of a multiscale platform for coupling a SGS thin film model to a CMFD code (TransAT). Subsequent steps are proposed for the treatment of an advanced non-homogenous wall boundary condition, using the Level Set distance function to characterize the local film height. First-of-a-kind multiscale simulations for thin film slug flow, with a fixed minimum lubricating film height, shows physical results. The present development creates a new avenue for applying numerical simulations in micro-fluidic applications. It also demonstrated that the platform for multiscale treatment with the Level Set function is preceptive.

Although the simulations show the fidelity of the multiscale coupling methodology with a SGS thin film model, additional aspects needs further development and model refinement in the future. The SGS thin film model needs improved or additional models for the prediction of: Hamaker constant, surface tension coefficient and polar forces. For the treatment of film rupture additional model refinement is needed to capture the molecular physics.

In the CMFD framework additional physics is needed for the bubble pinch-off in slug generation. As the interfaces approach each other a thin film is formed and intermolecular forces become dominant. This is another avenue of multiscale treatment for thin film physics.

A multiscale coupling between the full-bloom SGS thin film model and TransAT is needed. This work is in progress in collaboration with ASCOMP. A model developed and validated will have a significant impact in many multiphase mechanistic flow problems, such as: porous media, boiling. A case of high practical and fundamental interest is microfluidic system and evaporating thin film in high heat flux boiling and burnout. For such a case additional treatment is also needed for the triple-point contact line.

Acknowledgments

I would like to thank the people who have helped me and made this work possible. First I thank my professor, Truc-Nam Dinh, for all his support, suggestions and time throughout this work, it has been invaluable for me. I would like to thank the rest of the people at the Division of Nuclear Power Safety at KTH, specially Francesco Cadinu and Dr. Pavel Kudinov for their time and fruitful discussions. I would like to thank the people at ASCOMP GmbH, Dr. Djamel Lakehal and Dr. Chidambaram Narayanan, for their collaboration and thrust in our ideas. Finally I would like to thank, my Solvor, for putting up with my long nights of work and difficulty clearing my mind of work.

Bibliography

- [1] M. K. Akbar and S. M. Ghiaasiaan. Simulation of taylor flow in capillaries based on the volume-of-fluid technique. *INDUSTRIAL AND ENGINEERING CHEMISTRY RESEARCH*, 45(15):5396–5403, Jul 2006.
- [2] M. K. Akbar, D. A. Plummer, and S. M. Ghiaasiaan. On gas-liquid two-phase flow regimes in microchannels. *INTERNATIONAL JOURNAL OF MULTIPHASE FLOW*, 29(5):855–865, May 2003.
- [3] P. Aussillous and D. Quere. Quick deposition of a fluid on the wall of a tube. *PHYSICS OF FLUIDS*, 12(10):2367–2371, Oct 2000.
- [4] J. Becker, G. Grun, R. Seemann, H. Mantz, K. Jacobs, K. R. Mecke, and R. Blossey. Complex dewetting scenarios captured by thin-film models. *NATURE MATERIALS*, 2(1):59–63, Jan 2003.
- [5] J. Bico and D. Quere. Liquid trains in a tube. *EUROPHYSICS LETTERS*, 51(5):546–550, Sep 2000.
- [6] T. Boeck, J. Li, E. Lopez-Pages, P. Yecko, and S. Zaleski. Ligament formation in sheared liquid-gas layers. *THEORETICAL AND COMPUTATIONAL FLUID DYNAMICS*, 21(1):59–76, Jan 2007.
- [7] J. U. Brackbill, D. B. Kothe, and C. Zemach. A continuum method for modeling surface-tension. *JOURNAL OF COMPUTATIONAL PHYSICS*, 100(2):335–354, Jun 1992.
- [8] F. P. Bretherton. The motion of long bubbles in tubes. *JOURNAL OF FLUID MECHANICS DIGITAL ARCHIVE*, 10(02):166–188, 2006.
- [9] J. P. Burelbach, S. G. Bankoff, and S. H. Davis. Nonlinear stability of evaporating condensing liquid-films. *JOURNAL OF FLUID MECHANICS*, 195:463–494, Oct 1988.

- [10] A. J. Calderon, Y. S. Heo, D. Huh, N. Futai, S. Takayama, J. B. Fowlkes, and J. L. Bull. Microfluidic model of bubble lodging in microvessel bifurcations. *APPLIED PHYSICS LETTERS*, 89(24):244103, Dec 2006.
- [11] N. H. Chen, T. Kuhl, R. Tadmor, Q. Lin, and J. Israelachvili. Large deformations during the coalescence of fluid interfaces. *PHYSICAL REVIEW LETTERS*, 92(2):024501, Jan 2004.
- [12] W. L. Chen, M. C. Twu, and C. Pan. Gas-liquid two-phase flow in micro-channels. *INTERNATIONAL JOURNAL OF MULTIPHASE FLOW*, 28(7):1235–1247, Jul 2002.
- [13] R. J. Deissler and A. Oron. Stable localized patterns in thin liquid-films. *PHYSICAL REVIEW LETTERS*, 68(19):2948–2951, May 1992.
- [14] Cyril Duez, Christophe Ybert, Christophe Clanet, and Lyderic Bocquet. Making a splash with water repellency. *NATURE PHYSICS*, 3(3):180–183, 2007.
- [15] W. E. B. Engquist, X. Li, W. Ren, and E. Vanden-Eijnden. Heterogeneous multi-scale methods: A review. *COMMUNICATION IN COMPUTATIONAL PHYSICS*, 2(3):367–450, Jun 2007.
- [16] Wei Shyy Eray Uzgoren, Jaeheon Sim. Computations of multiphase fluid flow using marker-based adaptive, multilevel cartesian grid method. *45th AIAA AEROSPACE SCIENCE MEETING AND EXHIBIT, RENO, NEVADA*, January 2007.
- [17] F. Fairbrother and A. E. Stubbs. Part vi the bubble-tube methods of measurement. *J. CHEM. SOC*, 1(527), 1935.
- [18] Peric M. Ferziger, J. H. *Computational Methods for Fluid Dynamics*. SPRINGER-VERLAG, 3rd edition, 2002.
- [19] M. Heil. Finite reynolds number effects in the bretherton problem. *PHYSICS OF FLUIDS*, 13(9):2517–2521, Sep 2001.
- [20] C. W. Hirt and B. D. Nichols. Volume of fluid (vof) method for the dynamics of free boundaries. *JOURNAL OF COMPUTATIONAL PHYSICS*, 39(1):201–225, 1981.
- [21] C. C. Hwang, J. Y. Hsieh, K. H. Chang, and J. J. Liao. A study of rupture process of thin liquid films by a molecular dynamics simulation. *PHYSICA A*, 256(3-4):333–341, Aug 1998.
- [22] Jacob N. Israelachvili. *Intermolecular and surface forces*, volume 2. ed. Academic Press, San Diego, 1992.

- [23] R. K. Jain and E. Ruckstein. Stability of stagnant viscous films on a solid-surface. *JOURNAL OF COLLOID AND INTERFACE SCIENCE*, 54(1):108–116, 1976.
- [24] R. Khanna and A. Sharma. Pattern formation in spontaneous dewetting of thin apolar films. *JOURNAL OF COLLOID AND INTERFACE SCIENCE*, 195(1):42–50, Nov 1997.
- [25] M. T. Kreutzer, F. Kapteijn, J. A. Moulijn, and J. J. Heiszwolf. Multiphase monolith reactors: Chemical reaction engineering of segmented flow in microchannels. *CHEMICAL ENGINEERING SCIENCE*, 60(22):5895–5916, Nov 2005.
- [26] D. Lakehal, G. Larrignon, and C. Narayanan. Computational heat transfer and two-phase flow topology in miniature tubes. *MICROFLUID NANOFLUID*, 2007.
- [27] V. S. Mitlin and N. V. Petviashvili. Nonlinear dynamics of dewetting - kinetically stable structures. *PHYSICS LETTERS A*, 192(5-6):323–326, Sep 1994.
- [28] R. R. Nourgaliev, T. G. Theofanous, and S. Wiri. Short communications: “direct numerical simulations of two-layer viscosity-stratified flow, by qing cao, kausik sarkar, ajay k. prasad, ijmf (2004) 30, 1485-1508”. *INTERNATIONAL JOURNAL OF MULTIPHASE FLOW*, 2006.
- [29] A. Oron. Three-dimensional nonlinear dynamics of thin liquid films. *PHYSICAL REVIEW LETTERS*, 85(10):2108–2111, Sep 2000.
- [30] A. Oron, S. H. Davis, and S. G. Bankoff. Long-scale evolution of thin liquid films. *REVIEWS OF MODERN PHYSICS*, 69(3):931–980, Jul 1997.
- [31] S. Osher and J. A. Sethian. Fronts propagating with curvature-dependent speed - algorithms based on hamilton-jacobi formulations. *JOURNAL OF COMPUTATIONAL PHYSICS*, 79(1):12–49, Nov 1988.
- [32] G. Reiter, A. Sharma, A. Casoli, M. O. David, R. Khanna, and P. Auroy. Thin film instability induced by long-range forces. *LANGMUIR*, 15(7):2551–2558, Mar 1999.
- [33] G. Reiter, A. Sharma, R. Khanna, A. Casoli, and M. O. David. The strength of long-range forces across thin liquid films. *JOURNAL OF COLLOID AND INTERFACE SCIENCE*, 214(1):126–128, Jun 1999.
- [34] W. Q. Ren and E. Weinan. Heterogeneous multiscale method for the modeling of complex fluids and micro-fluidics. *JOURNAL OF COMPUTATIONAL PHYSICS*, 204(1):1–26, Mar 2005.

- [35] F. Sarrazin, K. Loubiere, L. Prat, C. Gourdon, T. Bonometti, and J. Magnaudet. Experimental and numerical study of droplets hydrodynamics in microchannels. *AICHE JOURNAL*, 52(12):4061–4070, Dec 2006.
- [36] A. SHARMA. Relationship of thin-film stability and morphology to macroscopic parameters of wetting in the apolar and polar systems. *LANGMUIR*, 9(3):861–869, Mar 1993.
- [37] A. Sharma and A. T. Jameel. Nonlinear stability, rupture, and morphological phase-separation of thin fluid films on apolar and polar substrates. *JOURNAL OF COLLOID AND INTERFACE SCIENCE*, 161(1):190–208, Nov 1993.
- [38] A. Sharma and R. Khanna. Pattern formation in unstable thin liquid films under the influence of antagonistic short- and long-range forces. *JOURNAL OF CHEMICAL PHYSICS*, 110(10):4929–4936, Mar 1999.
- [39] A. Sharma and E. Ruckstein. An analytical nonlinear-theory of thin-film rupture and its application to wetting films. *JOURNAL OF COLLOID AND INTERFACE SCIENCE*, 113(2):456–479, Oct 1986.
- [40] Y. D. Shikhmurzaev. Macroscopic mechanism of rupture of free liquid films. *COMPTES RENDUS MECANIQUE*, 333(3):205–210, Mar 2005.
- [41] Short course: Computational Multi Fluid Dynamics Zürich 2007. *Computational Multifluid Dynamics (CMFD) Part 2B*, 2007.
- [42] B. Suman and S. Kumar. Dynamics of thin liquid films on surfaces with a time-periodic wettability. *JOURNAL OF COLLOID AND INTERFACE SCIENCE*, 304(1):208–213, Dec 2006.
- [43] T. Taha and Z. F. Cui. Cfd modelling of slug flow in vertical tubes. *CHEMICAL ENGINEERING SCIENCE*, 61(2):676–687, Jan 2006.
- [44] T. Taha and Z. F. Cui. Cfd modelling of slug flow inside square capillaries. *CHEMICAL ENGINEERING SCIENCE*, 61(2):665–675, Jan 2006.
- [45] G. I. Taylor. Deposition of a viscous fluid on the wall of a tube. *JOURNAL OF FLUID MECHANICS DIGITAL ARCHIVE*, 10(02):161–165, 2006.
- [46] W. Villanueva and G. Amberg. Some generic capillary-driven flows. *INTERNATIONAL JOURNAL OF MULTIPHASE FLOW*, 32(9):1072–1086, Sep 2006.
- [47] M. B. Williams and S. H. Davis. Non-linear theory of film rupture. *JOURNAL OF COLLOID AND INTERFACE SCIENCE*, 90(1):220–228, 1982.

- [48] S. M. Wise, J. S. Kim, and W. C. Johnson. Surface-directed spinodal decomposition in a stressed, two-dimensional, thin film. *THIN SOLID FILMS*, 473(1):151–163, Feb 2005.

Objectives for the Appendix

The objectives for the appendix are to show results to supplement stated hypothesis or additional supplementary results to the thesis. The appendix is separated into three different parts:

1. Benchmark case in FLUENT with a rising bubble.
2. Parametric study on slug flow in TransAT.
3. Additional results from LWT.

The first chapter in the appendix shows results from a benchmark case for numerical simulations of a rising bubble in a stagnant liquid, with FLUENT. The simulations shows recirculation patterns for high viscosity and density ratio simulations with an AMR method. This proves that the lack of recirculation and bubble break-up, previously shown for slug flow, are not numerical effects of AMR.

A parametric study with the use of TransAT shows changes in: recirculation pattern, capillary force and pressure drop. The results increase the physical insight of the macroscopic slug flow nature by parameter changes, which can be exploited for engineering applications.

Additional results from LWT shows the effective length of the Van der Waals forces.

Appendix A

Rising bubble (spherical cap) benchmark case

The author has earlier performed an in-house project, where the effects of resolution in both time and space have been examined. The motivation for this work was to validate the performance of the commercial CFD code FLUENT and to show effects of time and space resolution. A benchmark case for a rising bubble in a stagnant liquid, with spherical cap was chosen. For this case of a rising bubble there exist an analytical solution. The simulation results show a reasonable match and good performance of the code. The technical approach was to use a moving coordinate system, with the pre-calculated steady-state bubble velocity. This avoided time and space restrictions for the study of the rising bubble.

The Archimedes (Ar) number expresses the ratio between the gravitational velocity (hydrostatic head) and the viscous forces. Archimedes number,

$$Ar = \frac{\rho_l^{\frac{1}{2}}(\rho_l - \rho_g)^{\frac{1}{2}}g^{\frac{1}{2}}d_b^{\frac{3}{2}}}{\mu_l}. \quad (A.1)$$

The Bond (Bo) number is expressing the ratio between the gravitational force and the surface tension force. So low Bond number indicates that the surface tension forces are dominating. Bond number,

$$Bo = \frac{\rho_l g d_b^2}{\sigma}. \quad (A.2)$$

As the Morton (Mo) number is defining the ratio between the viscous length scale and the capillary length scale. Morton number,

$$Mo = \frac{g\mu_l^4}{\rho_l\sigma^4}. \quad (A.3)$$

A.1 shows the rising bubble evolution for three different mesh resolutions. These simulations were performed to quantify effects of lack of time and space resolution for

-	Ar	Bo	Mo	σ	ρ_l	μ_l	ρ_b	μ_b
Rising bubble	32.7	40	0.056	0.1	1000	0.273556	10	0.00273556

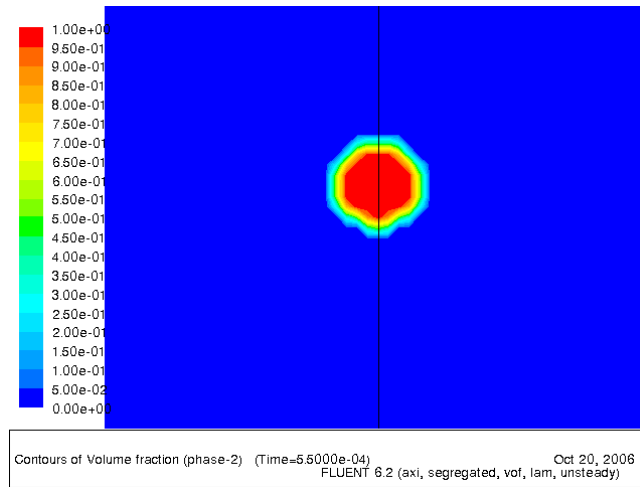
Table A.1: Material properties rising bubble.

VOF FLUENT simulations. As is clearly shown with a coarse mesh it becomes impossible to extract qualitative information from the simulations. The interface becomes so severely smeared that it can not reproduce properly the physical behavior.

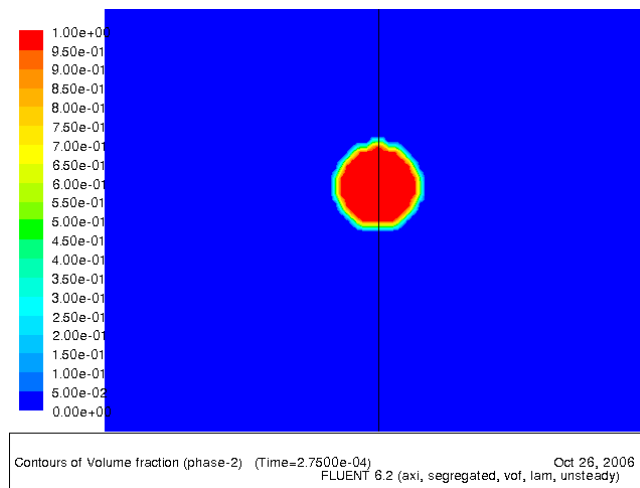
A.2 visualized the final improved results with an AMR simulations. Special emphasis is put on visualizing the physical recirculation pattern as a validation for the AMR.

A.3 the plots show the effect of time stepping for three different mesh sizes. This shows the effects of mesh resolution and time step size on the simulation results. By consequently reducing mesh spacing, and time stepping on ensures that the obtained results have converged in both time and space.

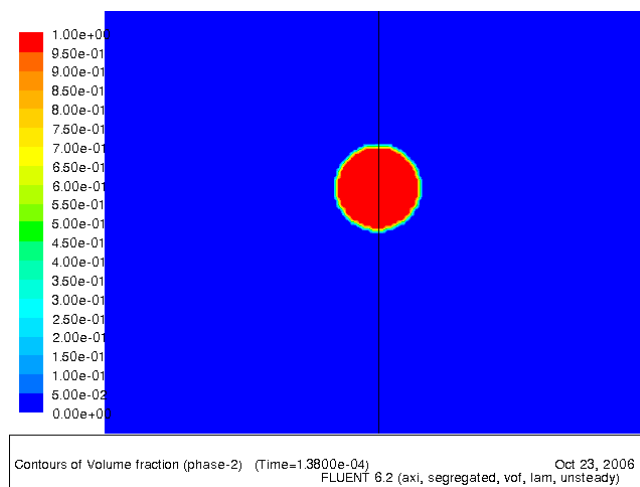
A.1 Phase contour of rising bubble



(a) Initially 25 cells, $d_b = 10\Delta x_{min}$.

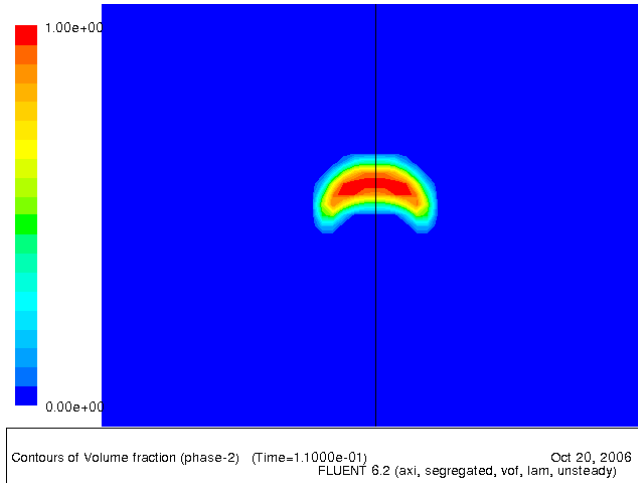


(b) Initially 99 cells, $d_b = 18\Delta x_{min}$.

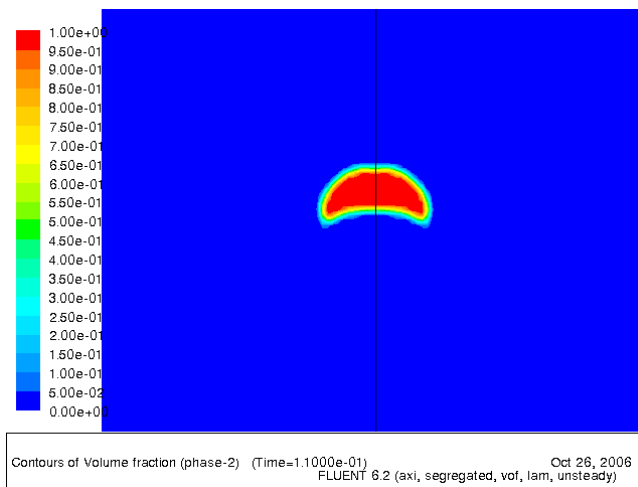


(c) Initially 402 cells, $d_b = 32\Delta x_{min}$.

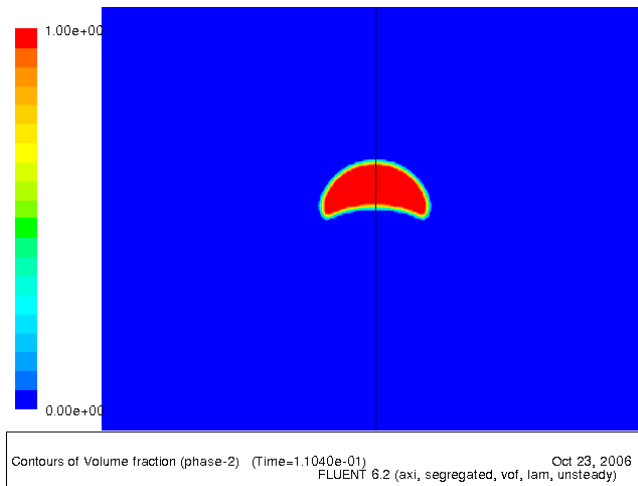
Figure A.1: Non dimensional time, $\tau = 0.01$.



(a) Initially 25 cells, $d_b = 10\Delta x_{min}$.

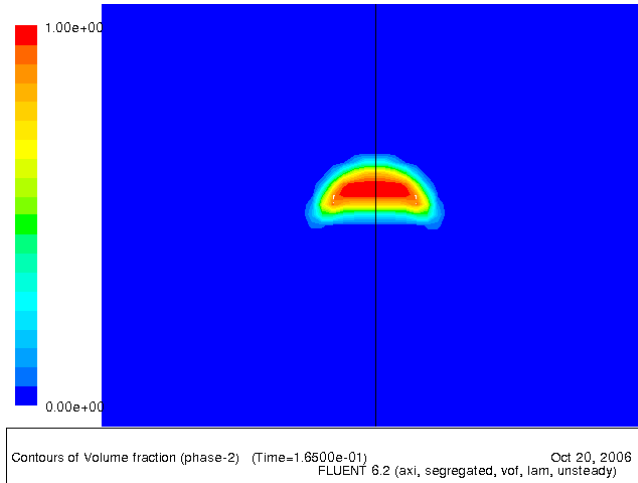


(b) Initially 99 cells, $d_b = 18\Delta x_{min}$.

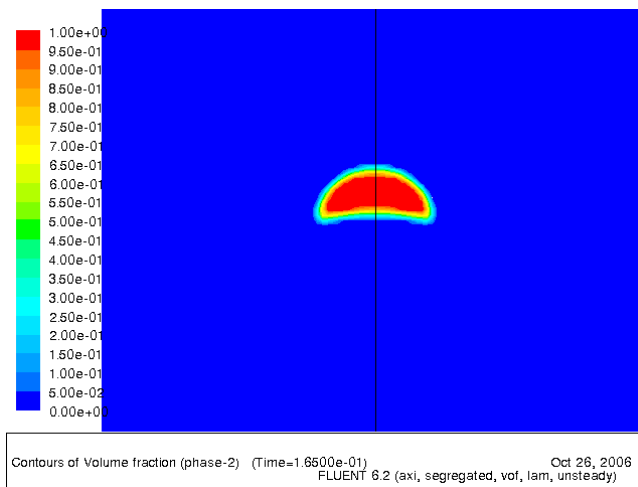


(c) Initially 402 cells, $d_b = 32\Delta x_{min}$.

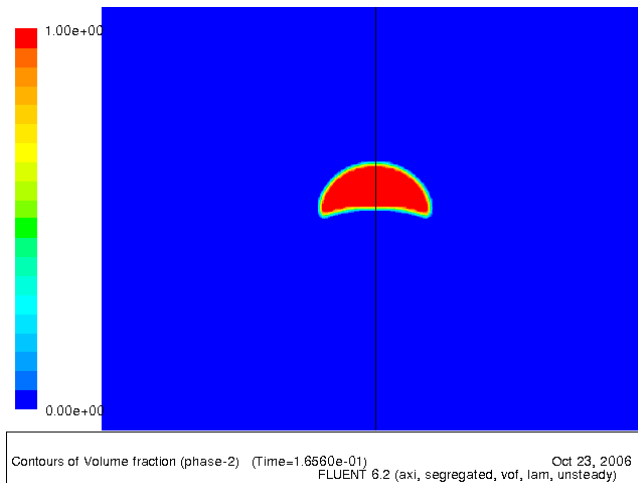
Figure A.2: Non dimensional time, $\tau = 2.23$.



(a) Initially 25 cells, $d_b = 10\Delta x_{min}$.



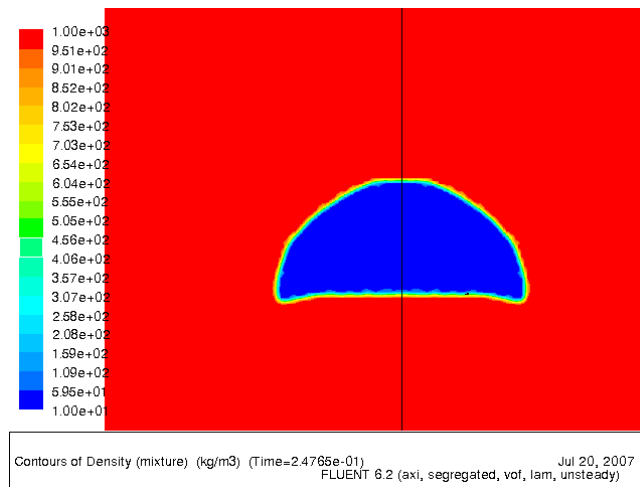
(b) Initially 99 cells, $d_b = 18\Delta x_{min}$.



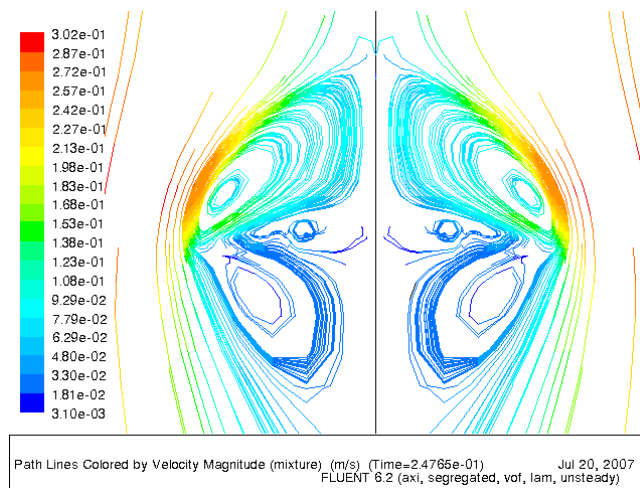
(c) Initially 402 cells, $d_b = 32\Delta x_{min}$.

Figure A.3: Non dimensional time, $\tau = 3.69$.

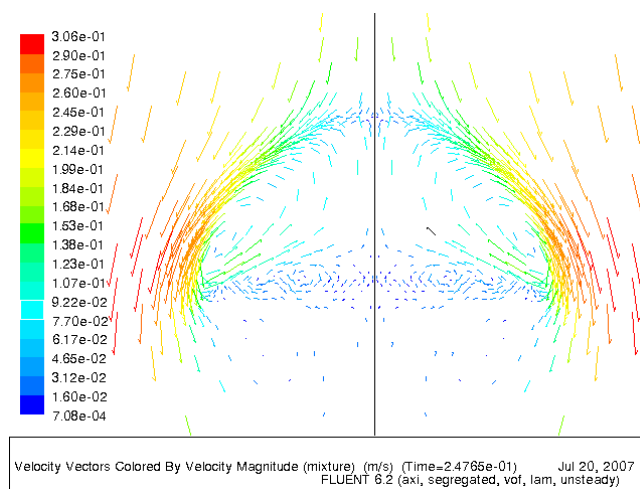
A.2 AMR of rising bubble



(a) Contour of the phases rising bubble.



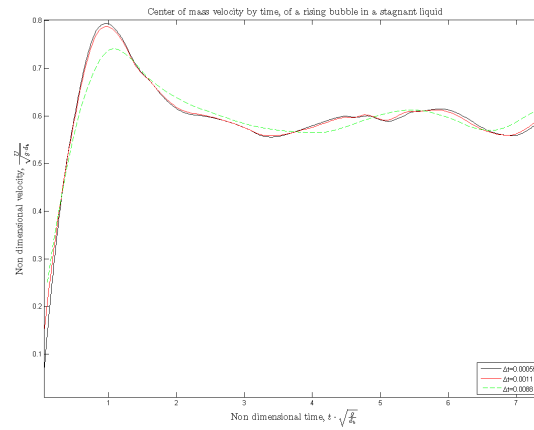
(b) Pathlines for rising bubble.



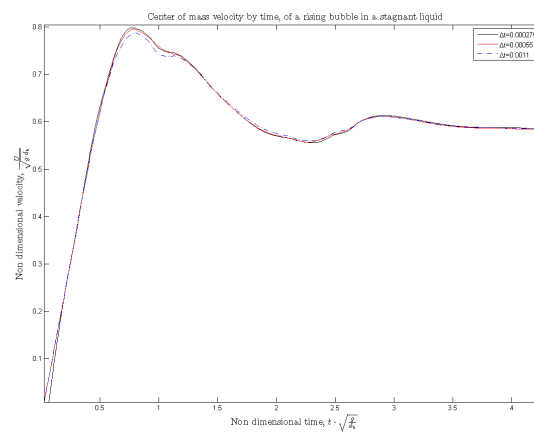
(c) Velocity vectors for rising bubble.

Figure A.4: AMR results for rising bubble in stagnant liquid, $\tau = 5.53$.

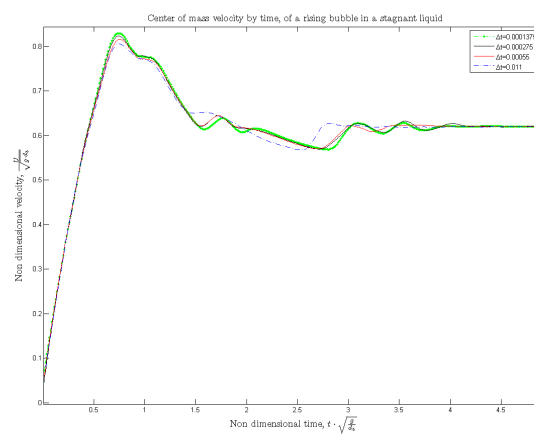
A.3 Reduced time evolution of speed of bubble displacement



(a) $\Delta x_{min} = 2 \cdot 10^{-3}m$, for three different time-steps.



(b) $\Delta x_{min} = 1.11 \cdot 10^{-3}m$, for three time-steps.



(c) $\Delta x_{min} = 6.6 \cdot 10^{-4}m$, for four time-steps.

Figure A.5: Space end time convergence, three different meshes with reduced time steps.

Appendix B

Parametric study of slug flow in TransAT

B.1 Parameter domain

To gain physical insight about slug flow the effects of change in parametric properties have been investigated in a short pipe (10D). Special interest has been focused on the flow patten within the bubbles as well as bubble topology. A hypothesis for the driving forces in the bubble break-up is suggested. There seem to be three different regimes that govern the break-up and slug flow generation. First is *Shear* driven, with strong recirculation patterns in the bubble. Several vortexes can be captured as an effect of the coupling of the shear over the interface. For the shear created break-up strong vortexes and low inertia forces are typical. Second is *Shear-Inertia* driven break-up, with the effects from both bubble inertia forces and recirculation in the bubble. Together these govern the bubble breakup. Third is the pure *Inertia* driven bubble break-up, high bubble inertia force that is creating the bubble break-up.

Case	U_L [$\frac{m}{s}$]	U_G [$\frac{m}{s}$]	ρ_G [$\frac{kg}{m^3}$]	ρ_L [$\frac{kg}{m^3}$]	μ_G [$\frac{kg}{ms}$]	μ_l [$\frac{kg}{ms}$]	D [m]	σ [$\frac{N}{m}$]	α [-]
6	1.11	0.66	12.2	998	$1.78 \cdot 10^{-5}$	0.0010	10^{-3}	0.0727	0.36
7	1.11	0.66	1.22	998	0.0010	0.0010	10^{-3}	0.0727	0.36
8	1.11	0.66	1.22	998	$1.78 \cdot 10^{-5}$	0.0010	10^{-3}	0.3635	0.36
9	1.11	0.66	1.22	998	$1.78 \cdot 10^{-5}$	0.0010	10^{-4}	0.0727	0.36
10	1.11	0.66	122	998	$1.78 \cdot 10^{-5}$	0.0010	10^{-3}	0.0727	0.36
11	1.11	0.66	1.22	998	$1.78 \cdot 10^{-5}$	0.0010	10^{-3}	0.727	0.36

Table B.1: Material properties, Case 6 – 11.

Case	$S = \frac{U_L}{U_G}$	U_B [$\frac{m}{s}$]	Ca_G	Ca_L	Ca_B
6	1.68	1.354	0.00016	0.01531	0.01869
7	1.68	1.12	0.00910	0.01531	0.01549
8	1.68	0.924	$3.22 \cdot 10^{-5}$	0.00306	0.00255
9	1.68	1.81	0.00016	0.01531	0.02493
10	1.68	1.11	0.00016	0.0153	0.01537
11	1.68	—	$1.6 \cdot 10^{-5}$	0.00153	—

Table B.2: Bubble velocity, slip ratio and Capillary number, Case 6 – 11.

Case	We_G	We_L	We_B
6	0.07310	16.91	25.18
7	0.007310	16.91	17.31
8	0.00146	3.38	2.34
9	0.00073	1.69	4.48
10	0.73099	16.91	17.04
11	0.00073	1.691	—

Table B.3: Weber number, Case 6 – 11.

Case	Oh_G	Oh_L	Oh_B
6	0.00060	0.00372	0.00372
7	0.10650	0.00372	0.00372
8	0.00084	0.00166	0.00166
9	0.00597	0.0117	0.01177
10	0.00019	0.00372	0.00372
11	0.00060	0.00118	—

Table B.4: Ohnesoge number, Case 6 – 11.

B.2 Numerical results and discussion

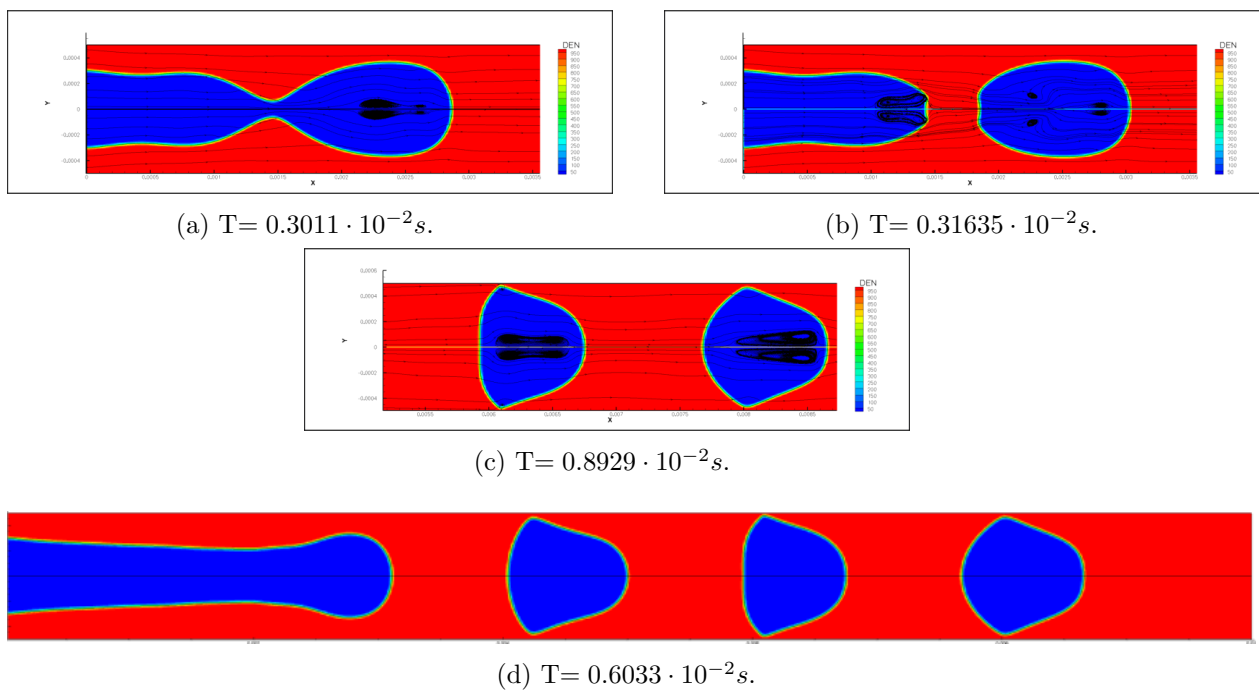


Figure B.1: Contours of the densities with streamlines and isoline for $\phi = 0$, Case 6.

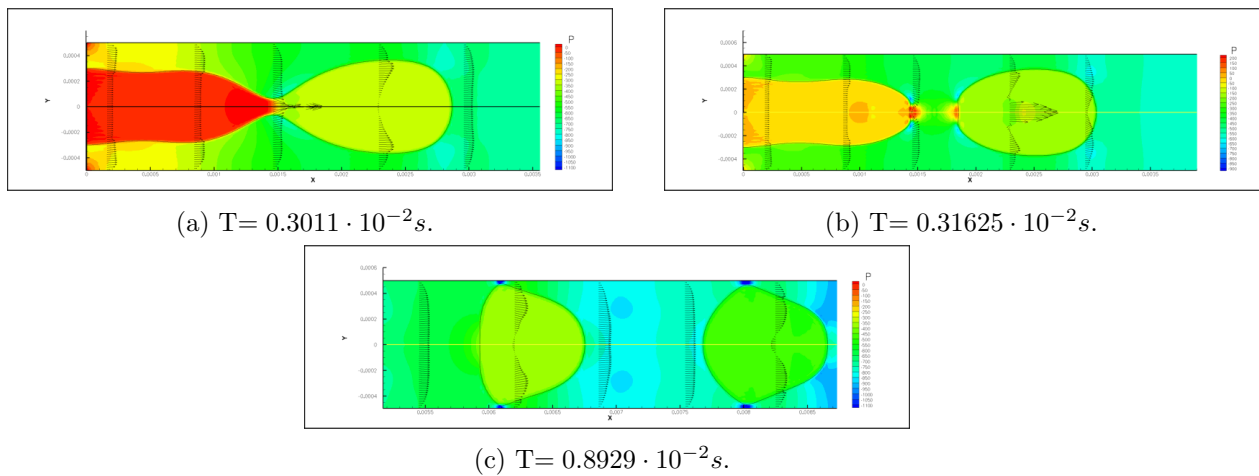
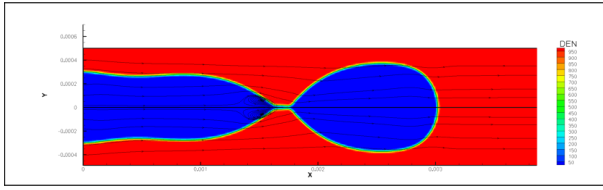
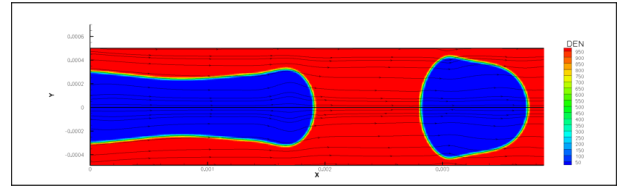


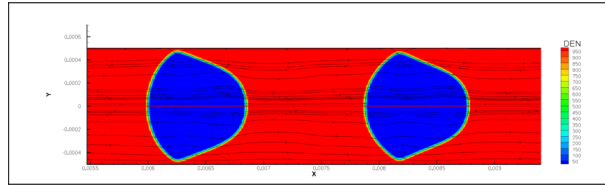
Figure B.2: Contours of the pressure with velocity vectors and isoline for $\phi = 0$, Case 6.



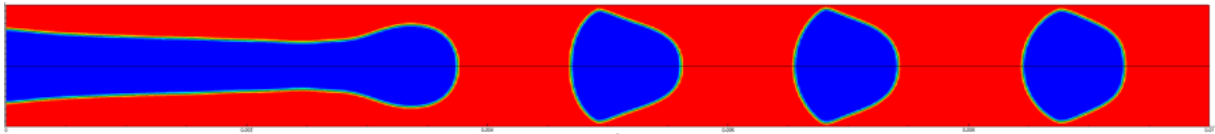
(a) $T = 0.3177 \cdot 10^{-2} s.$



(b) $T = 0.38189 \cdot 10^{-2} s.$

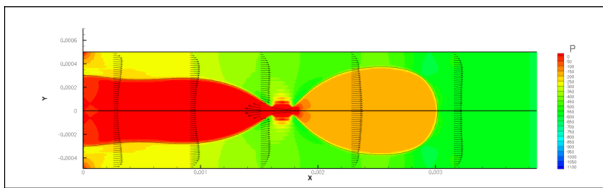


(c) $T = 0.8380 \cdot 10^{-2} s.$

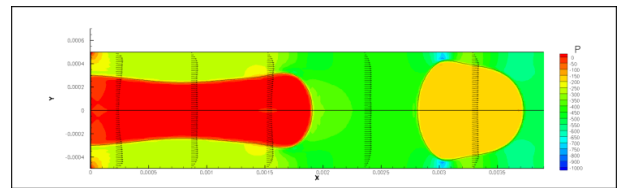


(d) $T = 0.6033 \cdot 10^{-2} s.$

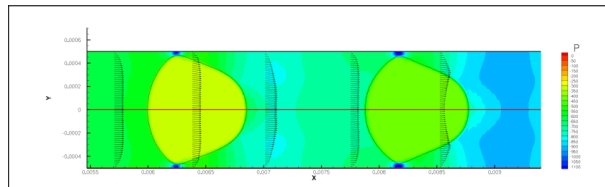
Figure B.3: Contours of the densities with streamlines and isolate for $\phi = 0$, Case 7.



(a) $T = 0.3177 \cdot 10^{-2} s.$

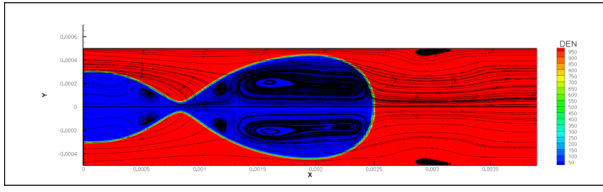


(b) $T = 0.3819 \cdot 10^{-2} s.$

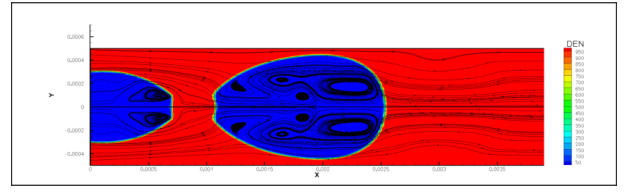


(c) $T = 0.8380 \cdot 10^{-2} s.$

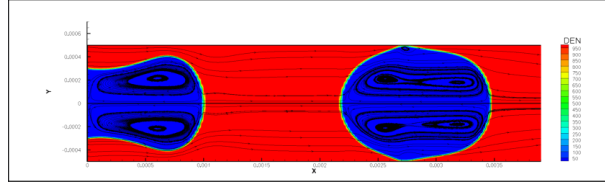
Figure B.4: Contours of the pressure with velocity vectors and isolate for $\phi = 0$, Case 7.



(a) $T = 0.32057 \cdot 10^{-2} s.$



(b) $T = 0.32057 \cdot 10^{-2} s.$

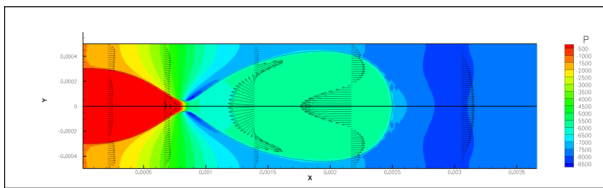


(c) $T = 0.4207 \cdot 10^{-2} s.$

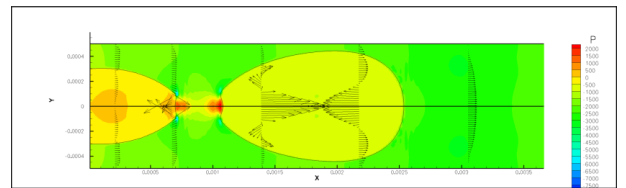


(d) $T = 0.4684 \cdot 10^{-2} s.$

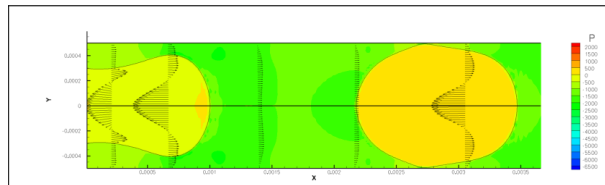
Figure B.5: Contours of the densities with streamlines and isline for $\phi = 0$, Case 8.



(a) $T = 0.32057 \cdot 10^{-2} s.$

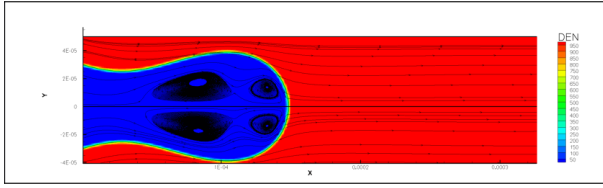


(b) $T = 0.32057 \cdot 10^{-2} s.$

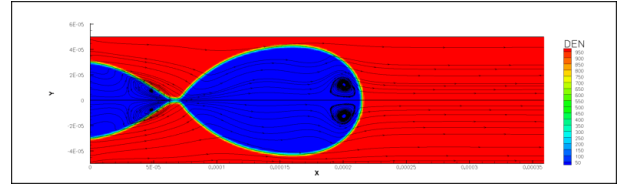


(c) $T = 0.4207 \cdot 10^{-2} s.$

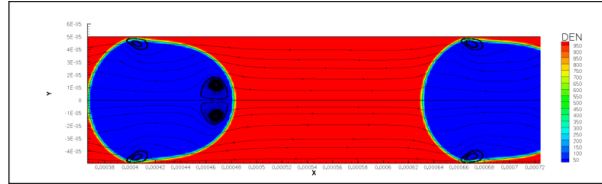
Figure B.6: Contours of the pressure with velocity vectors and isline for $\phi = 0$, Case 8.



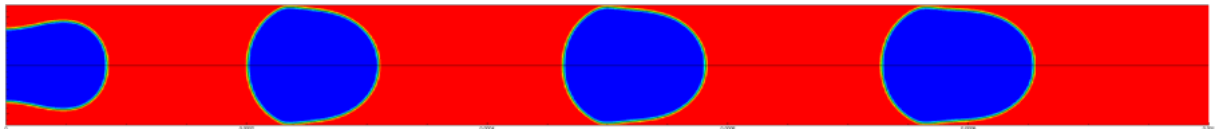
(a) $T = 0.198 \cdot 10^{-3} s.$



(b) $T = 0.2671 \cdot 10^{-3} s.$

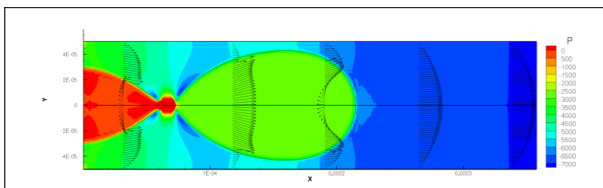


(c) $T = 0.7671 \cdot 10^{-3} s.$

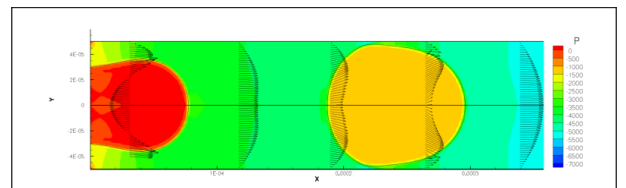


(d) $T = 0.8587 \cdot 10^{-2} s.$

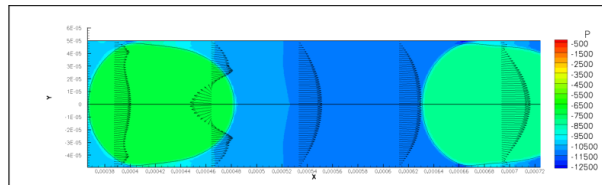
Figure B.7: Contours of the densities with streamlines and isoline for $\phi = 0$, Case 9.



(a) $T = 0.2671 \cdot 10^{-2} s.$

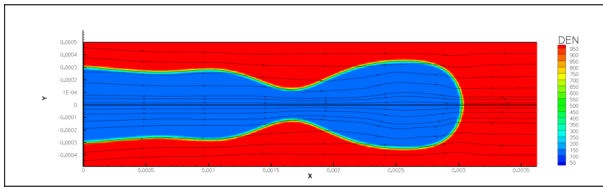


(b) $T = 0.3445 \cdot 10^{-3} s.$

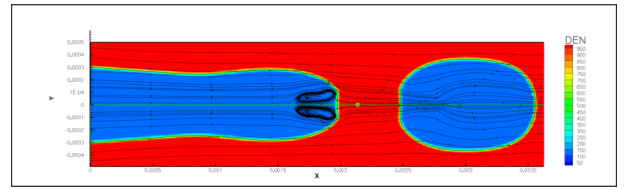


(c) $T = 0.7670 \cdot 10^{-3} s.$

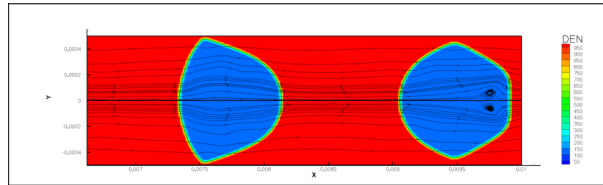
Figure B.8: Contours of the pressure with velocity vectors and isoline for $\phi = 0$, Case 9.



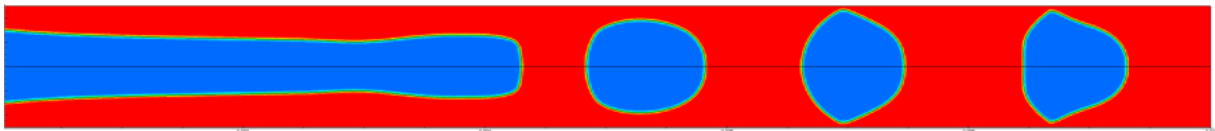
(a) $T = 0.32045 \cdot 10^{-2} s.$



(b) $T = 0.3685 \cdot 10^{-2} s.$

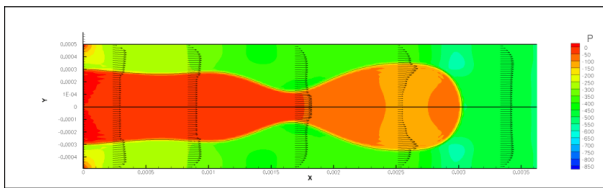


(c) $T = 0.944 \cdot 10^{-2} s.$

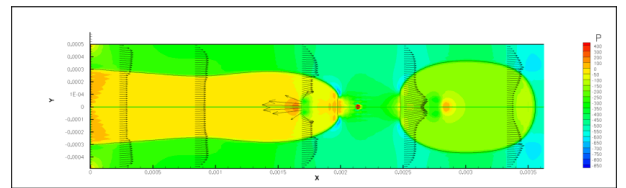


(d) $T = 0.8848 \cdot 10^{-2} s.$

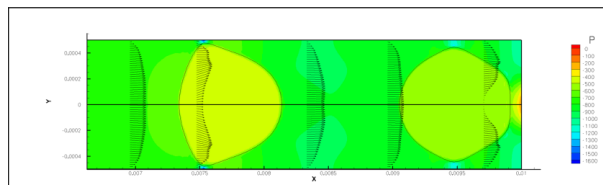
Figure B.9: Contours of the densities with streamlines and isolate for $\phi = 0$, Case 10.



(a) $T = 0.32045 \cdot 10^{-2} s.$

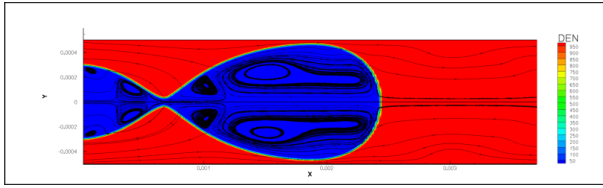


(b) $T = 0.3685 \cdot 10^{-2} s.$

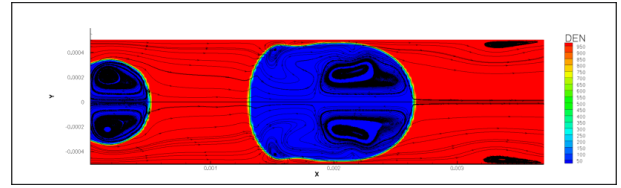


(c) $T = 0.9440 \cdot 10^{-2} s.$

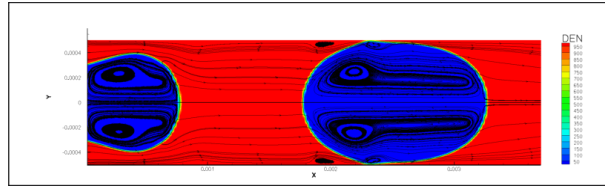
Figure B.10: Contours of the pressure with velocity vectors and isolate for $\phi = 0$, Case 10.



(a) $T = 0.315 \cdot 10^{-3} s.$



(b) $T = 0.3368 \cdot 10^{-3} s.$

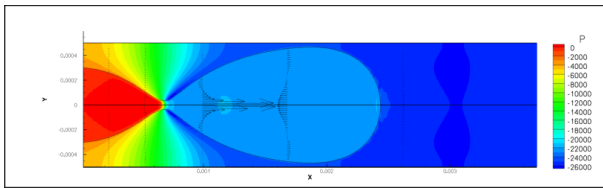


(c) $T = 0.39263 \cdot 10^{-2} s.$

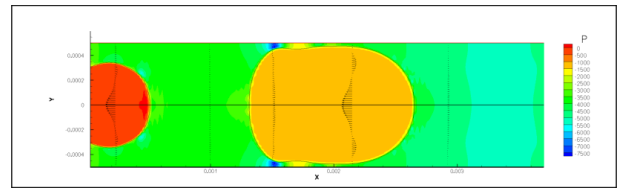


(d) $T = 0.8848 \cdot 10^{-2} s.$

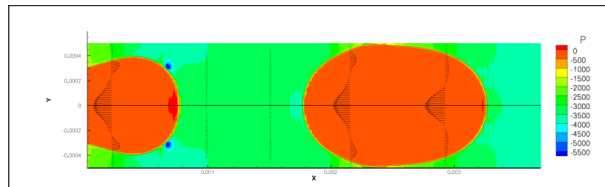
Figure B.11: Contours of the densities with streamlines and isolate for $\phi = 0$, Case 11.



(a) $T = 0.315 \cdot 10^{-3} s.$



(b) $T = 0.3368 \cdot 10^{-3} s.$



(c) $T = 0.39263 \cdot 10^{-2} s.$

Figure B.12: Contours of the densities with streamlines and isolate for $\phi = 0$, Case 11.

The pressure drop for the small pipe has been mapped.

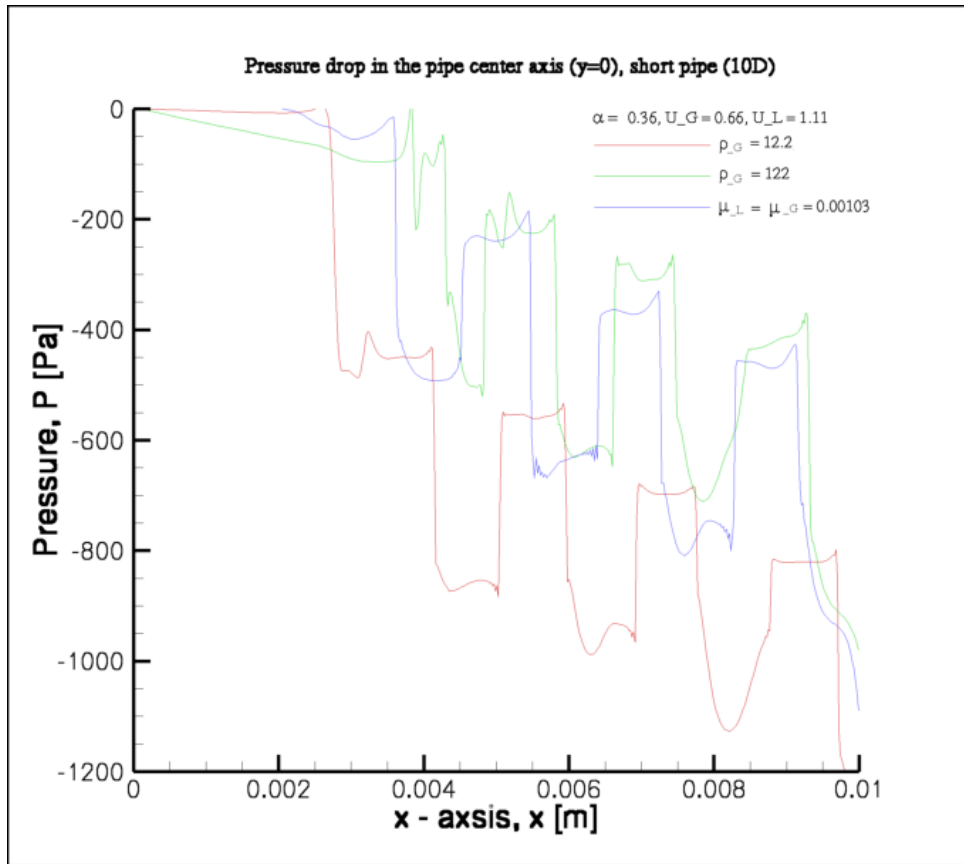


Figure B.13: Pressure drop in short pipe ($10D$) for Case 6, 7, 10.

Appendix C

Long wave theory

C.1 Critical note on publication: Long-scale evolution of thin liquid films [30]

As the results from long wave theory were scrutinized, it was apparent that with the data from [30] it was a problem to obtain the correct rupture time. It was noticed that there is an inconsistency with the original paper from Bruehlbach et. al. [9] and the paper from Oron et. al. [30]. The results from the non dimensional isothermal case that was reprinted in [30] (page 941 eq.2.41b) eq.(C.2) do not correspond with the original paper [9]. The last term is multiplied by a factor of $\frac{1}{3}$ compared to the original equation in [9] eq.(C.1). This influences the results as well and the rupture time.

$$\text{Bruehlbach et. al. [9]} \quad \partial_T H + A \partial_X \left(\frac{\partial_X H}{H} \right) + C \partial_X (H^3 \partial_X^3 H) = 0 \quad (\text{C.1})$$

$$\text{Oron et. al. [30]} \quad \partial_T H + A \partial_X \left(\frac{\partial_X H}{H} \right) + \frac{C}{3} \partial_X (H^3 \partial_X^3 H) = 0 \quad (\text{C.2})$$

C.2 Effective length of Van der Waals forces

The plot below shows the effective length of the Van der Waals forces with the parameters from Bruelbach et. al. [9]. It is also observed that the effective length of the Van der Waals forces scale by the order of two magnitudes of the Hamaker constant. This means that if the effective length is supposed to be changed from $10nm$ to $100nm$, $n = \frac{h_2}{h_1} = \frac{100nm}{10nm}$ the Hamaker constant must be changed from $x \cdot 10^i$ to $\sim n^2 \cdot x \cdot 10^i$ (x is an arbitrary constant).

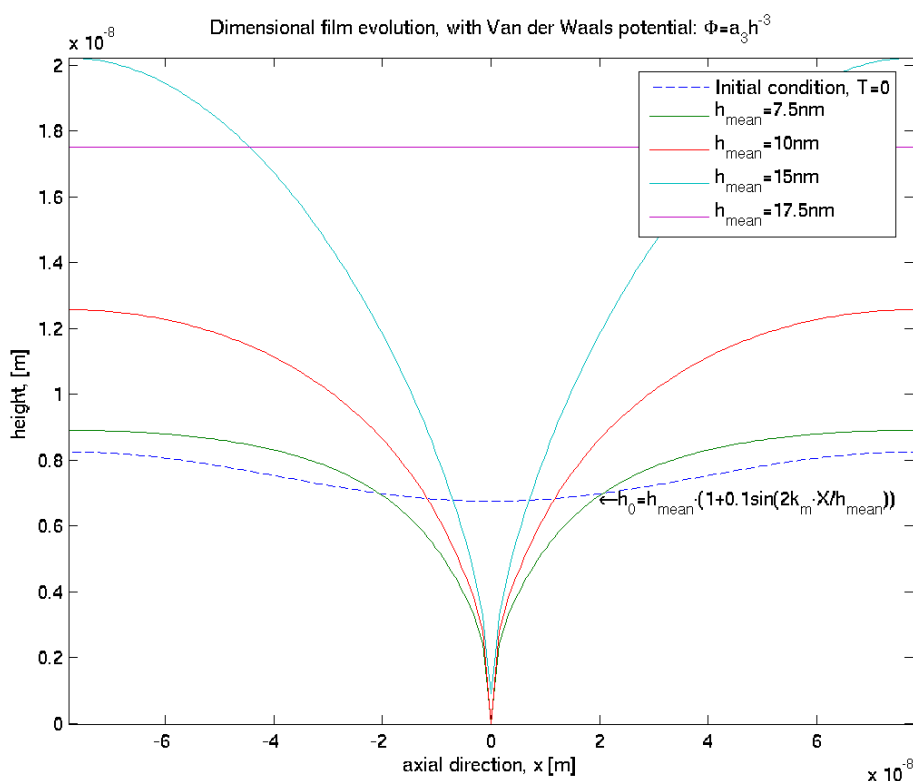


Figure C.1: Effective length of the Van der Waals forces shown by changing initial mean film height, parameters from [9].

